FDOT Research Project Number BDV29-977-05

NON-DESTRUCTIVE TESTING (NDT) OF A SEGMENTAL CONCRETE BRIDGE SCHEDULED FOR DEMOLITION, WITH A FOCUS ON CONDITION ASSESSMENT AND CORROSION DETECTION OF INTERNAL TENDONS

FINAL REPOR

Atorod Azizinamini, Ph.D., P.E.

Principal Investigator

Department of Civil and Environmental Engineering

Florida International University

Miami, Florida

Sponsored By

Florida Department of Transportation

May, 2017

DISCLAIMER

The opinions, findings, and conclusions expressed in this publication are those of the author(s) and not necessarily those of the Florida Department of Transportation or the U.S. Department of Transportation.

For clarity and completion of some discussion on available NDTs, portions of earlier published works have been included in the Introduction section.

REPORT PREPARED BY

Sheharyar e Rehmat
Amir Sadeghnejad
Saiada Fuadi Fancy
Alireza Valikhani
Brian Chunn
Alireza Mohammadi
Ramin Taghinezhadbilondy
Mohammadtaghi Moravej
Jawad Gull
Aaron Yakel

and

Kingsley Lau
Atorod Azizinamini

CONVERSION TABLES

Approximate conversion to SI Units

Symbol	When you know	Multiply by	To find	Symbol
Length				
in	inches	25.4	millimeters	mm
ft	feet	0.305	meters	m
yd	yards	0.914	meters	m
mi	miles	1.61	kilometers	km
Area				
in^2	square inches	645.2	square millimeters	mm^2
ft^2	square feet	0.093	square meters	m^2
yd^2	square yard	0.836	square meters	m^2
ac	acres	0.405	hectares	ha
mi^2	square miles	2.59	square kilometers	km^2
Volume				
fl oz	fluid ounces	29.57	milliliters	mL
gal	gallons	3.785	liters	L
ft^3	cubic feet	0.028	cubic meters	m^3
yd^3	cubic yards	0.765	cubic meters	m^3
Mass				
oz	ounces	28.35	grams	g
lb	pounds	0.454	kilograms	kg
T	short tons (2000 lb)	0.907	megagrams (or "metric ton")	Mg (or "t")
Temperature				
°F	Fahrenheit	5 (F-32)/9 or (F-32)/1.8	Celsius	°C
Illumination				
fc	foot-candles	10.76	lux	lx
fl	foot-Lamberts	3.426	candela/m^2	cd/m^2
Force and Pressure or Stress				
lbf	pound force	4.45	newtons	N
lbf/in^2	pound force per square inch	6.89	kilopascals	kPa

Approximate conversion to U.S. Customary Units

Symbol	When you know	Multiply by	To find	Symbol
Length				
mm	millimeters	0.039	inches	in
m	meters	3.28	feet	ft
m	meters	1.09	yards	yd
km	kilometers	0.621	miles	mi
Area				
mm^2	square millimeters	0.0016	square inches	in^2
m^2	square meters	10.764	square feet	ft^2
m^2	square meters	1.195	square yards	yd^2
ha	hectares	2.47	acres	ac
km^2	square kilometers	0.386	square miles	mi^2
Volume				
mL	milliliters	0.034	fluid ounces	fl oz
L	liters	0.264	gallons	gal
m^3	cubic meters	35.314	cubic feet	ft^3
m^3	cubic meters	1.307	cubic yards	yd^3
Mass				
g	grams	0.035	ounces	oz
kg	kilograms	2.202	pounds	lb
Mg (or "t")	megagrams (or "metric ton")	1.103	short tons (2000 lb)	T
Temperature				
°C	Celsius	1.8C+32	Fahrenheit	°F
Illumination				
lx	lux	0.0929	foot-candles	fc
cd/m^2	candela/m^2	0.2919	foot-Lamberts	fl
Force and Pressure or Stress				
N	newtons	0.225	pound force	lbf
kPa	kilopascals	0.145	pound force per square inch	lbf/in^2

TECHNICAL REPORT DOCUMENTATION

1. Report No.	2. Government Accession No.	3. Recipient's Catalog No.

4. Title and Subtitle
Non-Destructive Testing (NDT) of a Segmental Concrete Bridge Scheduled for Demolition, with a Focus on Condition Assessment and Corrosion Detection of Internal Tendons

5. Report Date

6. Performing Organization Code

7. Author(s)
Sheharyar e Rehmat, Amir Sadeghnejad, Saiada Faudi Fancy, Brian Chunn, Alireza Valikhani, Alireza Mohammadi, Ramin Taghinezhadbilondy, Mohammadtaghi Moravej, Jawad Gull, Aaron Yakel, Kingsley Lau, Atorod Azizinamini

8. Performing Organization Report No.

9. Performing Organization Name and Address
Florida International University, Miami
http://breslint@servax.fiu.edu
University Park, Room P.C. 539
Miami, FL 33199-0000

10. Work Unit No. (TRAIS)

11. Contract or Grant No.
BDV29-977-05

12. Sponsoring Agency Name and Address
Florida Department of Transportation
605 Suwannee Street
Tallahassee, FL 32399-0450
U.S.

13. Type of Report and Period Covered
Final report
Apr 2013-May 2017

14. Sponsoring Agency Code

15. Supplementary Notes

16. Abstract
The service life and durability of prestressed concrete in bridges are vulnerable to corrosion damages due to many factors such as construction, material, and environment. To ensure public safety, it is important to inspect these structures and to develop appropriate mitigation measures for corrosion damages. The availability of Non Destructive Testing (NDT) technology has made it possible to evaluate the condition of a bridge without invasive removal of concrete. A project bridge located in Fort Lauderdale, scheduled for demolition, provided an opportunity to carry out various on-site and post-deconstruction tests. An analytical study was carried out for demolition sequence, and segments of the bridge were transported to Florida International University (FIU). These segments were used as a test bed setup, and additional laboratory tests were conducted to evaluate some of the NDT technologies which can be extended to the testing of actual structures. The on-site field tests using impulse response showed a reduction in global stiffness, due to partial deconstruction while acoustic emission demonstrated possible use in detection of vibration due to tendon breakages. During the field tests, infrared thermography assisted in identification of ducts with deficient grout and the use of infrared thermography was further investigated in laboratory tests. The method has shown the possibility to detect wire breakages in encapsulated grout. A methodology to detect tendon damages in internal tendons in the presence of secondary reinforcement was investigated using the magnetic flux leakage method for laboratory test setup and validated on decommissioned test segments. The inductance method showed promising results for laboratory and segment tests, but obscuring of signals due to mild reinforcement is a challenge.

17. Key Words
Non-destructive testing, Magnetic flux leakage, Infrared thermography, Impulse response, Acoustic emission, Inductance

18. Distribution Statement

19. Security Classif. (of this report)	20. Security Classif. (of this page)	21. No. of Pages	22. Price
Unclassified	Unclassified	143	

ACKNOWLEDGEMENTS

The authors would like to thank the Florida Department of Transportation (FDOT) and project manager John Danielsen.

EXECUTIVE SUMMARY

Prestressed concrete bridge (PSC) structures have been designed and constructed for over 40 years in the U.S. with generally good structural and durability performance. Even though the prestressing steel is ideally protected from corrosion when either placed inside a grouted plastic or steel duct for post-tensioned (PT) applications or directly bonded with the concrete in pre-tensioning applications, corrosion remains a challenge. The limited capabilities of available non-destructive testing (NDT) techniques present challenges for practical field condition assessment of steel strand. Furthermore, few of these techniques can assess internal PT tendons.

The project bridge (bridge number 860434) located in Fort Lauderdale exit ramp to SB US-1 was scheduled for demolition and to be used as a test bed by the Florida International University (FIU) research team. The decommissioning of the bridge provided a unique opportunity for testing on full-sized structures in various service conditions, including (1) the in-service bridge conditions, (2) bridge segments during the deconstruction process, and (3) placement of extracted bridge segments in outdoor laboratory conditions. The main objective of the project was to carry out limited NDT in the field on the segmental concrete bridge prior to its demolition, to evaluate the merits of NDT techniques. The NDT techniques should provide condition assessment of segmental concrete bridges and detect corrosion. The work evaluated the merits of different approaches that could be used during routine bridge inspections to detect major changes in the structural characteristics of segmental concrete bridges.

Sequential demolition of the bridge was carried out by Finley Engineering Group, Inc. (Tallahassee, FL), based on safety aspects. An analytical study, which replicated the construction stages of a segmental bridge, projected the developed stresses for intermediate and final structure conditions. The analytical model of the structure provided checks for various deconstruction stages such as stability of superstructure for the mid-span cut and removal of segments. The analytical study provided a theoretical response of the structure which was in general not inconsistent with the results of conducted on-site NDTs. A visual survey was carried out on the portion of the bridge that was demolished. This post-deconstruction survey revealed some partially grouted ducts, honeycombing, and strands showing signs of corrosion. However, most of the components of post-tensioning systems showed no major deficiencies and were in good condition.

Several on-site field tests were conducted on the bridge to observe the overall response of the structure and to investigate the condition of bridge components. The impulse response (IR) provided a mobility spectrum that is indicative of flexibility of the structural element. Within a span, the mobility of the bridge decreased at the junction of deck and web and showed higher values in the middle of the span due to lower stiffness. A higher mobility of the bridge, along the width and length of bridge, was observed after partial demolition of the bridge, which is indicative of the reduction in global stiffness of the structure. These observations would indicate that although the results of the IR test could not necessarily be used to identify damage, conducting IR tests at different times during the service life of a bridge can be used to evaluate major changes in stiffness of the bridge superstructure. Major degradation of the concrete or reinforcing steel may result in stiffness loss.

Infrared thermography (IRT) with active heating could not be conducted in the field due to safety concerns during bridge deconstruction. The field work instead aimed to identify practicality of heating and differential cooling by passive heating. In Florida summer conditions, passive heating from the sun did allow differential heating especially when surfaces are partially sheltered. Also, IRT by passive heating could detect bulk concrete elements such as the tendon blisters. The bridge concrete surface conditions did not contain significant anomalous features that could be detected by IRT. After demolition, access to the strands in the bridge segments for IRT by active heating using a torch did not give good resolution of embedded steel conditions due to the good thermal properties of the bulk concrete itself. IRT on available segments from failed tendons from another bridge could differentiate deficient grout from hardened grout. The on-site field tests on tendons using IRT tests required further investigation into deficient grout. Therefore, a set of laboratory IRT test was conducted and preliminary results showed that inductive heating can detect wire damages and differential grout materials. The findings support the use of inductive heating where the steel components are heated differentially from the surrounding grout. Further investigation is required to develop an adaptable inductive heater, determining heat required to provide good resolution especially in the presence of metal and plastic tendon ducts and minimization of thermal reflections.

Acoustic emission (AE) tests carried out under no-traffic conditions were effective in pinpointing the location of calibration hammer strikes. The results showed that broken tendons produced substantial vibration amplitude above typical traffic noise and thus can be measured at a distance of 20 ft or more. However, during saw cutting operations, analysis showed poor to fair results due to the high level of noise generated by the saw cutting operation and three-dimensional nature of real structures. The optimization of sensor layout and use of improved signal processing techniques could be advantageous. The IBIS-S interferometric radar system was used to detect overall structure movements during saw-cutting operations, but due to high stiffness of the structure, significant movement could not be detected.

The magnetic flux leakage (MFL) method was used to assess damage in PT strands. The laboratory tests showed the capability of the system to detect physical discontinuity in strands using the active magnetic field. Secondary ferromagnetic sources such as mild steel reinforcement can lead to complicated signals and can make detection of strand defects challenging. A methodology was proposed to reduce the effect of transverse steel reinforcing rebar. Results showed that test artifacts from the transverse reinforcing bars can be reduced and allow for clearer identification of strand defects. A numerical study was carried out to validate the MFL results, to show a finite element (FE) analysis can be used to improve the MFL system by assisting in sensor positions and choosing appropriate magnetic field for strand saturation.

The inductance method was tested under laboratory and field conditions. In controlled laboratory settings, the method was found to be effective in identifying metal loss in steel strand in ideal cases without presence of secondary reinforcing steel. For segment testing, the inductance method identified strand section loss, but interfering signals due to transverse mild reinforcement caused spikes in the inductance reading. Improvements to the method can be made, possibly including the quality of the inductance meter, coil geometry, number of turns of the coil, frequency of the test signal, concrete cover over the tendon, the thickness of the wall of the steel conduit, and magnetic interference (shielding) from transverse reinforcing steel.

TABLE OF CONTENTS

LIST OF FIGURES

LIST OF TABLES

LIST OF ABBREVIATIONS AND ACRONYMS

Acronym	**Definition**
AASHTO	American Association of State Highway and Transportation Officials
AC	Alternating Current
AE	Acoustic Emission
ASTM	American Society for Testing and Materials
AWG	American Wire Gauge
DAS	Data Acquisition System
DC	Direct Current
DOT	Department of Transportation
EMF	Electromotive force
FDOT	Florida Department of Transportation
FE	Finite Element
FEMM	Finite Element Method Magnetics
FHWA	Federal Highway Administration
FIU	Florida International University
GWT	Guided wave testing
HDPE	High density polyethylene pipe
HE	Hall Effect
IE	Impact Echo
IPR	Interferometric Phase Radar
IR	Impulse Response
IRT	Infrared thermography
MFL	Magnetic Flux Leakage
NDE	Non-Destructive Evaluation
NDT	Non-Destructive Testing
PI	Principal Investigator
P-P	Peak to Peak
PPM	Parts per million
PSC	Prestressed Concrete Structure
PT	Post-Tensioned
PTI	Post-Tensioning Institute
PVC	Polyvinyl Chloride
RH	Relative Humidity

1 INTRODUCTION

1.1 BRIEF OVERVIEW OF POST-TENSIONING SYSTEMS

Prestressed concrete bridge (PSC) structures have been designed and constructed for over 40 years in the U.S. with generally good structural and durability performance. Since its origin in the early 1900s, prestressing technology has been subject to advancements in prestressing techniques, construction practices, and building materials. Despite these advancements, the prestressing steel is subject to corrosion which has caused major damage to bridges in Europe and U.S. (Azizinamini & Gull, 2012b).

Even though the prestressing steel is ideally protected from corrosion when either placed inside a grouted plastic or steel duct for post-tensioned (PT) applications or directly bonded with the concrete in pre-tensioning applications, corrosion remains a challenge. In pre-tensioned concrete structures, exposure to salts such as marine environments can lead to chloride-induced corrosion. Corrosion loss of the steel can further exacerbate damage by causing concrete spalling and bond reduction between concrete and steel. In PT components, corrosion has been related to grout bleeding, grout voids, and grout segregation. Intrusion of moisture into the ducts can further aggravate corrosion conditions. The corrosion-induced structural damage of the concrete element and the strand metal loss can lead to brittle failure of the strand and significantly reduce the service life of the structure.

For PT systems, the tendons are either embedded inside concrete (internal post-tensioning) or externally applied to the structure (external post-tensioning). In these systems, tendon ducts provide cable profile for the prestressing steel and serves as a barrier to intrusive environmental contaminants. The tendons are either bonded or unbonded inside a duct which is made of plastic, galvanized steel, or high density polyethylene pipe (HDPE). The corrosion in bonded tendons is mitigated by grout injection through inlet and outlet valves which also contain plugs to prevent moisture and salt intrusion during and after construction. The cementitious grout intended to provide corrosion protection for PT systems has received significant attention in the past 20 years because of its association with severe corrosion in a number of bridges in Florida and elsewhere (Lau & Lasa, 2016). The specifications for the PT grouts have been revised for these reasons to provide multi-level protection for strands. Neat grouts were used in first decade of 20th century, but problems, such as excessive formation of bleed water and resulting grout void formation, were encountered. Despite the revisions of specifications in the late 1990s which introduced thixotropic grouts with low bleed water, the problem of corrosion mitigation still persists.

To ensure public safety and structural integrity, development of sound methodologies to assess the health of steel strands is crucial. The corrosion detection of these strands embedded in concrete is a challenging task and visual inspection may not be adequate or possible. Assessment of strand in internal PT tendons is particularly difficult as direct access to the tendon requires invasive removal of concrete. Many non-destructive evaluations (NDE) are available for PSC, most of which are advantageous for predicting material properties of concrete. However, the limited capabilities of available NDE present challenges for practical field condition assessment of steel strand. Furthermore, few of these techniques can assess internal PT tendons.

1.2 SUMMARY OF COMMERCIALLY AVAILABLE NDE TECHNOLOGY

1.2.1 General Background

In general, NDE technologies can be grouped per their underlying phenomenological basis, as illustrated in Figure 1-1. In the following sections, select meritorious, commercially available and commonly applied NDE technologies for condition assessment of PT and stay cable systems are reviewed. In the following sections, conventional applications of these technologies and their reported advantages and limitations in structural systems with cementitious materials (including prestressed bridge components) are highlighted. However, the current work sought to identify possible novel applications of these technologies to assist in bridge health assessment.

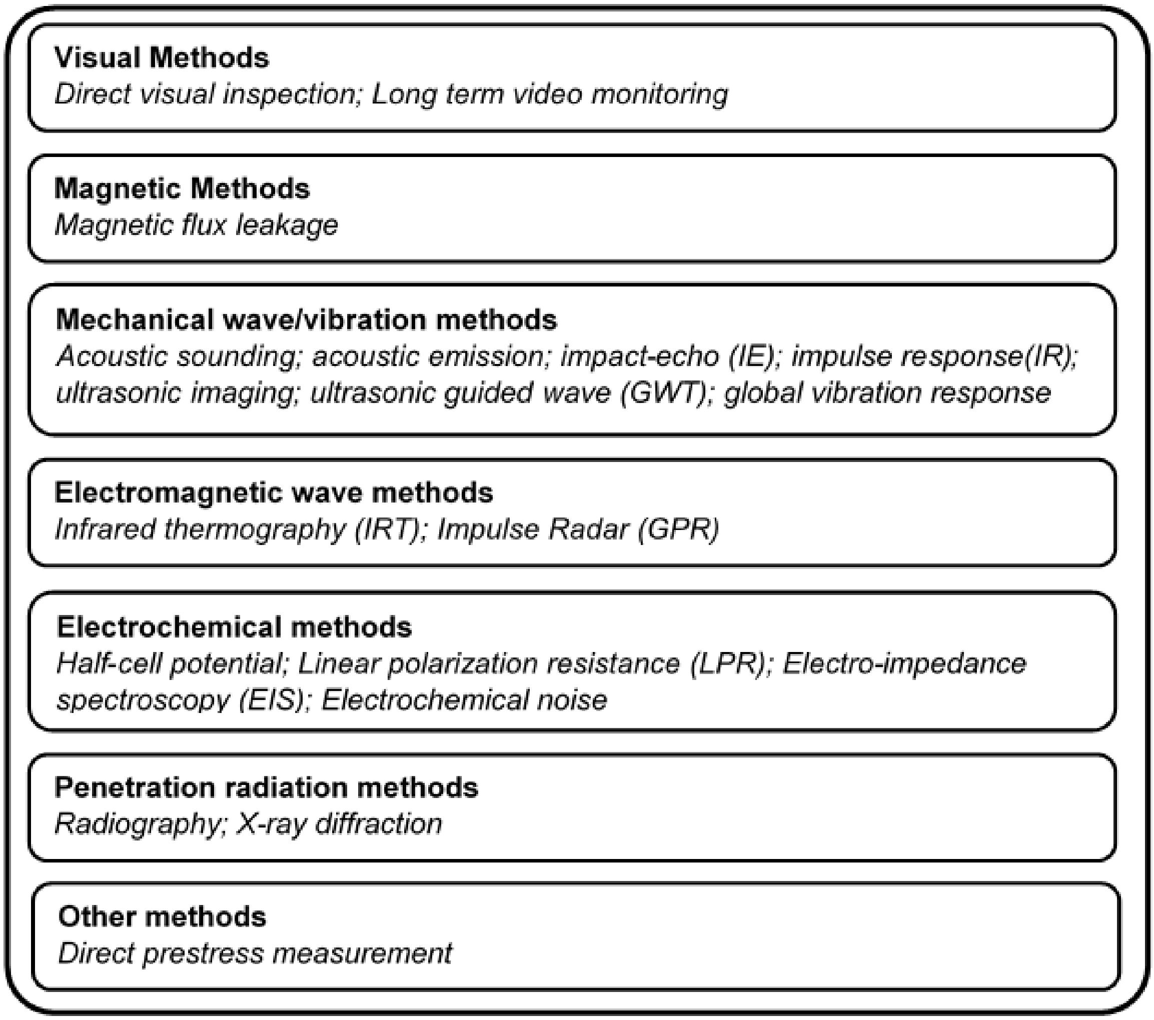

Visual Methods
Direct visual inspection; Long term video monitoring

Magnetic Methods
Magnetic flux leakage

Mechanical wave/vibration methods
Acoustic sounding; acoustic emission; impact-echo (IE); impulse response(IR); ultrasonic imaging; ultrasonic guided wave (GWT); global vibration response

Electromagnetic wave methods
Infrared thermography (IRT); Impulse Radar (GPR)

Electrochemical methods
Half-cell potential; Linear polarization resistance (LPR); Electro-impedance spectroscopy (EIS); Electrochemical noise

Penetration radiation methods
Radiography; X-ray diffraction

Other methods
Direct prestress measurement

Figure 1-1: Overview of NDE methods applied to inspect condition of PT systems (Azizinamini & Gull, 2012b)**.**

1.2.2 Impulse Response (IR)

The Impulse Response (IR) test provides a record or signature of the structural (mechanical) vibrational compliance of a structure near a given test location. The testing apparatus consists of a hammer with an attached load cell, capable of generating small force at a point in the deck. The other element of the testing device is a surface-mounted transducer capable of measuring response of the structure at relatively low frequency ranges; normally a geophone sensor (voltage output proportional to surface velocity) is used. The velocity transducer is placed at every defined testing grid point and an impact event from the instrumented hammer is applied nearby.

The loading function data from the hammer and the response signal from the surface sensor are collected and processed. The time signal information is then converted to the frequency domain by using the Fast Fourier Transform. The resulting velocity spectrum is then divided by the force spectrum to obtain a transfer function, referred to as the "mobility" of the element under the test. Mobility represents the maximum velocity at a given frequency at the test point per unit of applied impact force. A high mobility means that the unit force results in a relatively high velocity. Thus, mobility is related to the flexibility of the structural element at the test point. Mobility is an index that allows the engineer to quickly assess the local compliance condition, which can be used to illustrate relative changes across the structure.

The detailed procedure and standard for evaluating the condition of concrete decks is specified in ASTM C1740 (ASTM, 2010). The slab IR method requires access only to the top surface for receiver locations and hammer hitting. The receiver is mounted to the surface of the slab adjacent to the impact location and generally 3-4 inches away. In a slab IR investigation, the slab top is impacted with an impulse hammer and the response of the slab is monitored by a geophone placed next to the impact point. Figure 1-2 shows the testing configuration for the impulse-response method.

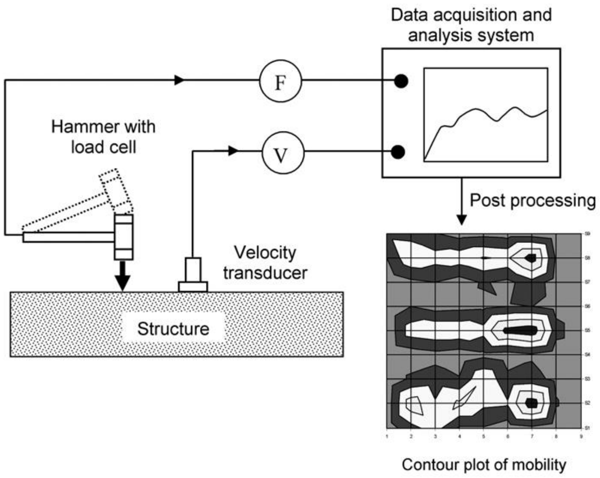

Figure 1-2: Schematic of the test setup and apparatus for IR test (ASTM, 2010)**.**

In plate-like structures the impact results predominantly in flexural vibration of the tested element, although other modes can be excited. Figure 1-3 shows waveforms from the load cell and the average mobility is the average of the mobility values from the mobility spectrum expressed in units of (m / s) / N or (in / s) / lb.

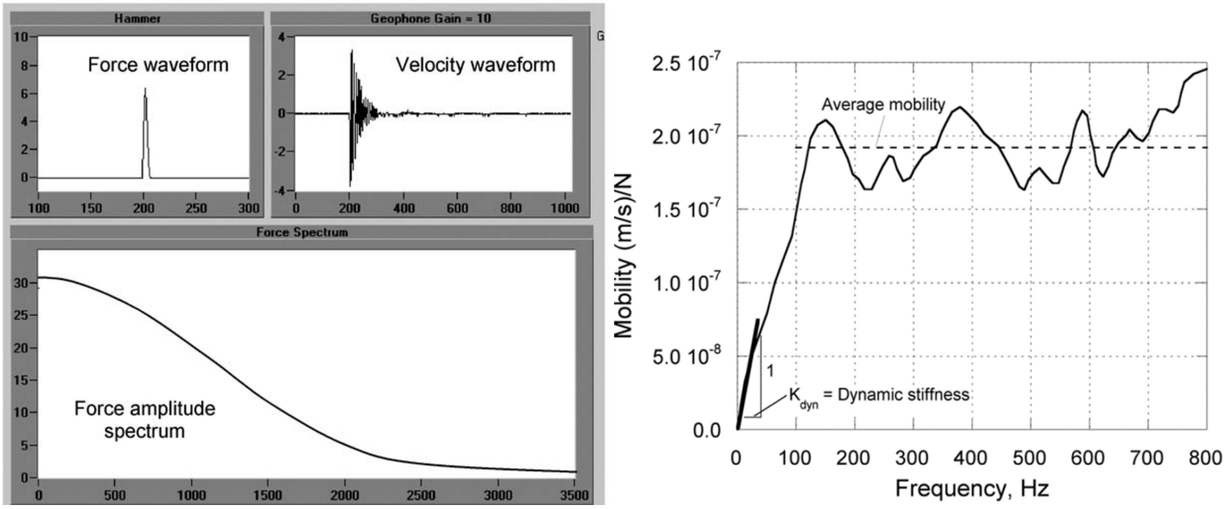

Figure 1-3: Typical force time waveform and amplitude spectrum plots from an IR test (ASTM, 2010)**.**

The force and velocity waveforms were recorded and subjected to digital signal processing to obtain the mobility spectrum at each test point. Key parameters were computed from the mobility spectra at the test points and displayed in the form of contour plots from which the likely locations of anomalous regions can be identified.

The IR response of a structural element is complex and depends on the geometry and boundary conditions of the element, the material properties, and the location and duration of the impact. Because of these complexities, it is not practical to use absolute values of measured impact responses to infer the internal conditions of a test element. The practical approach is to evaluate the response at different test points on a comparative basis. Those regions of the structure with unusually higher measures of mobility (velocity per unit of force) can be selected for further examination, either by other test methods or by invasive probing.

Table 1-1: Summary of inherent characteristics and application of IR

Advantages	Disadvantages	Best application case	Application with regard to duct type
- Potential to measure mechanical compliance of a duct system, which could reflect a duct grouting or other problem.	- Probably not sensitive to small defects.	- External ducts with large void in grout.	- Probably applicable only to external ducts, giving one global value for entire duct. - Unlikely to work for internal ducts unless void is very large.

The IR test is used primarily to identify and map subgrade voids below slabs-on-grade, loss of support beneath concrete pavements, debonding of bridge deck overlays, delamination caused by reinforcing steel corrosion, and the consolidation of mass concrete. The IR method has been used on slabs of a wide range of thicknesses, but is most effective on thinner slabs (less than 12 inches thick).

Recent advances in ultrasonic array transducer technology have promoted the development of ultrasonic imaging capability in concrete (Azizinamini & Gull, 2012b). The IR test is best suited for evaluating the global (overall changes in stiffness of the structure) and local (such as delamination of cover concrete, existence of void in cover concrete) responses of structural elements as described in (Azizinamini & Gull, 2012a). Further, IR test could be used to obtain signature of the structure at a given time and evaluate changes to the structure over time. Conducting IR test is relatively fast and mobility response of one duct for one segments, could be obtained in less than 10 minutes.

1.2.3 Infrared Thermography (IRT)

The Infrared Thermography (IRT) method has been validated in the laboratory and proven to be economically and technically viable to detect near-surface defects, such as near-surface voiding in grouted PT ducts (Pollock, Dupuis, Lacour, & Olsen, 2008). In this method, variations and disruptions to heat flow are used to detect surface defects on the test object. Both passive (natural heat flow) and active (applied heat) measurements are possible. The application of IRT in non-destructive testing (NDT) has increased due to the availability of cheaper and higher resolution cameras.

The method relies on the detection of the variations in the surface temperature profile, which are characterized in an infrared image captured with an infrared camera. Infrared radiation is emitted by all objects above absolute zero and the images taken from a thermographic camera distinguish objects based on the amount of radiation emission. The method relies on the detection of the variations in the surface temperature profile during transient heat flow. The thermal distribution pattern on the structure or its elements can be recorded and advances in digital thermal cameras allow for good precision in identifying localized anomalies. Other factors that must be considered include the geometry of the structure, thermal heating source, and reflection from other heat sources. Thermographic images can also show variations in temperature because the amount of radiation emitted by an object increases with temperature. Table 1-2 summarizes the inherent characteristics and applications of this technique.

Table 1-2: Summary of inherent characteristics and application of IRT

Advantages	Disadvantages	Best application case	Application with regard to duct type
• Rapid and convenient contact-less technique.	• Cannot provide meaningful information about internal ducts.	• Characterization of exterior duct or tape condition of duct on cable stays.	• Applicable mainly to cable stay ducts. • Likely not applicable to PT ducts of any sort.

IRT is a nondestructive surveying method that can be used to locate heterogeneities and surface defects on concrete structures. IRT is a rapid and convenient contactless technique, but it cannot provide meaningful information about internal ducts or other deeper defects. Further information on IRT is provided in Appendix A.

1.2.4 Magnetic Flux Leakage (MFL)

Magnetic methods make use of the interaction between magnetic (and associated electric) fields and their interaction with matter. Magnetic flux leakage (MFL) is the principal magnetism-based NDT method that has been applied to inspect distress in ferrous materials. Recent developments with static magnetic methods have shown improved capabilities to detect strand damage. The study performed has shown that the methodology can be used for detection of corrosion in PT concrete bridges (Ghorbanpoor, Borchelt, Edwards, & Abdel Salam, 2000). The method first was developed in late 1970s and has been subject to ongoing evaluation as sophistication of electronic instrumentation and data analysis techniques have improved.

The MFL method is a magneto-static measurement technique and is based on the application of an external magnetic field in vicinity of a ferromagnetic (steel) material to create magnetic flux lines to pass through the steel. The application of MFL to concrete structures is possible since concrete medium does not affect the measurements unless ferromagnetic impurities are present in the concrete. MFL method works by magnetizing a strand under an exciting magnetic field and the magnetic flux predominantly remains within the strand. In the presence of a geometric discontinuity such as a part of a corroded strand with loss of cross-section, the magnetic flux is deviated (leakage) and can be detected by magnetic sensors such as hall effect (HE) sensors (Figure 1-4**).** Excitation magnetic fields have been produced using a permanent magnet, an electromagnet or a solenoid depending on specific application. The HE sensors are made with semi-conductor crystals which when excited by a passage of current perpendicular to the face of the crystal, responds by developing an output voltage proportional to the magnetic field strength. Analysis of the leakage flux output signals can be used to detect the location and the size of the defect. The extent of metal loss can be identified by the corresponding intensity of the defect leakage flux signals.

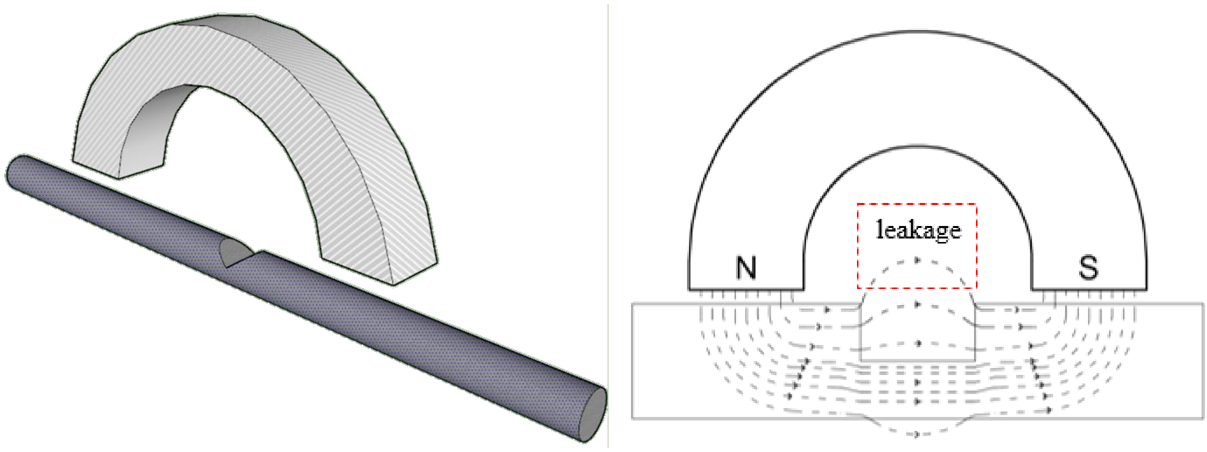

Figure 1-4: Magnetic flux leakage.

There are two primary methods for detecting the field anomalies using MFL. These methods are referred to as active and residual. In the active method, the specimen is magnetized initially and then the HE sensors are placed above a target area and between the poles of the magnet. For the residual method, the specimen is also initially magnetized but the HE sensors are placed without further magnetization of the specimen. In both methods, the output voltage of the HE sensors can be used to characterize the level of magnetization and changes in the magnetic field. Characteristics of the resulting inflection in the voltage curve can define the extent of the defect.

In the field, the application of MFL for investigating the corrosion of steel strands embedded in concrete presents challenges such as masking effect of the duct; the existence of different layers of reinforcement in the structure that cause disruption to the MFL signal; and limited access to areas, such as the anchorage zone, that are prone to corrosion activities.

Advancements in HE sensor size, accuracy and precision allow for the enhanced detection of small flaws on the steel. Furthermore, recent works have demonstrated that complications in signal analysis due to secondary ferromagnetic disturbances can be minimized (H Scheel & Hillemeier, 1997; Horst Scheel & Hillemeier, 2003; Xu, Wang, & Wu, 2012). Sawade et al. studied the limitation of MFL for detecting single wire ruptures in PT tendons and provided recommendations for improved inspections (Sawade & Krause, 2007). Using limited number of sensors, Szielasko et al. were able to test flat surfaces with high speed and resolution (Szielasko, Kloster, Dobmann, Scheel, & Hillemeier, 2006).

Table 1-3: Summary of inherent characteristics and application of MFL method

Advantages	Disadvantages	Best application case	What improvement can be made	Application with regard to duct type
• Can indicate local wire breaks (or member thinning) in near-surface tendons. • Established test method. • A contactless test that does not require connection to tendon. • Works for both metal and plastic ducts.	• Some expertise may be needed to interpret signals. • May need many magnetizing pre-sessions before signals are reliable. • Cannot detect break in underlying tendons, or in anchorage region.	• Identifying wire breaks in external, plastic ducts.	• Improved performance for congested steel sections and within anchorage region.	• Applicable to both internal and external ducts.

Improvements in the existing MFL methods have been made possible by finite element (FE) analysis which has allowed simulation of testing procedures to better understand the magnetic fields and its interactions. The FE analysis have complemented the experimental MFL and led to development of new improved electromagnetic devices. Naemi et al. compared the results of a 2-D and 3D FE analysis for defects on a test plate and despite the simplicity of 2-D models, higher flux density detected which may be inaccurate (Al-Naemi, Hall, & Moses, 2006). Zuoying et al. modeled a 3-D FE model for a pipeline and parametric study is carried out to analyze typical defects (Zuoying, Peiwen, & Liang, 2006). Based on numerical analysis, proposed positioning of sensor array at the front and back of probing device, the integration of signals from these sensors allows detection of a sample defect (Li, Tian, & Ward, 2006). Table 1-3 summarizes the inherent characteristics and application of MFL method.

1.2.5 Acoustic Emission (AE)

Acoustic Emission (AE) is a phenomenon of sonic and ultrasonic wave radiation in materials that undergo deformation and fracture processes. These ultrasonic waves are detected by an array of microphones or high frequency accelerometers. Arrival time of the waves to different sensors is used to triangulate the location of the fracture.

The corrosion process induces defects (in service wire fractures) in PT tendons, which generate acoustic emissions. These radiated “acoustic emissions” are detected by surface mounted sensors and the data acquired by several sensors is used to locate the defect and, in some cases, provide additional information about the defect. AE is well established technology and field studies have demonstrated its utility. Although the theory of this technique is simple and well established, the main problem in field application is to distinguish the emission caused by defects from ambient emissions. Only breaks occurring after the installation of equipment can be detected. Vibration sensors are strategically mounted on structural members. These vibration sensors are monitored to “listen” for fracture events due to corrosion of wire strands in the tendons. With multiple sensors, the locations of such events can be detected through triangulation, as illustrated in Figure 1-5.

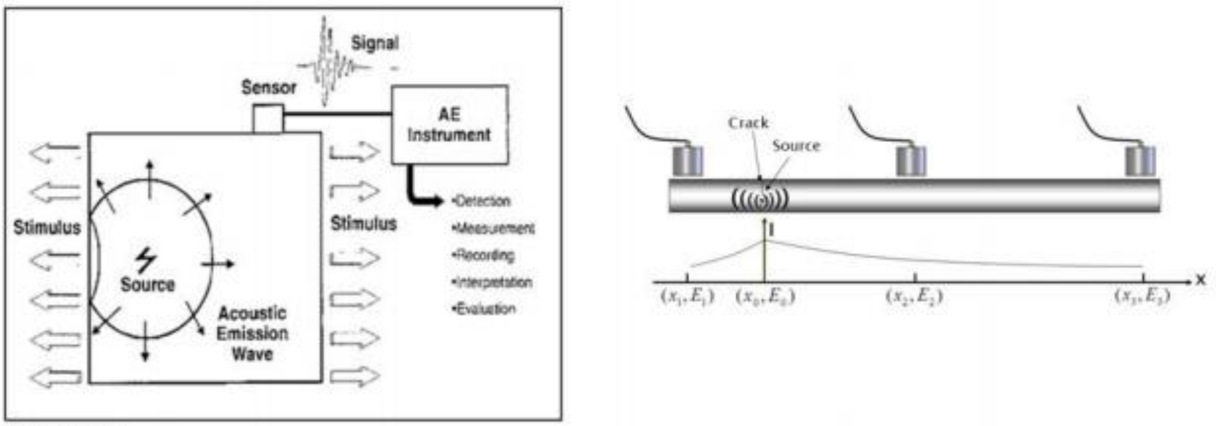

Mistras Group

Figure 1-5: AE concept (left) and source location with multiple sensors (right).

Table 1-4: Summary of inherent characteristics and applications of AE method

Advantages	**Disadvantages**	**Best application case**	**Application with regard to duct type**
• Can indicate occurrence of a wire break, and may indicate its approximate location. • Established technology.	• Expensive. • Process generates large volumes of data that can be difficult to manage and interpret. • Individual signal may be difficult to interpret or disrupted by noise, so some expertise is needed. • Cannot detect existing damage.	• Locating breaks in external ducts (either plastic or metal).	• Possibly applied to both internal and external ducts, and in both metal and plastic ducts.

Recent research shows promising results in detecting the onset of corrosion of bonded prestressing tendons. The researchers found that the expansion around steel at the onset of corrosion caused stress events in the concrete that were detectable. The challenge is to identify these small events in a bridge structure with many other sources of stress events. The researchers concluded that the AE could identify the source of corrosion (at least in the small specimens), and the cumulative signal strength of AE was a good indicator of the initiation, propagation, and development of corrosion. Table 1-4 summarizes the inherent characteristics and applications of AE method.

1.2.6 Interferometric Survey (IBIS-S)

Interferometric survey (IBIS-S) is a microwave radar sensor which is used to measure displacements from an array of points on a structure with an accuracy of a hundredth of a millimeter. The displacements can be useful to identify resonant frequencies and mode shapes. The IBIS-S is based on interferometric and wide-band wave form principles (Olson, 2010).

The components of IBIS-S consist of a sensor module, a control personal computer, and a power supply. The sensor module equipped with air horn antennas can generate, transmit, and receive electromagnetic signals. The air horn receives a series of discrete electromagnetic waves at regular intervals. The reflectors are installed on the structure and illuminated simultaneously by antenna beams which provides measurement of the line-of-sight displacements. The system has advantages of portability and robustness.

1.2.7 Inductance Measurement Method

The inductance testing method exploits the ferromagnetic properties of the steel prestressing strands within the tendon as a property which differentiates it from the surrounding concrete. Magnetic fields may be magneto-static, such as those created by a magnet, or they may vary with time as produced by an inductor energized by an alternating current (AC).

Inductance was recognized as an electrical characteristic that could be manifested in physical systems with steel components. The electrical behavior may be used as a metric for the relative amount of ferromagnetic material in bridge components such as post-tensioned tendons. Inductance may be described as a property of a circuit by which a change in current through the circuit induces an electromotive force in both the circuit itself and in any nearby circuits by mutual inductance. In the case of the NDT evaluation of internal tendons, an inductor probe coil paired with an inductance meter is placed on the concrete slab surface and energized with an AC current, and an expanding and contracting magnetic field is created which links to the steel strands inside the tendon to the probe coil by mutual inductance. Through mutual inductance, a larger amount of ferromagnetic material in the tendon produces a larger inductance and smaller amount of ferromagnetic material in the tendon produces a smaller inductance.

In addition to section loss, the inductance method also measures the additional inductance due to any additional mild steel reinforcement or conduit steel in the vicinity of the inductor coil. Inductance data plots from the bridge segment testing illustrate the abrupt rise in inductance due to the transverse reinforcement and transverse strands which were precast above the conduit at the time of fabrication. The transverse reinforcement therefore presents a limitation to the inductance method in these cases as the reinforcement shields the inductance meter from obtaining a true measurement of the inductance of the strands inside the tendon. Further information about the inductance method can be found in Appendix B.

2 RESEARCH OBJECTIVES AND APPROACH

2.1 RESEARCH OPPORTUNITIES

The project bridge (bridge number 860434) located in Fort Lauderdale exit ramp to SB US-1 was scheduled for demolition and to be used as a test bed by the FIU research team (Figure 2-1). A meeting was held on Feb 7, 2013 with the contractor (Tutor Perini Fort Lauderdale-Hollywood Venture) responsible for demolishing the bridge. Present in the meeting were Mr. John Danielsen and Mr. Alberto Sardinas of FDOT District 4; representatives of the FIU research team; and representatives of VSL, the contractor/consulting firm representing District 4. The main discussion centered on the schedule for demolishing the bridge and possibility of transferring a few segments of the bridge to the FIU. Following the bridge demolition, four segments of the bridge – each about 10-ft long were transferred to the FIU.

Figure 2-1: Bridge at Fort Lauderdale exit ramp to SB US-1.

NDTs, extensively carried out in laboratory and full scale structures, have provided important information regarding behavior of the structures. However, these methods have inherent benefits and limitations as explained in section 1.2. One of the possible ways to identify the deterioration of bridges with age is comparison of results obtained during periodic evaluation of bridges using NDT methods. However, depending on the type of specific structure and conditions, usually a considerable time is required for threshold deterioration to occur which could be identified by a specific NDT method. In addition, at the time of construction most of bridge structures lack a signature response which complicates the problem of damage identification.

In this regard, the demolition of Fort Lauderdale bridge provided an opportunity to conduct NDT on the (1) in-service bridge (2) testing during deconstruction and (3) testing on decommissioned segments of the bridge. This was an excellent opportunity to conduct tests that otherwise would be difficult to carry out on real structures or in a laboratory environment alone. The framework for research work involved carrying out multiple NDTs on the subject bridge and laboratory samples. Once the laboratory tests have been conducted, they can be verified by testing on test bed of decommissioned bridge segments. The purpose of the test bed segments is furnishing similar geometrical configuration of a bridge but may not necessarily imitate structural behavior of a PT bridge.

2.2 PRACTICAL APPLICATION OF NDT FOR FDOT

2.2.1 Observed Field Problems with Post-Tensioned Systems

PT concrete bridges can be very durable if properly constructed with high performance materials. Problems were found in grouted PT ducts in Florida during the late 1990s and early 2000s that indicated a change in grouting materials and construction practices, were necessary. Since that time, materials and practices have significantly improved. States that have investigated older PT bridges have found widely varying levels of deterioration depending on climate, construction practices, structure type and other variables. In the case of bridges built prior to around 2003, voided areas in the grouted tendons are common.

One of the early corrosion problems in PT structures was noticed during 1999 inspection of Niles Channel Bridge, the Mid-Bay Bridge, and the Sunshine Skyway Bridge in Florida (Beitelman, 2000; Harris, 2003; Powers, Sagues, Virmani, & Sagüés, n.d.). This led the Federal Highway Administration (FHWA) to issue a memorandum on January 12, 2001, alerting the State Departments of Transportation of serious corrosion problems with PT segmental concrete bridges, part of which reads: "… alert states to the PT corrosion problems and recommend the expedited inspection of their highest risk PT structures". Thus, several states have taken a lead in comprehending the corrosion challenges in in-service post tension and stay cable system, and developing advanced technologies.

Many of the problems associated with PT systems can be attributed to grouting which is used to protect corrosion of steel strands inside the duct. Figure 2-2 shows a typical cross-section of a duct with steel strands. Multi-level protection, as shown in figure, helps ensure long term durability of PT system. In general, the multi-level protection systems for steel strands are: (1) exterior surface, (2) concrete or epoxy cover, (3) duct, (4) grout, (5) strands' sheathing or coating, and (6) strand or bar.

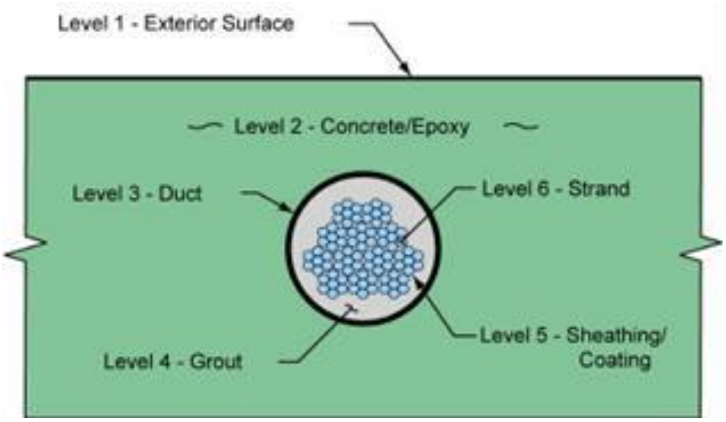

Figure 2-2: Multi-level corrosion protection of steel strands in tendons (Corven & Moreton, 2013)**.**

The final arrangement of the strands inside the duct after post tensioning is not necessarily centered, even in straight portion of the tendon. Figure 2-3 shows few examples of cross-section of tendons and final arrangement of the steel strands after post-tensioning. To an extent, the flow of grout depends on these final arrangements.

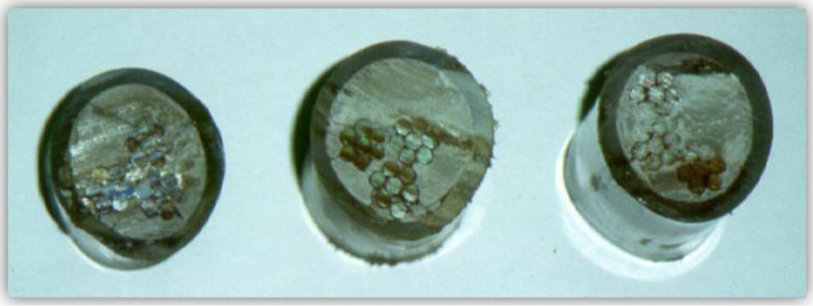

Figure 2-3: Final arrangement of steel strands inside duct after post-tensioning.

In PT systems there are two types of tendons, internal and external. The external tendons in segmental systems are used to provide: (1) primary tendons in span by span construction, (2) supplemental tendons in balanced cantilever bridge construction, (3) future tendons, and (4) added tendons for repair. The main elements of external duct system in segmental post tension systems (in span-by-span construction) are shown in Figure 2-4**.**

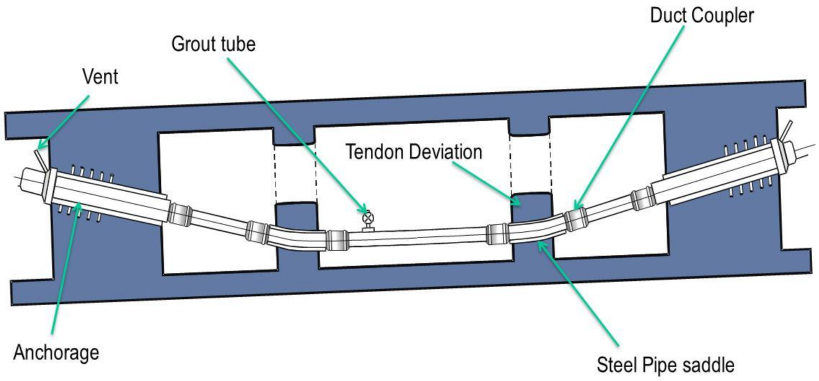

Figure 2-4: Elements of external ducts in segmental post-tensioning systems.

The length of duct, demand splicing, and duct couplers are used for splicing. Tendon deviators and anchorage blocks provide reaction for forces created by post-tensioning the strands inside the ducts. Anchorage devices are used for arresting the ends of the strands. Once the strands are post-tensioned, the ducts are grouted using grout tube and vents are used to allow the air to exit preventing formation of voids. Voids provide oxygen and moisture and can result in corrosion of the steel strands. Even though not shown in Figure 2-5, a concrete diaphragm over the pier is present in balanced cantilever construction. Other special details are used in segmental columns. Figure 2-5 shows an example of an external duct in post tension segmental bridge. In many cases the tendons are very close to bottom flange or web surfaces, as noted in Figure 2-5, which provide challenges for inspection.

Figure 2-5: External duct.

Major problems observed with external ducts are: (1) cracked duct, (2) grout voids, (3) un-set, wet, soft, and chalky grout, (4) contaminated grout, (5) strand corrosion, and (6) tendon failure. The existence of void does not necessarily translate to having corrosion at those locations. Figure 2-6 (left) and Figure 2-6 (right) show examples of strand conditions in vicinity of voided areas in duct.


1/24/2001

Figure 2-6: Corrosion activity in voided area (left) lack of corrosion activity in void area (right).

Figure 2-7 shows examples of cracking of the duct. These observed cracking are mainly related to old duct types used and were not created by grouting process. Cracking is mainly attributed to age and durability of the types of materials used. In some cases, corrosion of strands is observed at the vicinities of duct cracking. This is especially true when steel strands are exposed at cracked locations.


10/13/2000
9/27/2000

Figure 2-7: Examples of types of observed cracking of ducts.

Since early 2000, the practice has improved significantly and substantial attention is being paid to training workers, quality of materials used, and documentation of construction activities. Currently there are number of checks and balances in place that significantly reduce the chances of corrosion. Nevertheless, some of the solutions that were thought to resolve the corrosion problems are creating additional challenges. For instance, grout is used to prevent corrosion of steel strands in PT concrete bridges. Types of grouts used have gone through significant changes since early 2000’s. Ducts or stay cables are filled with cementitious material. Most recent grout types used by the FDOT are proprietary products. Recently corrosion issues have also surfaced using new proprietary grout types. For instance, Figure 2-8 shows the cross-section of a tendon where a new grout type was used. Recent thinking among some practitioners is that most recent corrosion problems observed in the field could be attributed to ingredients used in the grout. More specifically certain characteristics of the grout and grouting practices, which includes (1) high chloride content, (2) high water demand for new grout types, and (3) high pressure that is used during grouting process.

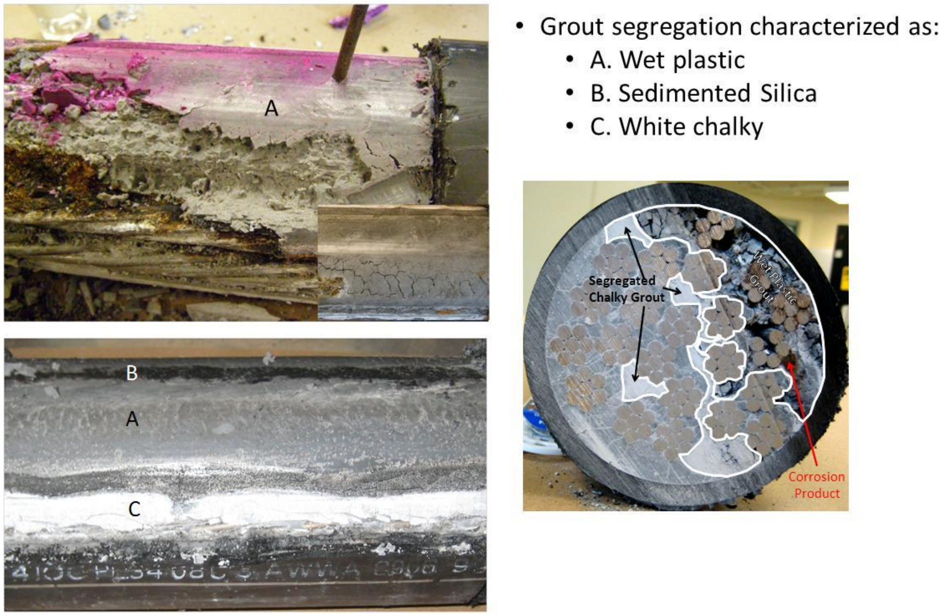

Figure 2-8: Condition of grout ten years after construction (photo courtesy of FDOT).

The segregation of grout in Figure 2-8 is characterized by having three types of solids, (1) region where grout is still wet, even after 10 years of construction (wet plastic); (2) grout with sedimented silica, which is because of segregation; and (3) white chalky grout, which is somewhat hardened, but lacks the characteristics of a superior grout. The grout conditions shown in Figure 2-8 are mainly observed at high points of the tendons. Corrosion of strands is shown to be strongly related to locations where grout was segregated.

2.2.2 Practices to Assure Durable PT Systems

Because of observed corrosion issues with PT systems, state DOTs have made significant changes in their practice. Quality of grout, workmanship, and hardware used has improved significantly. Fortunately, the level of redundancies and safety factors used in design are high enough that the observed corrosion issues have not created significant public safety concerns. FDOT implemented new policies and procedures to enhance the long-term durability of their PT bridges in 2002. These policies and procedures were developed through extensive research highlighted in a ten-volume publication titled “New Directions for Florida Post-Tensioning Bridges” (Corven Engineering, 2002). The following five strategies have been adopted for providing corrosion protection for PT bridges: (1) enhanced PT systems, (2) fully grouted tendons, (3) multi-level anchor protection, (4) watertight bridges, and (5) multiple tendon paths.

One of the major improvements from past practice is the use of plastic duct. Field performance and research has indicated that galvanized metal ducts offer little corrosion protection. Plastic ducts, on the other hand, as shown in Figure 2-9, provide an added layer of protection. Further, plastic ducts are air and watertight. The quality of grout prior to 2000 was not good. Use of new and proprietary grout types are now the norm with many DOTs.

Figure 2-9: Plastic ducts.

Field observations indicate that one of the major areas of corrosion is at the anchorage areas. Thus, newer generations of anchorage systems are being developed, which are believed to resolve corrosion issues in the anchorage areas. Figure 2-10 and Figure 2-11 show the new and old generations of anchorage devices, respectively. It is worth mentioning that many states no longer permit use of older generation of anchorage devices.

Figure 2-10: New generation of anchorage devices.

Figure 2-11: Older generations of anchorage devices ─ not permitted by some states.

Similar to multiple protection layers for steel strands, recent practices are calling for multiple protection of anchorage regions, as shown in Figure 2-12.

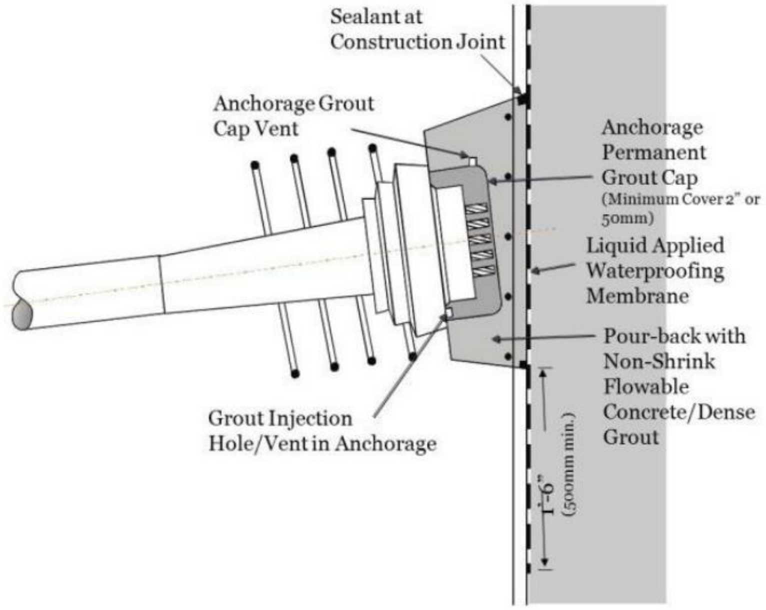

Figure 2-12: Multiple layer protection system for anchorage regions.

For present practice (in the future, use of un-grouted duct may be a feasibility as it will be easier to inspect and replace strands), the quality of grouting and workmanship is very important. The “Specification for Grouting of Post-Tensioned Structures”, by Post-Tensioning Institute (PTI), provides comprehensive guidelines for grouting. This document is presently undergoing updates. The key elements for good grouting practices are: (1) being able to completely filling the duct, (2) low permeability, (3) appropriate bleed resistance, and (4) careful use of admixtures.

2.2.3 Formation of Advisory Panel

The FDOT has had a history of corrosion damage of PSC bridges as early as the 1990s to current practice. As a response to corrosion degradation, continual changes in bridge design and detailing as well as in material specifications reflect the need for effective condition assessment evaluation. In attempt to define the current and future needs of the department for effective in-situ material testing as well as to provide means to identify maintenance requirements, the investigators coordinated with district and state FDOT personnel and industry consultants. The members of the project advisory board during the time of the project are given in Table 2-1.

Table 2-1: Advisory board

Principal Investigator	Project Manager
Atorod Azizinamini Professor and Chair Department of Civil and Environmental Engineering Florida International University 10555 W. Flagler Street Room 3602 Miami, FL 33172	**John Danielsen** District 4 Maintenance Engineer Florida Department of Transportation 3400 West Commercial Boulevard Fort Lauderdale, FL 33309
Advisory Panel	**Consultant members**
Fred Ochoa District 4 Structures Design Engineer Florida Department of Transportation Phone: 954-777-4693 **Alberto Sardinas** Special Projects Manager Florida Department of Transportation, Phone: 954-777-4175 Email: Alberto.Sardinas@dot.state.fl.us **Mario Paredes, PE** State Corrosion Engineer State Material Office Florida Department of Transportation Phone: 352-955-6690 Email: mario.paredes@dot.state.fl.us **Ivan Lasa** State Corrosion Mitigation Technologist State Material Office Florida Department of Transportation Phone: 352-955-2901 Email: ivan.lasa@dot.state.fl.us	**Luis M. Vargas, PhD, PE** URS Corporation Southern 7650 Corporate Center Drive, Suite 400 Miami, Florida 33126 305-514-2423 Direct 305-261-4017 Fax luis.vargas@urs.com **R. Craig Finley, Jr., P.E.** Managing Principal Finley Engineering Group, Inc. Phone: 850-894-1600 Email:craig.finley@finleyengineeringgroup.com

2.3 PROJECT OBJECTIVE

Problems such as poor workmanship and inadequate grouting increases the failure probability of PT tendons and raise questions about the integrity and performance of post-tensioning tendons in existing concrete segmental bridges. Corrosion causes deterioration of tendons and reduces the strand cross-section thereby affecting their strength and potentially affecting the ability of the structure to carry load. This subject prompted FIU to take the opportunity to carry out some field tests before and after the deconstruction of a bridge scheduled for demolition.

The main objective of the project was to carry out limited NDT in the field on the segmental concrete bridge prior to its demolition to evaluate the merits of NDT techniques for (1) condition assessment of segmental concrete bridges, (2) corrosion detection, and (3) evaluation of the merits of different approaches that could be used during biannual bridge inspection to detect major changes in the structural characteristics of segmental concrete bridges. Further, several tests were to be carried out on segments that were transferred to the FIU to evaluate the ability of NDTs to detect corrosion in internal tendons. Most of these technologies were identified in a recently completed project conducted by FIU and sponsored by the FDOT (Azizinamini & Gull, 2012b). This report provides a description of the NDT procedures used by the FIU research team and Olson engineering to evaluate an existing concrete bridge.

One of the spans of the bridge was to be tested using IR tests to collect mobility response of the segment while being part of the bridge. If successful, IR could be used to obtain the local and/or global signature of the bridge and be used to assess changes in the structural characteristics of the bridge over time. Recent findings of deficient grout materials in Florida PT tendons, characterized as soft and segregated grout for which IRT was thought to be a promising tool to locate local grout anomalies. Field and laboratory exploration of IRT would serve to determine feasibility for application of the technique for inspection of segmental bridges. Defects in internal tendons would be considered by field and laboratory tests using the MFL and inductance methods. The conditions to be considered for the MFL and inductance methods include the cross-section loss, the depth of strands with defect, and effect of secondary reinforcement on the signals.

2.4 GENERAL RESEARCH APPROACH

An in-service bridge scheduled for demolition provided research opportunities for evaluating the service condition and carrying out NDT on the bridge. The subject bridge constructed in 1980s has been functional for almost 35 years, and based on nominal design service life, it can be assumed that the components of structure may have undergone varying levels of damage and/or corrosion. The stiffness of a PT structure can reduce due to the continual degradation mechanisms affecting concrete and steel.

Although, rupture of strands is uncommon in real PT structures, the change in stiffness due to rupturing of a strand can provide an overview of resultant change in structural behavior. The sequential demolition of the bridge involved cutting PT internal tendons, which caused loss of stiffness of the structure. The sequential demolition procedure can provide data of decrement of strength/stiffness of the bridge which can be useful information for comparative study on a bridge evaluated over a period.

The sequential deconstruction of bridge was of significance from the stand point of construction safety, possibility of on-field testing (and compare test results with expected and actual behavior) and extraction of segments to be used in conjunction with laboratory tests. Finley Engineering Group, Inc. provided calculations and drawings for the deconstruction process, temporary works, and rigging for the deconstruction of a segmental bridge. An analytical study was carried out by Finley Engineering Group, Inc. for deconstruction procedure by modeling a construction sequence of a balanced cantilever bridge and calculating the final stress levels taking into consideration effects of creep and shrinkage due to the 30-year service time frame. Based on these stresses, the sequential decommissioning was analyzed. The structural analysis described in the section 3.4 was done as part of the bridge deconstruction. This information was deemed useful to develop test methodologies for NDTs that were to be conducted on-site at different phases of demolition.

Most of the elements of PSC bridge, especially ones deteriorating over time are embedded inside concrete such as reinforcement, tendons and PT anchorage system. Due to limited capabilities of NDT techniques and inaccessible surfaces, providing a complete detail of structure’s health is a difficult task. The decommissioning and demolition of the bridge provided an opportunity to inspect individual elements and exposed surfaces of bridge. The visual inspection on these elements provides important information. Although no on-site NDT was applied on the demolished portion, the post-deconstruction survey of these elements is briefly discussed in section 3. The project involved decommissioning of bridge segments by cutting which were to be used as a test bed for future segment testing at FIU. These segments do not imitate in-service structural condition and were only to be used as a test bed.

One of the objectives of the project was to conduct various types of structural monitoring and on-site field on the bridge prior and during its demolition. These on-field NDTs employed sensors as discussed in section 4 provided various signals (deflection, acceleration, etc.). These on-field test results were analyzed to evaluate the possibility of correlating the changes with the results (such as deflections) from numerical study explained in section 3. Although not inconsistent, the on-field tests had same general behavior as predicted by the numerical study and these results may be helpful in bridge inspection.

The post-destruction survey of the bridge helped identify some ducts with deficient grout and corroded strands. To further investigate these problems, additional laboratory tests were carried out on deficient grout and corroded strands as explained in section 5. In addition to laboratory tests on strands, the segment test bed was used to replicate similar geometrical configuration as that of a service bridge. One of the purposes of using the decommissioned segments was to evaluate the merits of various technologies on full-scale geometry. For this purpose, laboratory tests were carried out which provided baseline results that were extended to segment testing.

3 DECOMMISSIONING OF PT SEGMENTAL BOX GIRDERS

3.1 BRIDGE SEGMENT DETAILS

A project bridge, located in Fort Lauderdale (bridge number 860434), was constructed in early 1980s. The bridge served as an exit ramp from the Fort Lauderdale airport to SB US-1. Figure 3-1 shows a bird's eye view of the bridge. The bridge was designed as a PT, pre-cast segmented, continuous girder with three spans (125.58 ft,152.52 ft, 95.9 ft).

Figure 3-1: A bird's eye view of the exit ramp (left) and side view of bridge (right).

An additional runway at the airport necessitated changes to highway geometric layouts resulting in removal of the bridge. The bridge was scheduled for demolition in mid-May of 2013 and was used as a test bed. The central span was the focus of research since its removal was performed piece-by-piece so that the normal operation of live railroad tracks was not affected. The demolition procedure was performed using a diamond impregnated cable wire saw to cut the bridge segments that were then removed by crane.

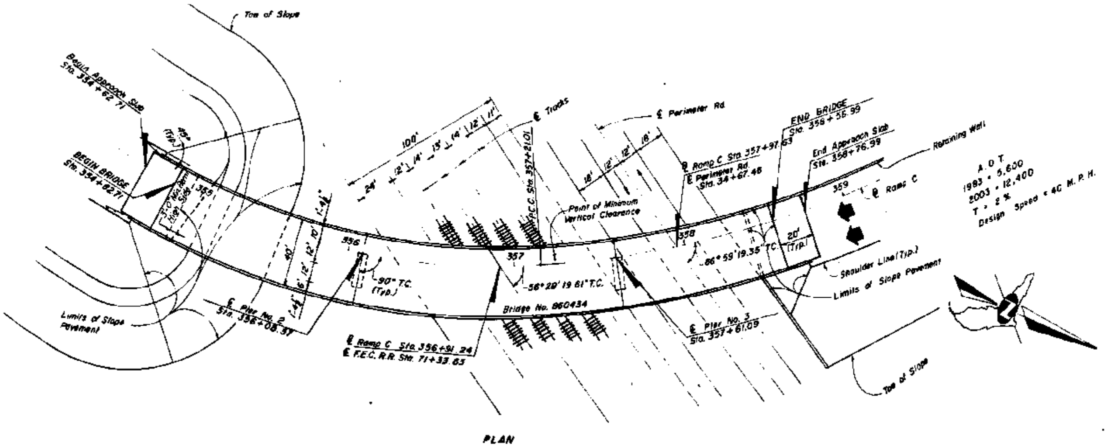

Figure 3-2: Structure plan view.

The geometric roadway axis followed a compound curve consisting of two radii; 400 ft., and 600 ft. The plan view of the structure is given in Figure 3-2.

3.2 DECONSTRUCTION SEQUENCE

The deconstruction sequence plan was engineered by Finley Engineering Group, Inc. To properly evaluate the in-service structural condition of the bridge, the model by Finley Engineering Group, Inc., included a simplified construction sequence. To account for any locked-in effects, a time-dependent calculation was run. The construction sequence of the bridge was simulated, as per the plans, using the balanced cantilever method. Once the construction was finished, the effects of creep and shrinkage due to the 30-year service time frame were evaluated putting the structure in its current state so that the stress levels could be investigated. The deconstruction sequence was modeled step-by-step, as to produce accurate results ensuring stability and capacity at each stage. The AASHTO LRFD bridge design specifications, 2010 were used in the analysis (AASHTO, 2010). Figure 3-3 shows the box girder cross-section.

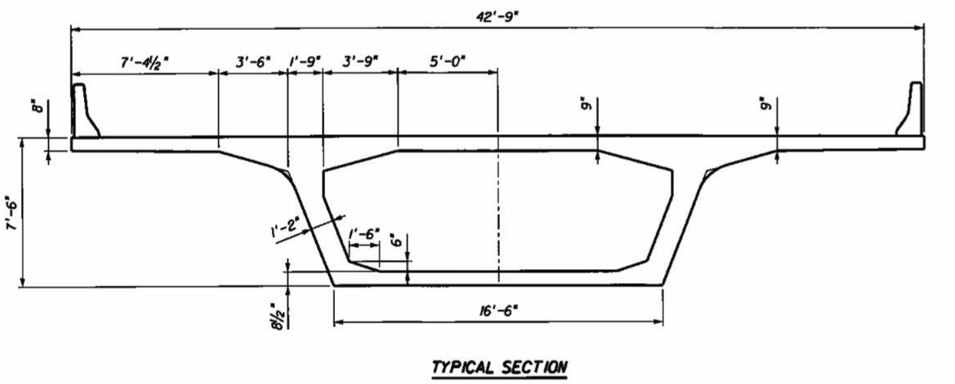

Figure 3-3: Dimensional drawing of typical box girder cross-section.

The original deconstruction sequence proposed by Finley Engineering Group, Inc., made use of a crane positioned on the bridge deck. However, due to site constraints and crane availability, it was decided that all lifting could be done with the crane on the ground. However, the general deconstruction sequence did not change. The deconstruction sequence proposed by Finley Engineering Group, Inc., is presented in the following steps:

Step 1: The wings of the box section were cut off to reduce the total weight of the lifting sections. Photos from the actual operation are shown in Figure 3-4.

Figure 3-4: Cutting off box wings on both side of the bridge.

Step 2: After the structural braces were placed to support the structure, the first wire saw cut was performed at the center of span 2 through the closure pour from top to bottom as shown in Figure 3-5. Prior to making the cut, shear transfer beams (green beams seen in Figure 3-5 (right) were placed across the cut location to prevent relative movement of the two segments during the cutting operation. Once the cut was complete, these beams were removed. This first cut at the center of span 2 went through multiple PT grouted ducts and was of primary interest to the research team since severing the tendons affects the structural behavior of the bridge.

Figure 3-5: Wire saw cutting at middle of span 2 (left) and shear transfer beams (right).

Step 3: The segments of structure were sequentially removed from span 2 as shown in Figure 3-7. The segments were demounted from the structure using an on-ground crane. Once the segments from the first half of span 2 were removed, the crane was transported to the other side of the rail road tracks and the segments from the other half were removed in a similar manner. Also, identified in Figure 3-6 are the segments that were to be transported to FIU for further testing.

Figure 3-6: Piece-by-piece removal of segments.

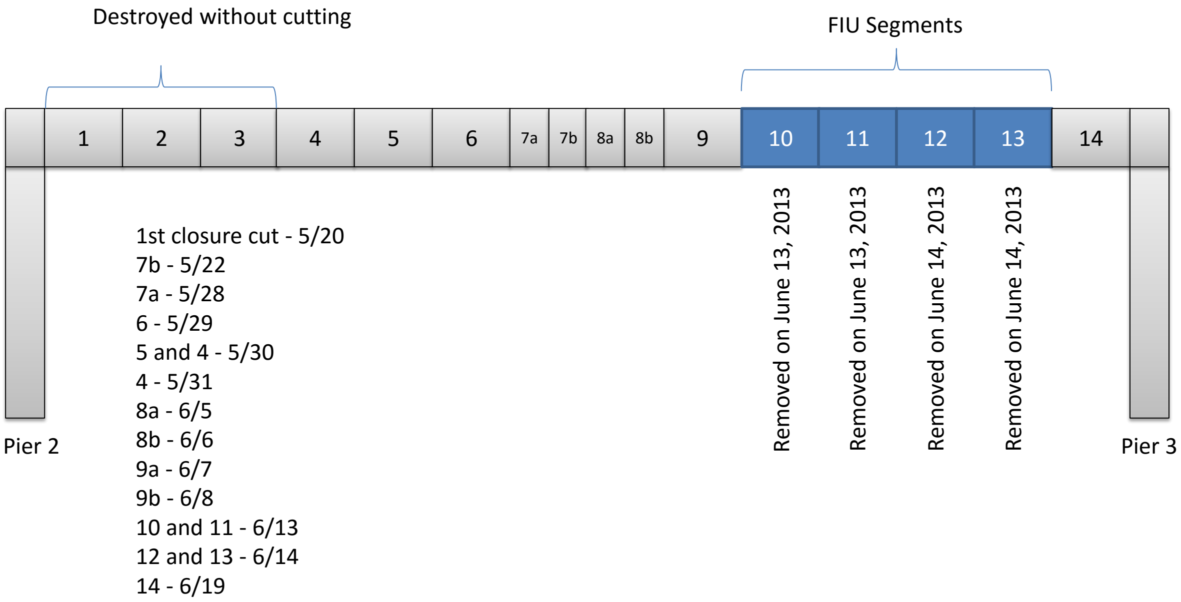

Figure 3-7: Segments of span 2 which were removed for testing.

Step 4: Once removal of segment from span 2 was complete, conventional methods were used to demolish the remainder of the structure, shown in Figure 3-8**.**

Figure 3-8: Concrete crusher demolition procedures.

3.3 POST-DECONSTRUCTION SURVEY

Cutting span 2 segment by segment allowed the FIU research team to perform an investigation of the post-tensioning system for voids and honeycombing in the concrete. Figure 3-9 shows photos of the duct exposed during the demolition. It is clear that voids exist in the ducts. These voids are where corrosion can easily occur.

Figure 3-9: Some ducts were fully grouted, and some other ducts were partially grouted.

Figure 3-10 shows the end anchorages that were used in the structure and Figure 3-11 shows the abutment and pier after demolition of the superstructure.

Figure 3-10: Post-tensioning anchor and strands after demolishing of the bridge.

Figure 3-11: Remaining structure after bridge demolition.

In some cases, strands and anchoring system were completely intact and the duct was fully grouted, but in other cases the ducts appeared partially grouted with strand showing some signs of corrosion. That corrosion did not appear to be severe. The overall condition of the post-tensioning system including anchoring system, strands, and grout inside of the ducts were in good condition, with no deficiencies.

3.4 DECONSTRUCTION MODELING AND ANALYSIS

For the safe demolition of the bridge, RM V8i software was used to model the bridge. RM is structural analysis software allows for analysis and design of PT concrete in 3-D space, as well as the time-dependent behavior of the structure. This bridge was modeled longitudinally as a single line of beam elements. Due to poor readability of the available plans and drawings, several assumptions of dimensions, loading, materials and geometry had to be made, which were generally based on the common practice of 1980s era. Removal of each piece was defined as separate load case to provide complete stress level control for the superstructure. The deconstruction sequence was checked for service level stresses.

During deconstruction, the structure undergoes several changes that affect the stress levels and force distribution within the bridge. Mid-span cut, deconstruction stress in the top slab over the pier 2 and 3, deconstruction stress in the bottom slab over the segment joints, and superstructure stability checks were also provided during the analysis. Also, RM automatically calculated the forces along each tendon during each stage of construction. For the superstructure stability, all support points were investigated to provide stability during deconstruction.

3.5 FULL-SCALE GIRDER TEST-BED SETUP

3.5.1 Transportation and Logistics

The bridge segments were cut and removed from span 2 of the bridge in July 2013. The process of cutting the segments and transferring four units took place in a short span of almost one week to minimize the interference with on-going construction activities at the Fort Lauderdale airport expansion project. This created a challenging situation and demanded a temporary storage of the segments off-site before placing them in their permanent location at FIU. Therefore, the research team arranged with Titan America to temporary store the units at their facility while platform to place the segments at FIU was being completed.

Figure 3-12: Storage of segments at Titan America yard (left) and transport to FIU (right).

The segments which were identified to be brought to FIU are shown in Figure 3-6. FIU hired G&R Mineral Services (Miami, FL) to for the transportation of bridge segments from the bridge to Titan America and from Titan America to FIU. Two lowboy flatbed trucks were used to transport the segments as shown in Figure 3-12. Each segment weighed about 50 tons and is 10-ft long. Two cranes having load capacity of 300 tons were used for loading and unloading the bridge segment. Special care was taken to prevent any potential damage to the segments during transportation.

3.5.2 Setup at FIU

The principal investigator of the project discussed the setup with advisory panel of the project. As per discussions, the segments needed to be placed at least 2-ft above the ground to have room to pick up the segment with hydraulic rams while maintaining access to the bottom of the segments for potential usage in non-destructive tests. This required building pedestals on which segments could be placed. FIU staff decided to use temporary concrete barriers (32-in high) as pedestals (Figure 3-13).

For storage of segments, a 50 ft x 35 ft x 0.75 ft slab, was constructed at FIU. After the construction of the slab, the bridge segments were transferred to FIU Engineering Center in July 2014. There was concern about the elevation difference at the top of the barrier. This elevation difference could result in improper seating of bridge segments on the barrier. Therefore, to prevent the segments from rocking/swaying between the barriers, bearing pads were attached to the top of barriers to allow proper seating. Bearing pads were sized to keep stress below the design stress level for bearing pads.

Figure 3-13: Concrete barriers to serve as pedestal for bridge segments.

Bridge segments were cut from curved portion of the bridge. The segments would align along a curved path when placed next to each other. Therefore, it was necessary to layout the barriers, on which segment were to be placed next to each other, to follow a curved path. Also, imperfections during cutting process resulted in unequal segment lengths. Therefore, actual dimensions of the segments were measured and combined with clearance between the segments to come up with a layout for the barriers and bearing pads as shown in Figure 3-14. Further, it was decided to keep 2-in clearance between the adjacent segments. This 2-in gap was necessary for picking up the segments. The segments are shown with the shaded area and number as 1, 2, 3 and 4 for their proper arrangement.

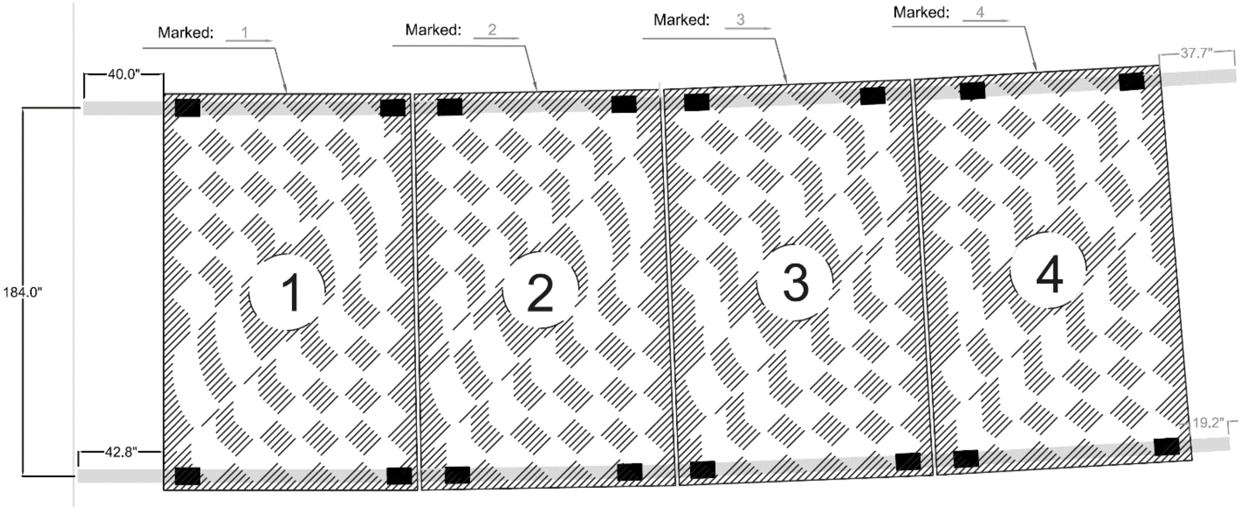

Figure 3-14: Segment numbering and placement on barrier.

Erection plan was prepared for transferring the segments from Titan America yard. Prior to transfer date, FIU staff numbered the segments and identified the sequence of the placement. An attempt was made to line up the ducts as close as possible, however, unequal pick up slings attached to the crane made it difficult to align the segments perfectly. Figure 3-15 shows photos of the bridge segments taken during their placement. Minor cracking was observed in the barriers during the segment placement which were possibly due to non-uniform slab surface on which the barriers were placed. The segments seated on the bearings perfectly and did not rock between points of contact with bearing pad.

Figure 3-15: Photos taken during placement of first segment (left) and last segment (right).

4 ON-SITE FIELD TESTING

4.1 IMPULSE RESPONSE (IR)

4.1.1 IR Test Methodology

The objective of the impulse response (IR) tests was to evaluate the capability of IR tests in capturing the overall change in stiffness of the structure. Two IR tests were conducted on deck of span 3 of the Bridge under different conditions. The first test was conducted on April 27, 2013 during which the bridge was closed to traffic. For an easy access to inside of the box structure, two access holes 2 ft x 3 ft were cut in the bridge deck, one near Pier 2 and another near Pier 3. The bridge was in its service condition except for these two access holes that had been cut into the bridge deck. The access holes were small compared to size of the bridge and therefore it was assumed to have negligible effect on the global stiffness of the bridge. Figure 4-1 shows a photo of the bridge taken during the first test indicating the general testing procedure.

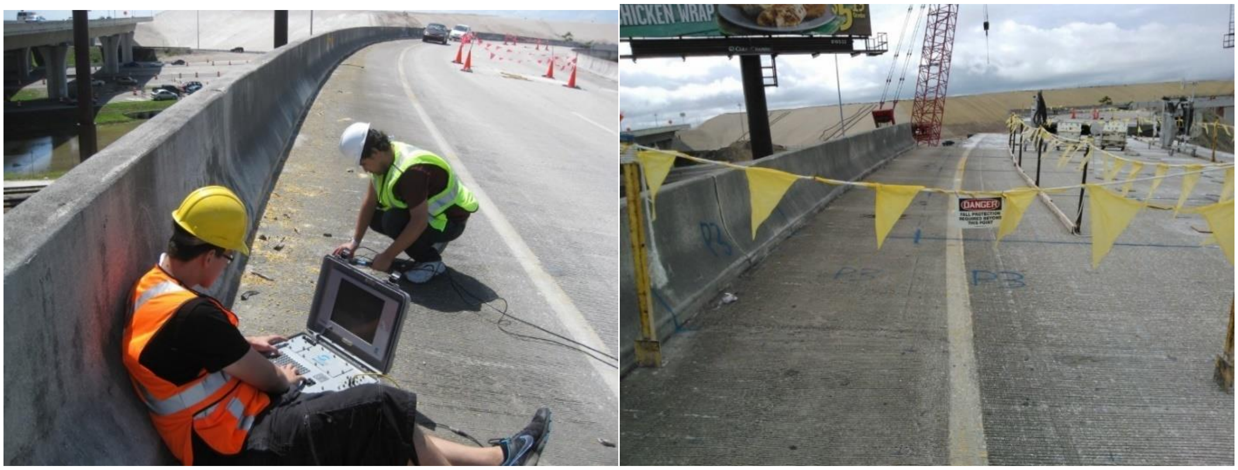

Figure 4-1: Bridge photo before (1st test on April 27, 2013) and after cutting wing wall and removing bridge segments (2nd test on June 01, 2013).

The second test carried out on June 01, 2013 was conducted after partial deconstruction of the bridge. At the time of testing, seven bridge segments of about 50 ft total had been deconstructed between Pier 2 and Pier 3. Prior to removal of these segments, the wing walls on either side had been removed from the span. These deconstruction procedures led to a decrease in the global stiffness of the bridge. This decrease in the global stiffness was shown by an increase in the mobility of the bridge deck measured by IR tests as discussed in the report.

A grid layout, marking the locations of IR measurements, was laid out on span 3 as shown in Figure 4-2. IR measurement were taken at every grid point and therefore the grid point number indicates the IR measurement number. Grid spacing normally ranges between 20 in and 78 in. However, different grid sizes can be used along the length and width of the bridge depending on the variations in sections in those directions. Figure 4-2 shows the grid used for the deck of span 3. Due to the curved bridge geometry, the grid size can differ on outer and inner arcs which does not significantly affect the test results if an appropriate grid size is chosen.

Grid size or the number of measurements taken during IR test affects the time required for inspection significantly. Time for laying out the grid needs to be considered when calculating the total time of inspection. A dense grid can significantly increase the time required for conducting the inspection. Table 4-1 shows different grid sizes, the corresponding number of measurements and an approximate time required for inspection. Based on the time available and the details that needed to be captured, an appropriate grid size of 36 in x 36 in was chosen. The estimated time required for each point is about 30 s which includes 3 hits followed by acceptance or rejection of the measurement by observing the data and gain.

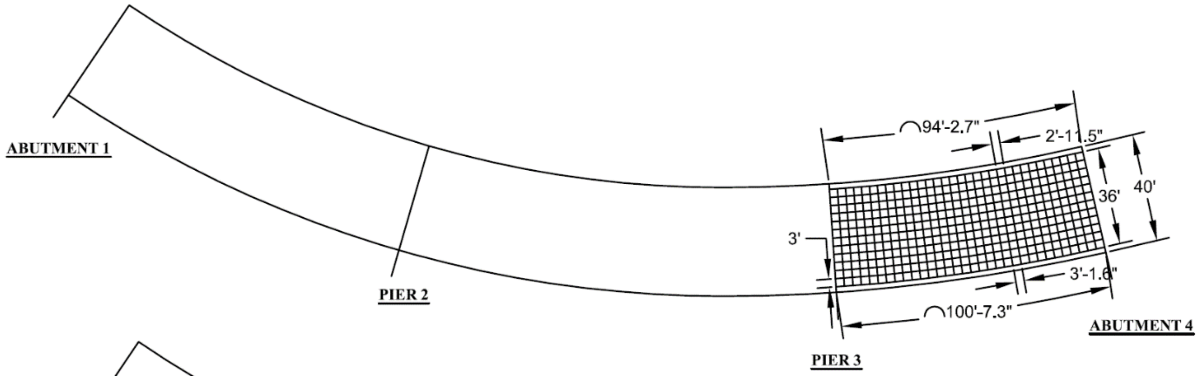

Figure 4-2: Grid on bridge deck for conducting IR test.

Table 4-1: Different grid options for conducting IR test on span 3 of the bridge

Option	Grid Size (ft)		No. of points along		Total Number of Points	Approx. Time @30 sec/point
	Length	Width	Length	Width		
1	4	4	96 / 4 = 24	40 / 4 = 10	24 x 10 = 240	2 hr 20 min
2	3	3	96 / 3 = 32	40 / 3 = 13	32 x 13 = 416	3 hr 30 min
3	2	2	96 / 2 = 48	40 / 2 = 20	48 x 20 = 960	8 hr 00 min

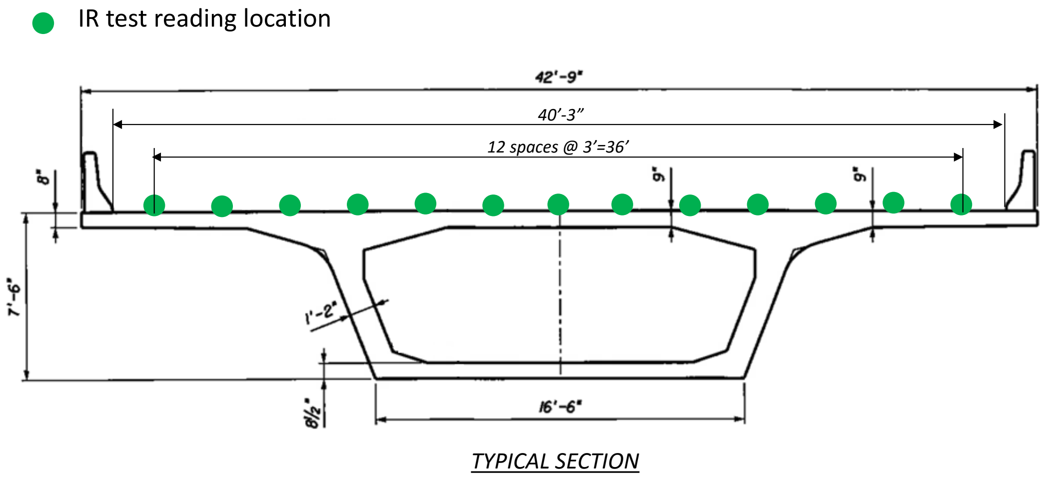

Figure 4-3: Measurement locations along the cross-section and bridge geometry.

Portable IR testing equipment from Olson Instruments, Inc. was used for conducting the IR test. A detailed description of the equipment and procedure to carry out the test are described in the system reference manual (Olson Instruments Inc., 2008). The measurement locations shown in Figure 4-3 were optimally spaced to capture different details.

A 3 lb hammer with a load cell is used to impact the deck surface and a geophone is used to measure the velocity of deck vibration resulting from the hammer impact. The impact generates transient waves in the concrete test element which sets up flexural and other vibrational modes of the element in the vicinity of the test point. The data from the hammer and geophone is collected through a portable computer (PC) unit with a built-in data acquisition system. One person places the geophone on the point of measurement and strikes with the hammer at approximately 4 inches (±1) from the geophone. Some pressure is applied to geophone by hand while hitting the hammer to prevent shaking of geophone during the hit. The second person checks the data on the PC unit and ensures the quality of reading. At least two readings or hits are required to complete one measurement.

Figure 4-4 shows a sample of the data displayed on the computer unit screen after a hit. The first graph on the top shows the time series of velocity of vibration recorded by geophone. The other two graphs in the picture shows the coherence and mobility spectrum. Each hit can be accepted or rejected based on the following:

1. Amplitude of velocity during the vibration should be decreasing with time. If not, it indicated sources other than the hammer are causing vibration of the deck or geophone and the reading can be rejected.

2. Coherence appears after the 2nd hit and any onward hit. It shows agreement between the data obtained from two consecutive hits. Ideally, coherence should be close to one for a frequency range of 50 Hz to 2,000 Hz. Small discrepancies may be acceptable based on judgment. However, if coherence is not close to most of the frequencies then the reading can be rejected.

3. The scale of the reading indicating amplitude of vibration or the force used for hitting the hammer should be 10% to 90%. A value less than 10% indicates vibration velocity data has very small amplitude and value greater 90% indicates potential data clipping due to high amplitude. The force used to strike the hammer can be adjusted based on the scale shown on the screen.

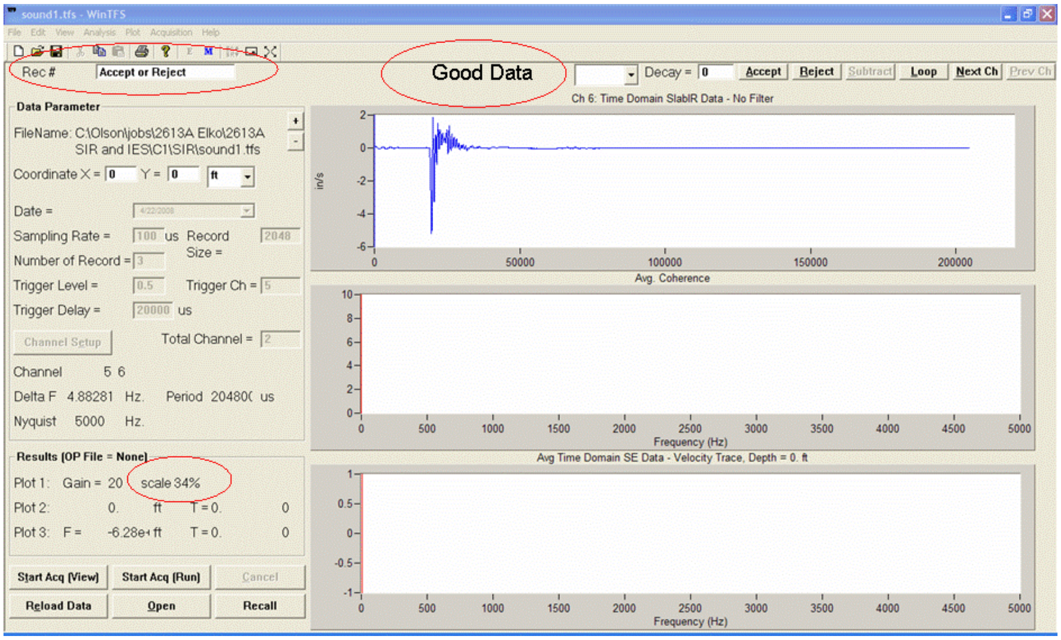

Rec # Accept or Reject

Data Parameter

FileName: C:\Olson\jobs\2613A Elko\2613A SIR and IES\C1\SIR\sound1.tfs

Coordinate X = 0 Y = 0 ft

Date = 4/22/2008

Sampling Rate = 100 us Record Size = 2048

Number of Record = 3

Trigger Level = 0.5 Trigger Ch = 5

Trigger Delay = 20000 us

Total Channel = 2

Channel 5 6

Delta F 4.88281 Hz. Period 20480(us

Nyquist 5000 Hz.

Results (OP File = None)

Plot 1: Gain = 20 scale 34%

Plot 2: 0. ft T = 0. 0

Plot 3: F = -6.28e‹ ft T = 0. 0

Figure 4-4: Velocity waveform after a hammer strike (Olson instruments, 2008).

4.1.2 IR Test Results

The force and velocity waveforms were recorded and subjected to digital signal processing to obtain the mobility spectrum at each test point. Key parameters were computed from the mobility spectra at the test points and displayed in the form of contour plots from which the likely locations of anomalous regions can be identified. For all the test points on the grid, the average mobility obtained before and after the partial demolition are plotted in Figure 4-5 and Figure 4-6, respectively. In these figures, the two horizontal axis are distance along the length and width of the bridge and the vertical axis is the average mobility (in / s / lb).

The mobility is indicative of flexibility of the structural element at the test point. A high value of mobility indicates high flexibility, or low stiffness, of the structural element at the point of test and vice versa. The contour plots in Figure 4-5 and Figure 4-6 show three ridges (regions of high mobility) that correspond to the middle of the deck between the two webs and the two outer edges of the deck.

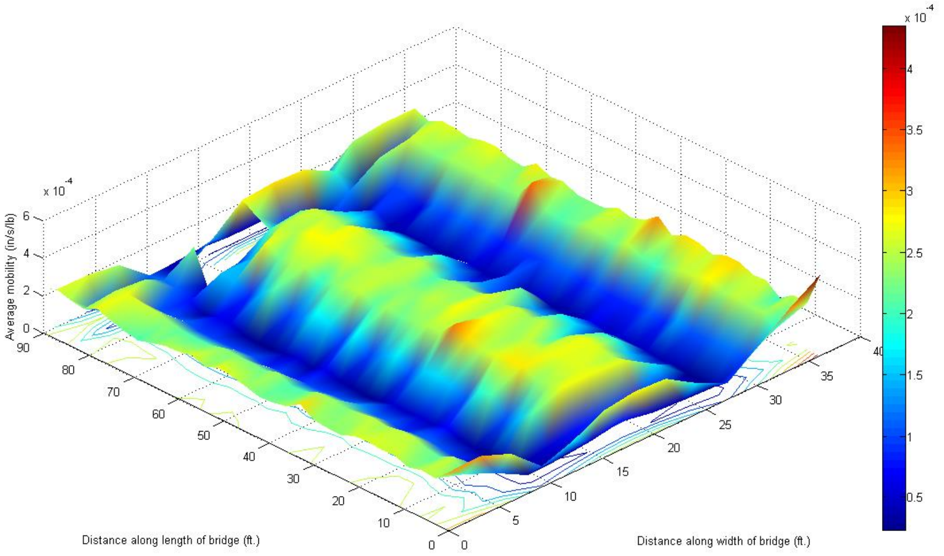

Figure 4-5: IR test result before partial demolition (1st test on April 27, 2013).

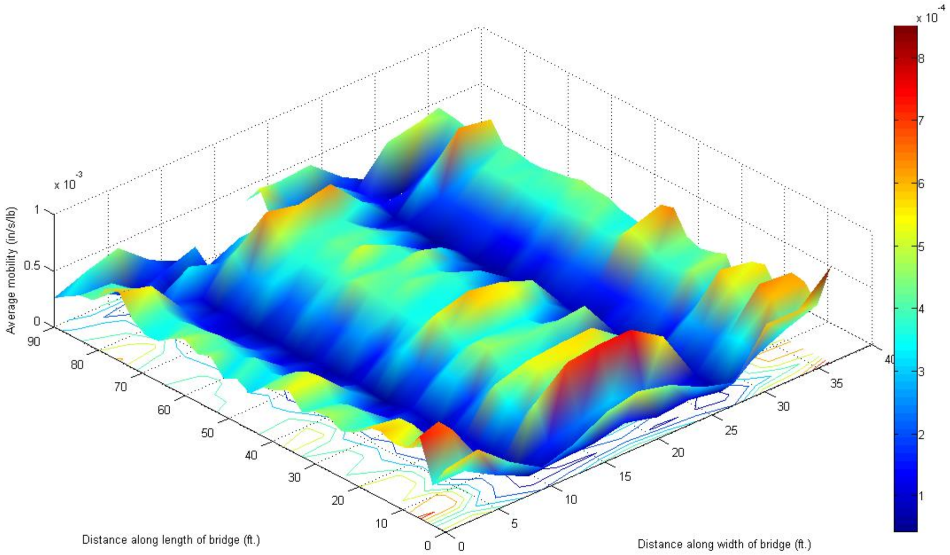

Figure 4-6: IR test result after partial demolition (2nd test on June 01, 2013).

This fact is more clearly illustrated in Figure 4-7, which shows mobility across the width of the bridge over a typical cross-section of the bridge. Mobility values are low near the junction of the deck to the web of the section. High mobility values are noticed at the middle and edges of the section. At the connection of deck and webs of the box, we have more thickness and the mobility decreased in these regions. The reason is reduction in plate thickness corresponds to a large increase in mean mobility, because flexural rigidity is proportional to the thicknesses raised to the third power.

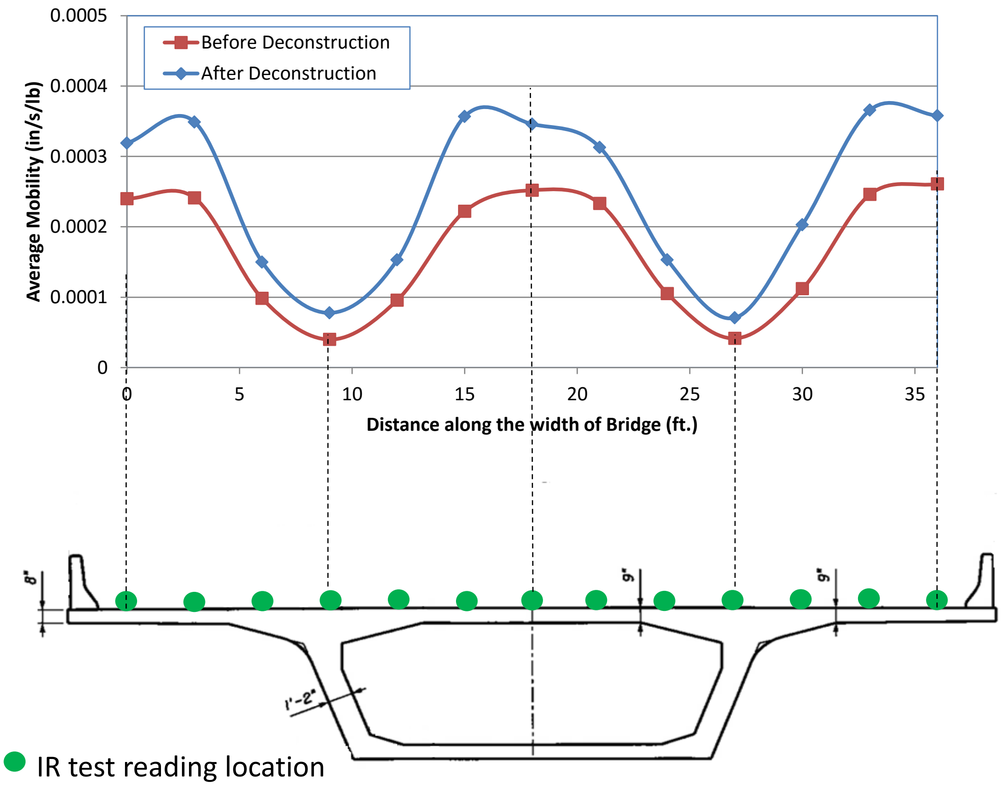

Figure 4-7: Mobility along the bridge width at 45 ft along the length of span 3.

Figure 4-7 also show mobility curves for the first test (before demolition) and second test (after demolition). The blue curve shows that mobility in the second test is higher than the red curve, which plots mobility in first test. This may arise from a decrease in global stiffness of the bridge system due to the partial deconstruction at the time of the second test. A similar increase in the mobility of the bridge along the length of the bridge is observed in Figure 4-8, which plots similar data for the centerline along the length of the bridge.

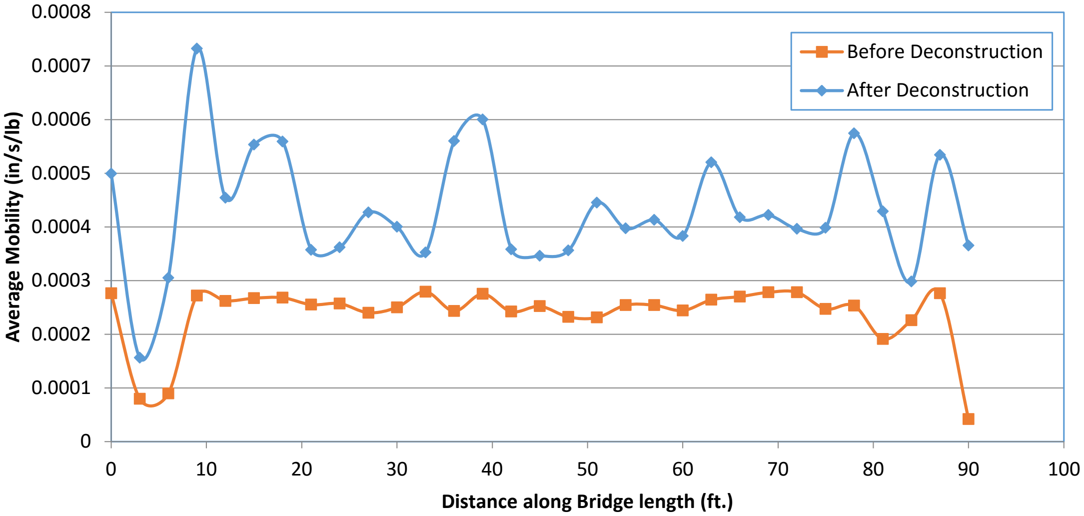

Figure 4-8: Mobility along the length of span 3 of bridge at the middle of section.

The variations in the mobility along bridge width is due to inconsistent thickness of deck in this direction. The thickness of deck along the length of the bridge is consistent, therefore, the average mobility does not have large variations.

4.1.3 IR Test Summary

Results of the two tests carried out before and after the partial deconstruction of the bridge show an increase in the mobility of the bridge after the deconstruction. The deconstruction reduced the global stiffness of the bridge and this was captured by the IR testing. The bridge signature can be obtained by conducting an IR test on a newly constructed bridge and then compared to an IR test later during the service of life of the bridge to evaluate the health of the bridge. The bridge needs to be closed for conducting an IR test, therefore making the IR test quicker and automated to avoid traffic disruption remains a challenge.

4.2 INFRARED THERMOGRAPHY (IRT)

The IRT tests were conducted on the segmental concrete bridge scheduled for demolition. The objective of IRT tests was to evaluate the merits of IRT testing in condition assessment of segmental concrete bridges. It was proposed to carry out IRT tests on the bridge and on segments of the bridge retrieved during its deconstruction.

4.2.1 IRT Test Methodology

The geometry, structure type, and location of embedded PT tendons provided challenges to obtain useful results by IRT testing. Any practical data recorded with a portable infrared camera would require adequate heating and subsequent cooling of the concrete and embedded elements. Safety issues during demolition of the bridge prohibited exposing anchors and applying any type of active resistive heating to the steel tendons. Therefore, feasibility of obtaining useful thermal data from passive ambient heating and cooling was assessed.

As heating and differential cooling was among important testing parameters, the possible temperature range that could be obtained in ambient summer conditions in Florida was to be obtained. The bridge deck had the greatest exposure to sunlight and provided ease for access to the bridge being demolished in an active construction site. Four test locations on the textured bridge deck were considered for test as shown in Figure 4-9 and Figure 4-10 along with the camera setup. Locations A and D were fully exposed to sunlight while locations B and C were covered with a plastic tarp to create a shaded covered surface. The testing was timed after a rain event and the covered regions provided ability to keep the concrete in a moist condition while comparing thermal response due to drying in the uncovered regions.

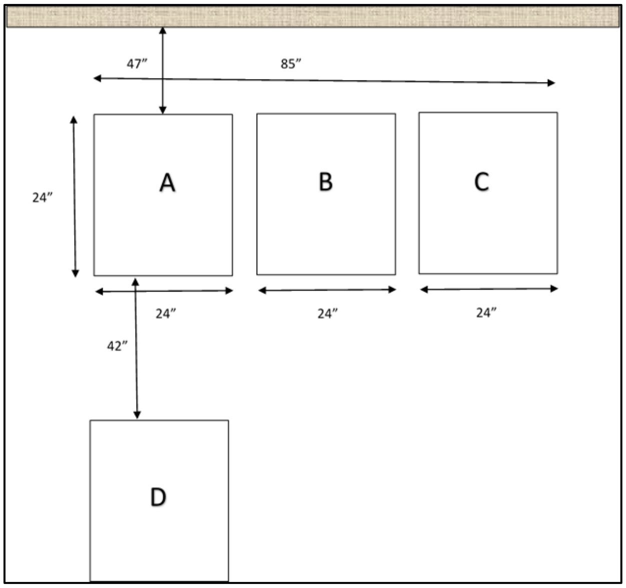

Figure 4-9: Schematic of surface IRT.

Figure 4-10: Surface infrared testing site (left) and thermal camera setup (right).

The textured deck surface complicated the drying conditions, the thermal camera was set at pre-marked locations for thermal testing and recordings were made in a time interval of several hours. Figure 4-11 (left) gives the surface temperature readings for each test location after approximately 2 hours and ambient air temperature using thermometer given in Figure 4-11 (right).

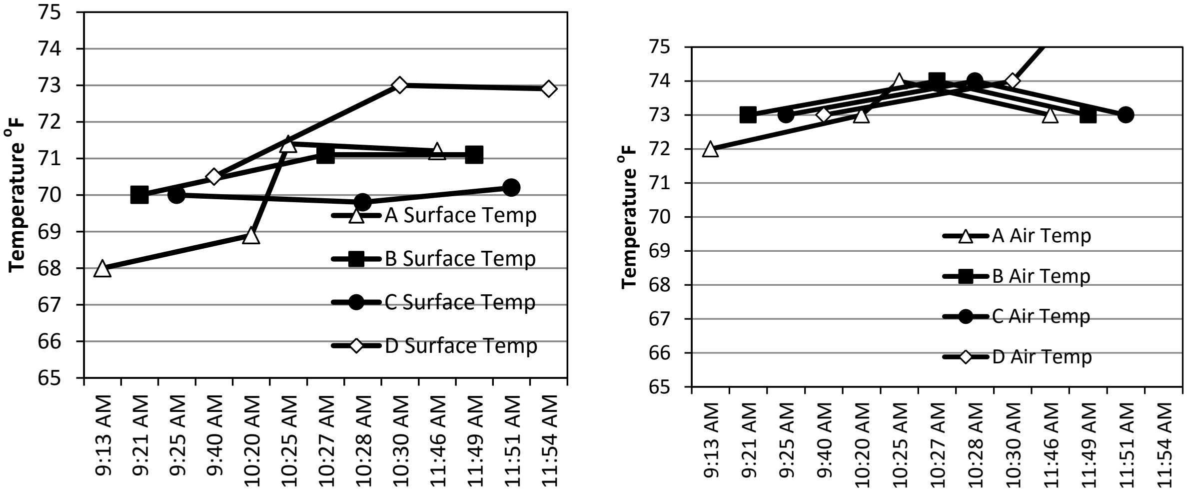

Figure 4-11: Evaluation of surface temperature from infrared camera (left) and ambient air temperature from thermometer (right).

4.2.2 IRT Test Results

The texture on the bridge deck was apparently visible in the thermal images in Figure 4-12 and Figure 4-13. The images at point A and B as well as the surface temperature evolution in Figure 4-11 (left) shows the expected temperature increase due to ambient heating. Whereas the uncovered deck surface increases to near ambient air temperature, the covered regions remained a few degrees cooler than the covered regions indicative of the shading and partial moisture retention.

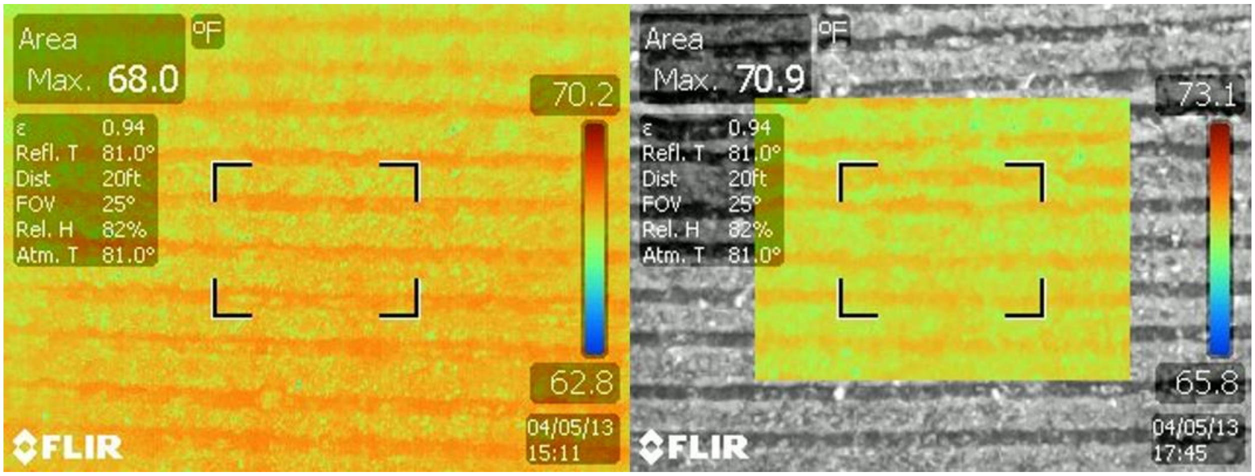

Figure 4-12: Recorded thermal image at point A at 9:13 am (left) and 11:46 am (right).

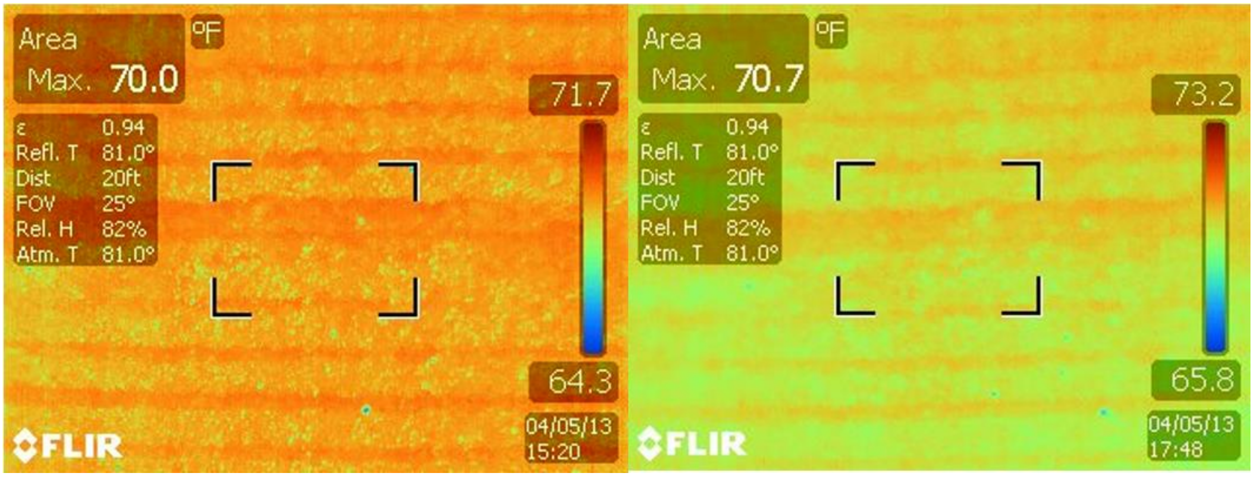

Figure 4-13: Recorded thermal image at point B at 9:21 am (left) and 11:49 am (right).

Figure 4-14 shows sensitivity of the thermal camera to differences in temperature. Test locations can be seen in the figure with A in red and C in dark blue. In natural heating condition, it is shown that differential cooling conditions can be achieved. However, the lack of apparent defects at the concrete deck did not allow for discrimination for surface anomalies.

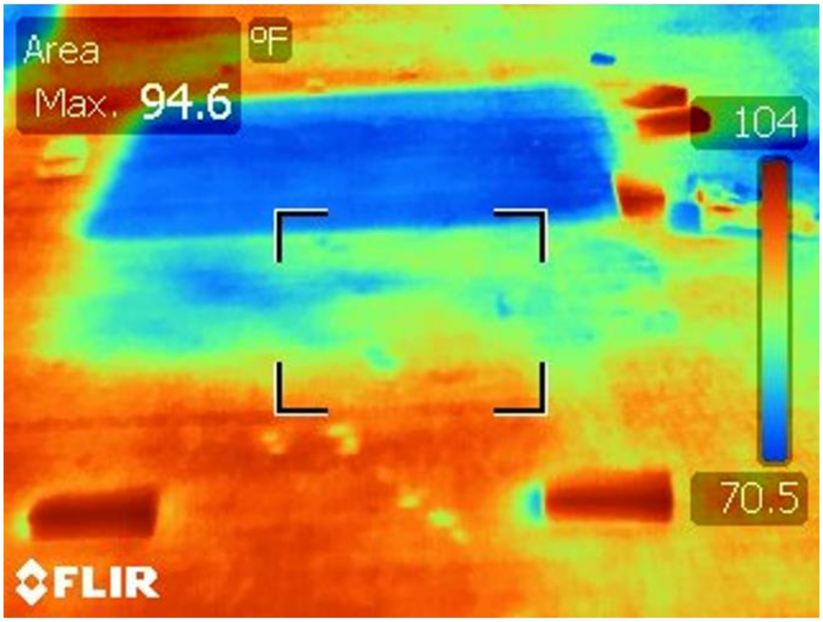

Figure 4-14: Thermal image of test site. Colors show differential surface temperatures of test locations A-C where the cooler covered regions are shown in blue (~70°F); the warmer exposed surfaces are shown in orange/red (~73°F).

A typical infrared image is shown in Figure 4-15. Features readily visible include the lane striping, drainage hole and segment joints. Variations in moisture on the deck and barrier walls were apparent as well.

Figure 4-15: Typical infrared image on bridge deck.

Of interest was the detection of differential cooling of the bulk concrete in the bridge segments as captured from below the bridge. As shown in Figure 4-16, hotter temperature regions were seen at regular spacing on the bottom of the box girder. These locations were attributed to tendon deviators. It was apparent that cooling was slower for locations with larger concrete masses such as the deviators.

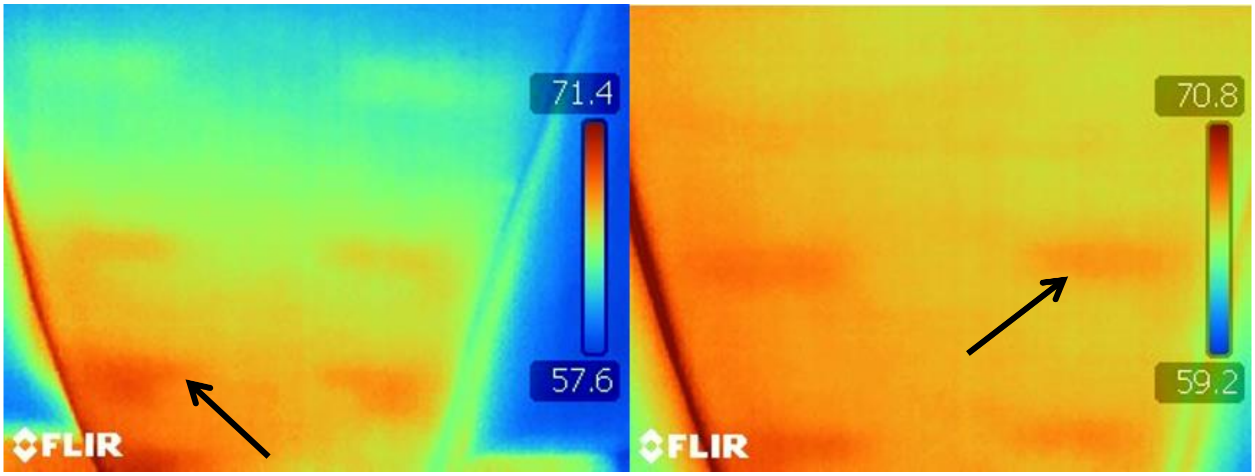

Figure 4-16: Infrared image of bottom of bridge segments captured from below bridge deck. Arrows point to expected locations of concrete deviators.

Testing could not reveal placement let alone deficiencies in the internal PT tendons. It was deemed that the tendons embedded in the segment as internal tendons provided significant challenges, specifically allowing for significant heating and differential cooling by passive heating by ambient natural conditions.

Rudimentary active heating and IRT measurements were conducted on bridge demolition debris after initial cutting of portions of the deck to provide access into the bridge segment. Steel wires were exposed at the cut surfaces of a rectangular portion of the deck removed from the bridge. A butane torch was used to heat one end of the wire in a rectangular concrete section. Interestingly, the heating of the rectangular concrete section showed effective and uniform heating of the whole section rather than differential heating of the steel wire. The thermal image showed heat transfer through the concrete slab from a 1-point heat source. Cooling of the section likewise showed uniform heat transfer throughout the slab with no indication of differentiation for the grout and wires.

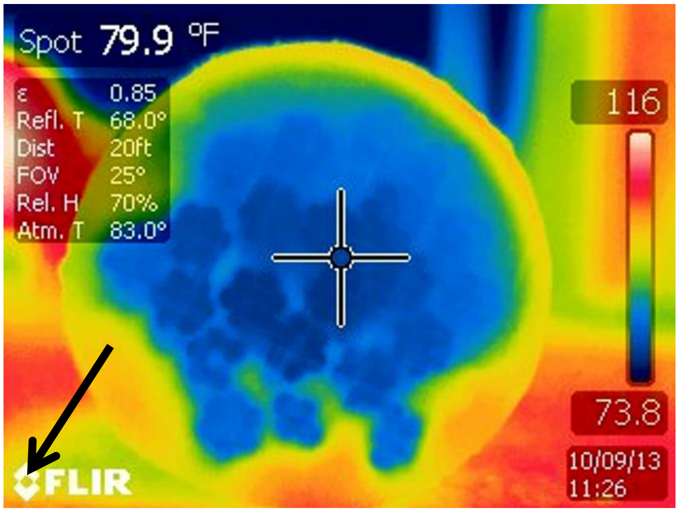

Figure 4-17: Infrared thermography of tendon cross-section with deficient grout. Arrow shows location of deficient grout.

Optimistic IRT evaluations were made on a tendon cross-section that contained deficient grout. The tendon cross-section was completely sealed with several layers of masking tape yet differentiation of the underlying materials can be seen by passive heating of the tendon as shown in Figure 4-17. Individual strand bundles are clearly differentiated. Furthermore, a contour in the bottom portion of the tendon in the image shows where there was deficient grout. These results provide possible utility of the technology to assess grout deficiencies which is further investigated in laboratory tests given in section 5.1.2**.**

4.2.3 IRT Test Summary

IRT as a non-destructive technology has major challenges for practical implementation in the field especially for internal tendons. However, observations of deficient grout materials in Florida bridges, especially segregated grout, continue to create need for further evaluation of diagnostic tools for maintenance decisions. The large amount of moisture associated with segregated grout continues to make IRT a NDT of interest; however, application of the technology in-situ in field application at this time has not been easily implemented. The experience with IRT for internal tendons by passive heating does have significant challenges in collecting data. It is believed that the technique would be better suited for testing of external tendons, but field verification is still needed. The major challenges include providing safe and reliable means for active heating and to reduce test aberrations due to thermal reflections.

4.3 ACOUSTIC EMISSION (AE)

Acoustic emission (AE) has been used to detect wire breaks in PT structures and studies have shown that it has more potential for fully prestressed structures than reinforced concrete structures. The results of these studies were directly related to the grouting condition around the tendons (Taghinezhad, Gull, Pham, & Olson, 2017). AE signal sometimes become difficult to interpret due noise. In this project, attempt was made to reduce the noise in the AE signals by carrying out calibration tests and by using different signal filtering techniques. Further, a 3-D model of the segment was used to look at propagation of acoustic wave through the geometry of the bridge segment.

4.3.1 AE Test Methodology

AE monitoring can locate the source of an event such as strand breakage. The test method principle is basic, in that when a significant and discrete vibration event occurs it is measured by the sensor array. Eight high-frequency accelerometers (10 kHz and 50 kHz) were used detect AE from wire breakage as shown in Figure 4-18. The accelerometers were arranged in two rows 19.5 ft apart. The location of wire-cut (tendon breakage location) and distances between the sensors are shown in Figure 4-19. The accelerometers were mounted on the bridge deck by attaching a steel fender washer to the concrete deck using an epoxy. The accelerometers were then attached to the steel washer using a strong magnetic base, which is threaded directly into the accelerometer.

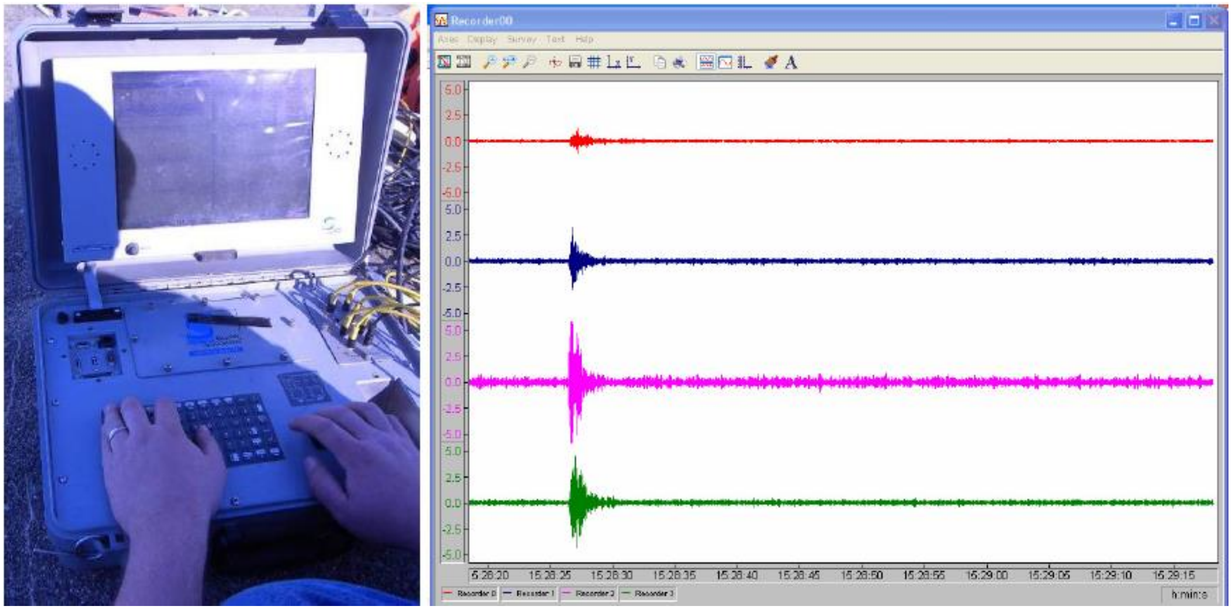

Figure 4-18: Olson Instruments Freedom Data PC with 8-channel accelerometer input module (left) and screen shot (right) of nominally 1-minute-long DASYLab record of an AE event on channels 1-4.

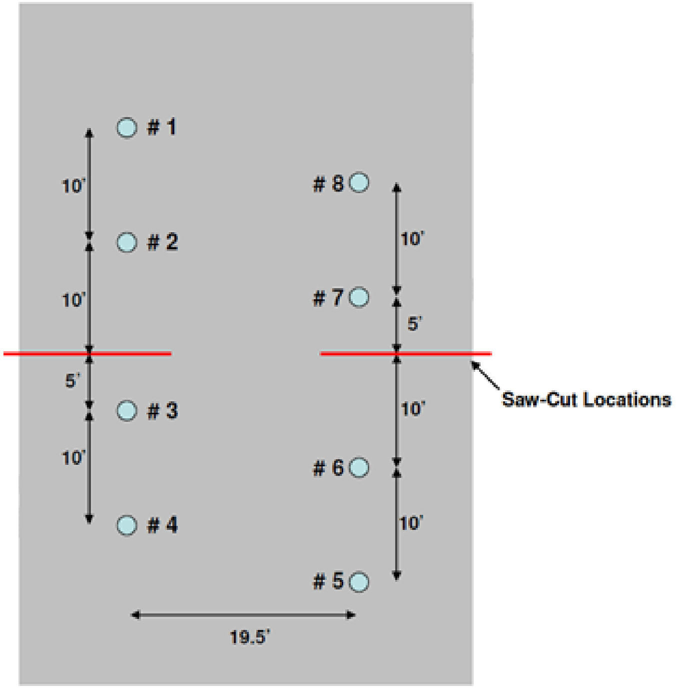

Figure 4-19: Plan view schematic of accelerometer array layout (not to scale).

The induced vibration triggered the acquisition system and was measured by the mounted accelerometers. Figure 4-20 shows a screen shot of one of the data acquisition software used (SHM by Olson Instruments, Inc.) which presents the resulting vibration on all 8 accelerometer channels due to a hammer strike.

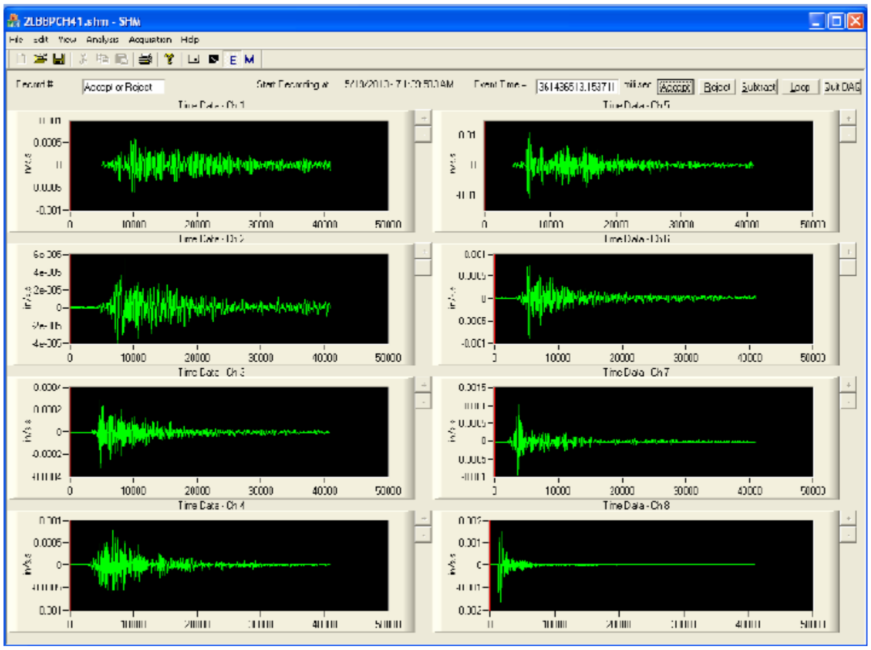

Figure 4-20: Example accelerometer data acquired during trial testing with an impact hammer source at the channel 8 accelerometer location.

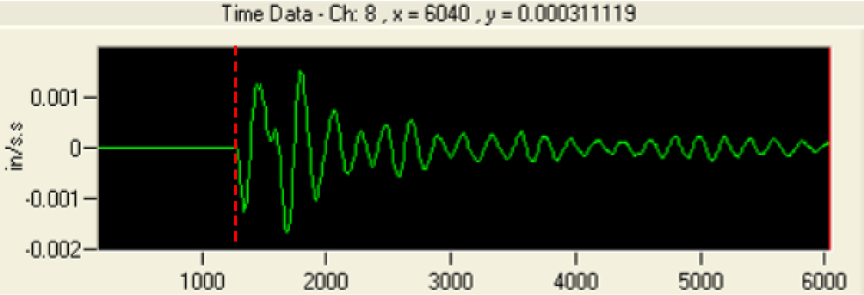

Source distance <1 ft, no clear distinction between P-wave and S-wave arrival

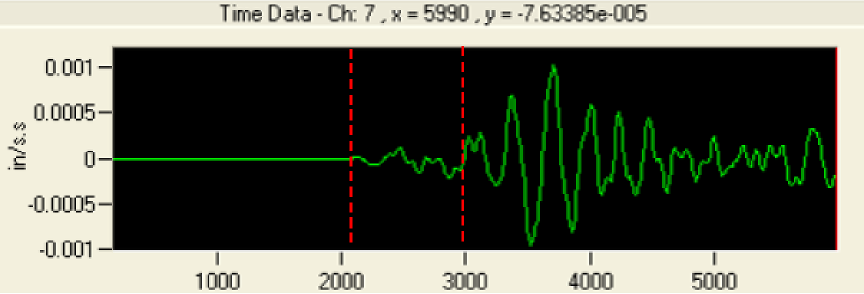

Source distance ~10 ft, and distinct P-wave and S-wave arrivals

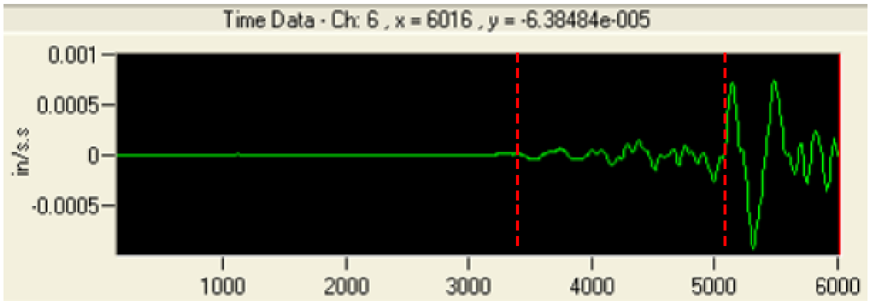

Source distance ~25 ft, distinct P-wave arrival at 6016 microseconds and S-wave arrival at about 5,100 microseconds.

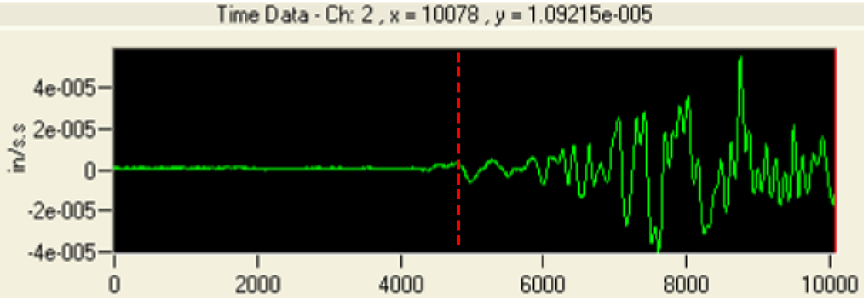

Source distance ~37 ft, less distinct arrivals, difficult to determine S-wave arrival time without knowledge of the source location

Figure 4-21: AE signals detected by accelerometers at different distances from source.

Once the vibration data was captured, the next step was to determine the wave arrival time at each sensor location. It is these arrival times that are used to triangulate the position of the vibration source. In this case, a 2-D planar surface is assumed with a single homogeneous material (velocity). An impact source such as the hammers used in this trial as well as the PT tendon breaks, induce both primary compressional wave (P-wave – the fastest initial arrival) and shear wave (S-wave – second larger amplitude arrival) energy into the structure. The major challenge in selecting the wave arrival time is to determine if the wave arrival selected is the P-wave or S-wave. Either wave type can be used for source location; however, it is important to select the same wave type on all channels for any given event. The S-wave component is approximately 62% of the velocity as the P-wave component. The ability to distinguish the P wave and S-wave from each other depends on a number of factors, the most critical being distance to the source and background noise level. It is important to notice that background noise can have a large effect on data in AE testing. Figure 4-21 display example of waves arriving with varying source to receiver distances and events shown by vertical dashed line cursors.

As displayed in the figures, the plots of acceleration are in in / s^2 and time in microseconds. Note that in the data immediately prior to the source induced vibration, background vibration levels were extremely “quiet” with virtually no vibration noise for the out-of-service bridge. The low noise level also aids in the identification of the wave arrivals, particularly the P-wave. Twenty-five separate trial tests were performed using hammer impacts as the source location. Both a metal ball-peen style hammer as well as a plastic tip instrumented hammer were used as impact sources. Additionally, four tests were performed with a special input module installed in the data acquisition system that applied a basic analog single-pole, high-pass filter at 10,000 Hz. The filtered module was tried during initial testing to determine if the filter was helpful in eliminating unwanted low frequency noise from the data. Once the arrival time of every available sensor is picked for each event, the source location algorithm is employed. The algorithm is a reverse procedure of the source location triangulation equation. Steps in locating the source are:

1. An acceptable mesh grid to the area of interest is applied. For the trial hammer testing a 2-D planar grid 1 in x 1 in was employed.

2. It was assumed that each location was a potential correct source location. At each grid location, the distance to each sensor location was calculated.

3. The time that the source theoretically occurred (t0) was calculated from the selected arrival time from each sensor and the calculated distance. A constant concrete velocity was assumed. For example, if three sensors are used, three different values of t0 will be obtained (t0 calculated from sensor 1 or t01, t0 calculated from sensor 2 or t02, and t0 calculated from sensor 3 or t03).

4. If the calculated location happens to be the actual location of the source, t01, t02 and t03 should all be identical and equal to the actual time that the event occurred (t0). Typically, they are not in agreement. The difference (error) between the t0 values from each of the sensors is calculated as well as the sum

of the squares of the error and then normalized based upon the number of sensors used in the calculation.

5. The error calculation was repeated for each grid location and the location with minimum error was deemed as the source location.

The day prior to the scheduled saw-cutting, trial testing was performed using the accelerometer array and a hammer impact source on the bridge deck at a variety of locations. This system testing provided useful data with little to no background noise (unlike testing during the saw-cutting which causes significant vibration levels). Figure 4-22 shows a photograph of trail testing using a metal ball peen 2-lb hammer close to one of the magnetically mounted accelerometers.

Figure 4-22: Trial source location testing using a metal ball peen hammer.

Trial testing was performed by striking the concrete bridge deck with either a metal ball peen or hard-plastic black-tipped impulse hammer that measures force. Twenty-five separate trial tests were performed using hammer impacts as the source location. The filtered module was tried during initial testing to determine if the filter was helpful in eliminating unwanted low frequency noise from the data. Table 4-2 presents the results from the trial testing.

Table 4-2: Trial testing impact source locations

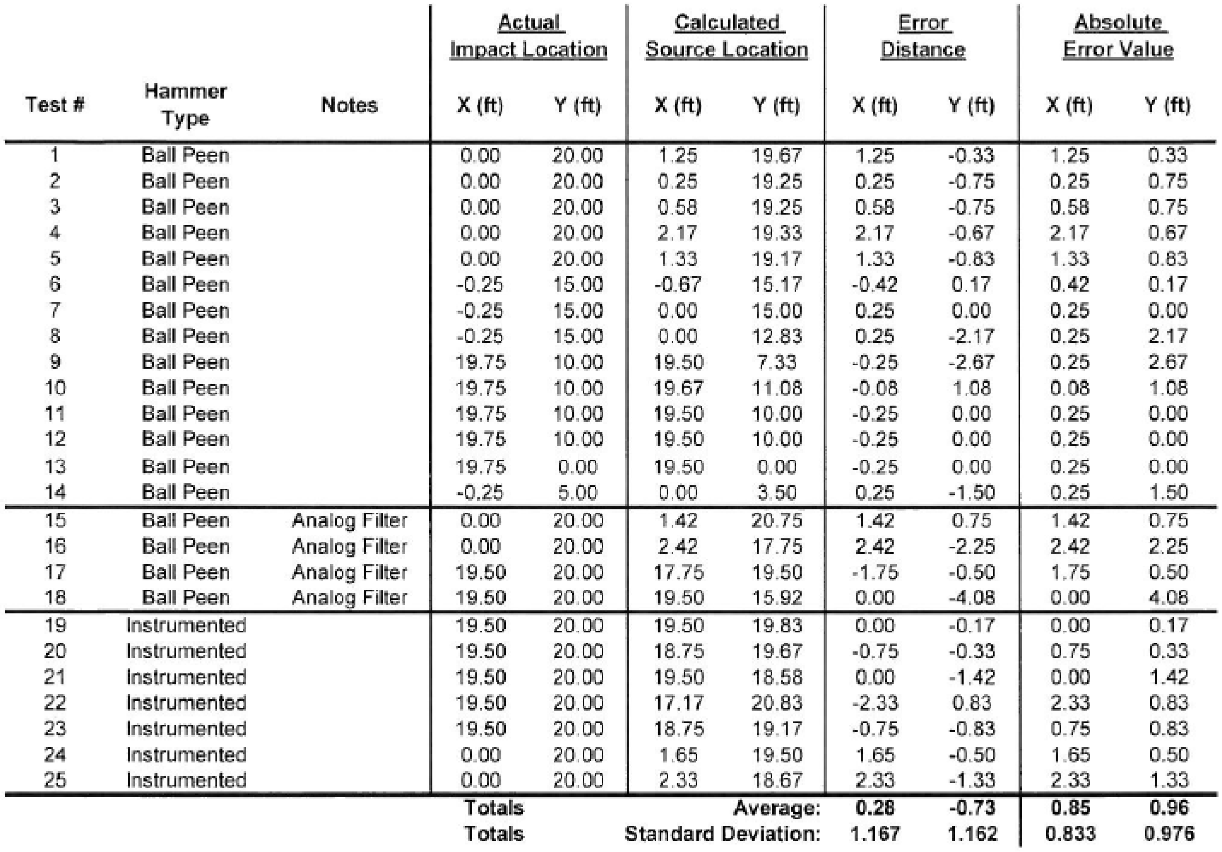

			Actual Impact Location		Calculated Source Location		Error Distance		Absolute Error Value	
Test #	Hammer Type	Notes	X (ft)	Y (ft)	X (ft)	Y (ft)	X (ft)	Y (ft)	X (ft)	Y (ft)
1	Ball Peen		0.00	20.00	1.25	19.67	1.25	-0.33	1.25	0.33
2	Ball Peen		0.00	20.00	0.25	19.25	0.25	-0.75	0.25	0.75
3	Ball Peen		0.00	20.00	0.58	19.25	0.58	-0.75	0.58	0.75
4	Ball Peen		0.00	20.00	2.17	19.33	2.17	-0.67	2.17	0.67
5	Ball Peen		0.00	20.00	1.33	19.17	1.33	-0.83	1.33	0.83
6	Ball Peen		-0.25	15.00	-0.67	15.17	-0.42	0.17	0.42	0.17
7	Ball Peen		-0.25	15.00	0.00	15.00	0.25	0.00	0.25	0.00
8	Ball Peen		-0.25	15.00	0.00	12.83	0.25	-2.17	0.25	2.17
9	Ball Peen		19.75	10.00	19.50	7.33	-0.25	-2.67	0.25	2.67
10	Ball Peen		19.75	10.00	19.67	11.08	-0.08	1.08	0.08	1.08
11	Ball Peen		19.75	10.00	19.50	10.00	-0.25	0.00	0.25	0.00
12	Ball Peen		19.75	10.00	19.50	10.00	-0.25	0.00	0.25	0.00
13	Ball Peen		19.75	0.00	19.50	0.00	-0.25	0.00	0.25	0.00
14	Ball Peen		-0.25	5.00	0.00	3.50	0.25	-1.50	0.25	1.50
15	Ball Peen	Analog Filter	0.00	20.00	1.42	20.75	1.42	0.75	1.42	0.75
16	Ball Peen	Analog Filter	0.00	20.00	2.42	17.75	2.42	-2.25	2.42	2.25
17	Ball Peen	Analog Filter	19.50	20.00	17.75	19.50	-1.75	-0.50	1.75	0.50
18	Ball Peen	Analog Filter	19.50	20.00	19.50	15.92	0.00	-4.08	0.00	4.08
19	Instrumented		19.50	20.00	19.50	19.83	0.00	-0.17	0.00	0.17
20	Instrumented		19.50	20.00	18.75	19.67	-0.75	-0.33	0.75	0.33
21	Instrumented		19.50	20.00	19.50	18.58	0.00	-1.42	0.00	1.42
22	Instrumented		19.50	20.00	17.17	20.83	-2.33	0.83	2.33	0.83
23	Instrumented		19.50	20.00	18.75	19.17	-0.75	-0.83	0.75	0.83
24	Instrumented		0.00	20.00	1.65	19.50	1.65	-0.50	1.65	0.50
25	Instrumented		0.00	20.00	2.33	18.67	2.33	-1.33	2.33	1.33
			Totals			**Average:**	**0.28**	**-0.73**	**0.85**	**0.96**
			Totals			**Standard Deviation:**	**1.167**	**1.162**	**0.833**	**0.976**

4.3.2 AE Test Results

The saw-cutting was monitored using the accelerometer layout, to determine if the sensor layout could be used to identify the location of PT tendon breakages in the box-section web walls.

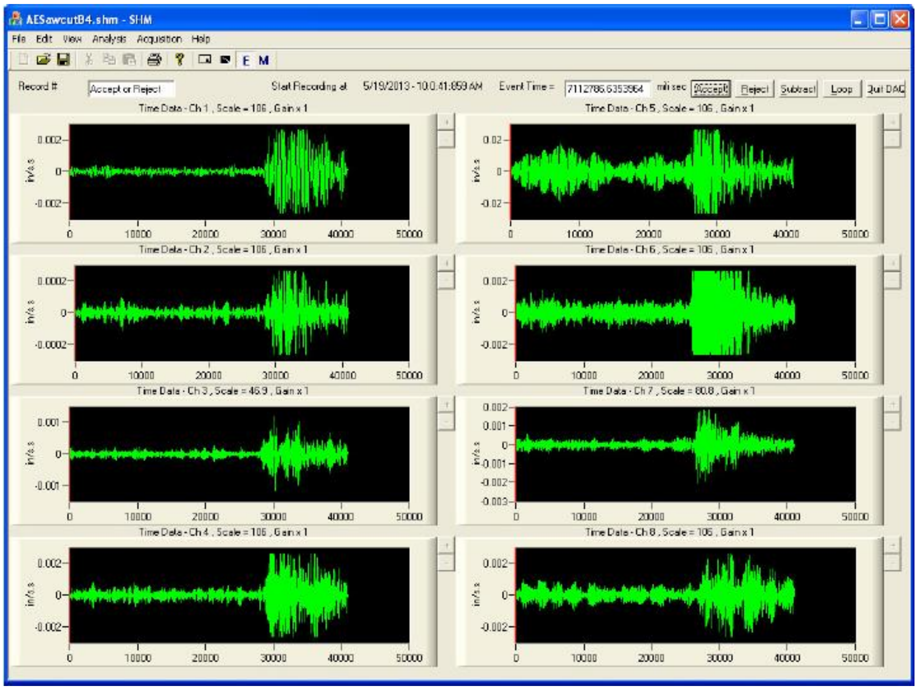

Record # Accept or Reject

Start Recording at 5/19/2013 - 10:0:41:859 AM

Event Time = 7112786.6353964 mili sec

Figure 4-23: Example data during saw cutting for all 8 accelerometers.

Figure 4-23 shows an example PT tendon breakage event during the saw-cutting. As observed in Figure 4-23, the accelerometer data acquired during saw-cutting had significant vibration noise prior to and during the tendon breakage event. The noise is induced into the structure by the wire-saw and possibly smaller vibrations from other equipment on the bridge deck. While the PT tendon breakage events are easily apparent on a macro scale of the data records, the vibration noise in the data makes it extremely difficult to separate P-wave and S-wave arrivals and accurately identify the arrival time. Small errors in arrival time (100's of microseconds) can have a large effect on the accuracy of the triangulation routine.

The second major challenge in analyzing the data acquired during saw-cutting was that the box girder is a 3-D structure with multiple tendons located throughout the web and within the top and bottom slabs of the box. However, the sensor array was only a 2-D array located on top of the bridge deck. While the 2-D sensor array worked reasonably well for hammer impact sources on top of the bridge deck where the accelerometers were also located, the saw-cutting events had the possibility of more complicated wave propagation around the box girder, depending upon where the cut tendon was located, and thus the 2-D array was less well suited for source location. To minimize this source of error, a simple 3-D model was also used during analysis, which considered the box girder top thickness as well as a geometrically simplified version of the east web wall. Similar to the 2-D model, a grid of voxels with dimensions of 1 in x 1 in x 1 in was utilized throughout the 3-D model. The source location algorithm was applied and the resulting error for each voxel was calculated and compared to locate the global minimum. Figure 4-24 shows a simplified schematic of the 3-D model. The coordinates are in inches and are referenced to the accelerometer positions.

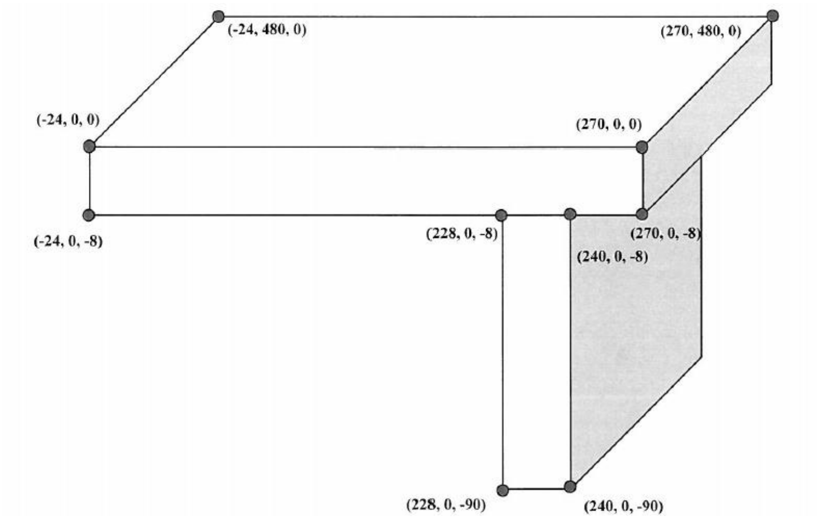

Figure 4-24: Simplified 3-D model schematic, coordinates in inches, referenced to accelerometer positions (not to scale).

Table 4-3: Sample testing results and corresponding acoustic emission.

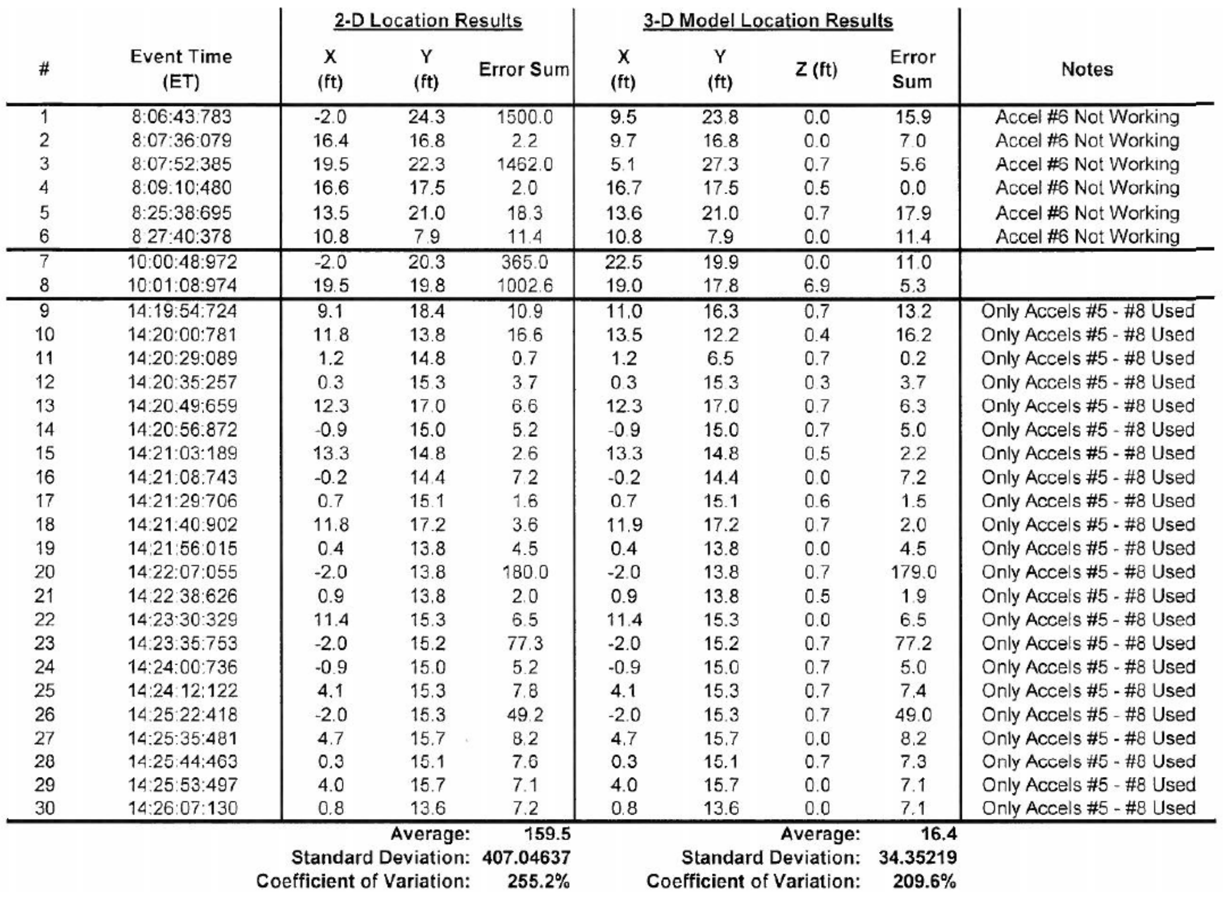

		2-D Location Results			3-D Model Location Results				
#	Event Time (ET)	X (ft)	Y (ft)	Error Sum	X (ft)	Y (ft)	Z (ft)	Error Sum	Notes
1	8:06:43:783	-2.0	24.3	1500.0	9.5	23.8	0.0	15.9	Accel #6 Not Working
2	8:07:36:079	16.4	16.8	2.2	9.7	16.8	0.0	7.0	Accel #6 Not Working
3	8:07:52:385	19.5	22.3	1462.0	5.1	27.3	0.7	5.6	Accel #6 Not Working
4	8:09:10:480	16.6	17.5	2.0	16.7	17.5	0.5	0.0	Accel #6 Not Working
5	8:25:38:695	13.5	21.0	18.3	13.6	21.0	0.7	17.9	Accel #6 Not Working
6	8:27:40:378	10.8	7.9	11.4	10.8	7.9	0.0	11.4	Accel #6 Not Working
7	10:00:48:972	-2.0	20.3	365.0	22.5	19.9	0.0	11.0	
8	10:01:08:974	19.5	19.8	1002.6	19.0	17.8	6.9	5.3	
9	14:19:54:724	9.1	18.4	10.9	11.0	16.3	0.7	13.2	Only Accels #5 - #8 Used
10	14:20:00:781	11.8	13.8	16.6	13.5	12.2	0.4	16.2	Only Accels #5 - #8 Used
11	14:20:29:089	1.2	14.8	0.7	1.2	6.5	0.7	0.2	Only Accels #5 - #8 Used
12	14:20:35:257	0.3	15.3	3.7	0.3	15.3	0.3	3.7	Only Accels #5 - #8 Used
13	14:20:49:659	12.3	17.0	6.6	12.3	17.0	0.7	6.3	Only Accels #5 - #8 Used
14	14:20:56:872	-0.9	15.0	5.2	-0.9	15.0	0.7	5.0	Only Accels #5 - #8 Used
15	14:21:03:189	13.3	14.8	2.6	13.3	14.8	0.5	2.2	Only Accels #5 - #8 Used
16	14:21:08:743	-0.2	14.4	7.2	-0.2	14.4	0.0	7.2	Only Accels #5 - #8 Used
17	14:21:29:706	0.7	15.1	1.6	0.7	15.1	0.6	1.5	Only Accels #5 - #8 Used
18	14:21:40:902	11.8	17.2	3.6	11.9	17.2	0.7	2.0	Only Accels #5 - #8 Used
19	14:21:56:015	0.4	13.8	4.5	0.4	13.8	0.0	4.5	Only Accels #5 - #8 Used
20	14:22:07:055	-2.0	13.8	180.0	-2.0	13.8	0.7	179.0	Only Accels #5 - #8 Used
21	14:22:38:626	0.9	13.8	2.0	0.9	13.8	0.5	1.9	Only Accels #5 - #8 Used
22	14:23:30:329	11.4	15.3	6.5	11.4	15.3	0.0	6.5	Only Accels #5 - #8 Used
23	14:23:35:753	-2.0	15.2	77.3	-2.0	15.2	0.7	77.2	Only Accels #5 - #8 Used
24	14:24:00:736	-0.9	15.0	5.2	-0.9	15.0	0.7	5.0	Only Accels #5 - #8 Used
25	14:24:12:122	4.1	15.3	7.8	4.1	15.3	0.7	7.4	Only Accels #5 - #8 Used
26	14:25:22:418	-2.0	15.3	49.2	-2.0	15.3	0.7	49.0	Only Accels #5 - #8 Used
27	14:25:35:481	4.7	15.7	8.2	4.7	15.7	0.0	8.2	Only Accels #5 - #8 Used
28	14:25:44:463	0.3	15.1	7.6	0.3	15.1	0.7	7.3	Only Accels #5 - #8 Used
29	14:25:53:497	4.0	15.7	7.1	4.0	15.7	0.0	7.1	Only Accels #5 - #8 Used
30	14:26:07:130	0.8	13.6	7.2	0.8	13.6	0.0	7.1	Only Accels #5 - #8 Used
			Average:	159.5			Average:	16.4	
			Standard Deviation:	407.04637			Standard Deviation:	34.35219	
			Coefficient of Variation:	255.2%			Coefficient of Variation:	209.6%	

During the saw cutting the wire-saw was wrapped around a portion of the top slab, the entire east web wall, and a portion of the bottom slab of the box girder. Because such a large portion of the structure was wrapped by the saw, the exact location of any tendon-breakage was largely unknown. The wire-saw primarily progressed upward through the bottom to the top of the box girder. The wire-saw primarily progressed from the outside edge (east) of the remaining deck wing toward the box girder web. Table 4-3 presents a sample of the data acquired during monitoring around three separate times when several tendon breakage events occurred. Figure 4-25 presents the predicted locations of the events noted in Table 4-3 from the 2-D and 3-D models, respectively.

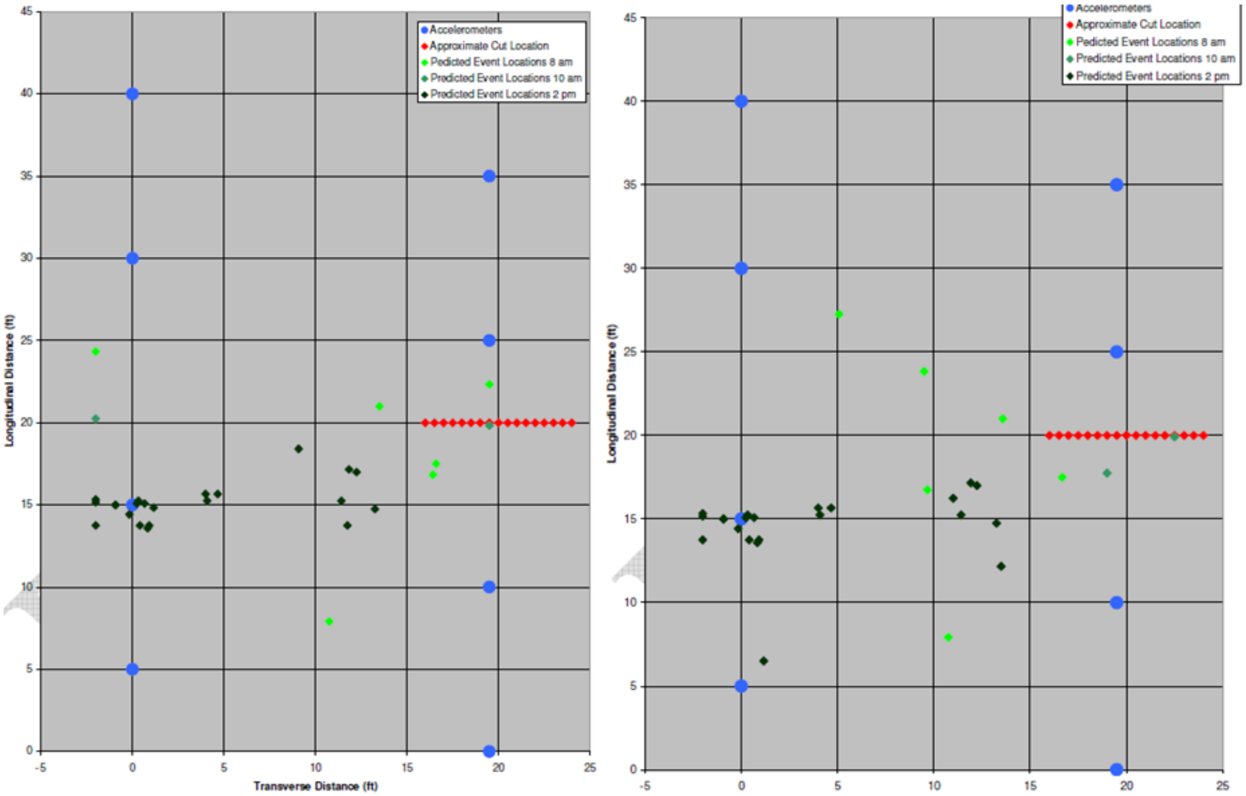

Figure 4-25: Predicted AE tendon saw-cut break event locations, plan view, using 2-D (left) and 3-D (right) model.

4.3.3 AE Test Summary

AE monitoring was effective in pinpointing the location of calibration hammer strikes the day before bridge deconstruction when there was no activity on the bridge. As observed in Table 4-2, Table 4-3, and Figure 4-25, the source location routine using both the 2-D and 3-D model provided seemingly poor to fair results when compared with the expected approximate source locations (assuming all tendon breaks occurred at the mid-span saw-cut). The two factors, high level of noise created by the saw-cutting which made determining the exact wave arrival time problematic and the 3-D nature of the structure are likely the biggest contributors to the poor results. The data has shown that the amplitude of vibration due to such tendon breakages is substantial and can be easily measured at distances of 20 ft or more. The events produce vibration amplitudes above high levels of noise; therefore, it is likely that the events would be apparent above typical traffic noise (without the high-amplitude noise of saw-cutting).

Additionally, in hindsight, the sensor array layout could have been more optimized for the saw-cutting layout. It was initially understood that the wire-saw would wrap the entire cross-section (which was not able to be done). Therefore, the sensors were mounted nearly directly above the web walls and across a wide area. It is ideal if the source event is within the sensor array, so focusing on a single web wall, the sensors could have been mounted near the edge of the box girder wing and near the center of the box girder to produce a dense grid which would better perform at confining the events. Also, given the 3-D nature of the structure as well as the wire-saw path, it would have been advantageous to have additional sensors on the web wall and/or on the bottom of the box girder. In general, the denser the sensor array the more accurate the results.

It is possible that additional signal processing techniques, such as filtering, may improve the analysis results. It is also possible that a more complex 3-D model of the cross-section (that considers the full box including tapers and chamfer) may improve the analysis results. Additionally, the triangulation routine for AE event locations employed here-in searched for global minimum of error, therefore it is possible that local minimum exists at more plausible event locations and that a more stringent algorithm could improve results.

4.4 INTERFEROMETRIC PHASE RADAR (IPR) MONITORING

4.4.1 IPR Test Methodology

The IBIS-S Interferometric phase radar was supplied, installed and operated by Olson Engineering, Inc. The imaging by interferometric survey – structural system (IBIS-S) was set-up near abutment 1 of the bridge and reflectors were installed on center span. The IPR system relies on line of sight reflections of the reflected radar signals; therefore, the system was set up on the west side (inside curve) of the bridge deck to provide a clear, unobstructed view of all 11 installed corner reflectors. The IBIS-S system simultaneously measures the displacement of all reflectors within the system's line of sight. The system monitors both static displacements with a resolution of 0.0004 in and dynamic movements up to 100 Hz. Figure 3-29 presents a photograph from behind the IBIS-S antenna showing the orientation of the system and view of the corner reflectors.

The IBIS-S system is less sensitive to vibration pulses such as those caused by tendon breaks than the accelerometers due to several factors, including sample rate (vibrations may be higher than 100 Hz) and the fact that the IBIS-S system is monitoring overall structure movements and not high speed transient waves traveling through the structure.

Figure 4-26: IBIS-S antenna shows system orientation and corner reflectors.

4.4.2 IPR Test Results

The IBIS-S system was used to monitor the structure while the saw-cuts were performed. Prior to testing it was unknown if the tendon saw-cutting would produce vibration emissions that could be measured by the IBIS-S system, which has a relatively low sampling rate (max sampling rate of 200 Hz for a nyquist frequency of 100 Hz). However, the IBIS-S data does show that small vibration pulses (likely due to tendon cutting) were apparent above the background vibration levels due to the saw-cutting. These vibration pulses typically appear in multiple reflector location's data and are approximately synchronized in time. The vibration pulses have duration of approximately 0.1 s and vary in amplitude. Figure 4-27 and Figure 4-28 present plots of time history vibration data for reflectors #3, #7 and #10, shows an example of a suspected tendon break vibration pulse. The vibration data shown was from the second day of saw-cutting, in which the web closest to the corner reflectors was being cut.

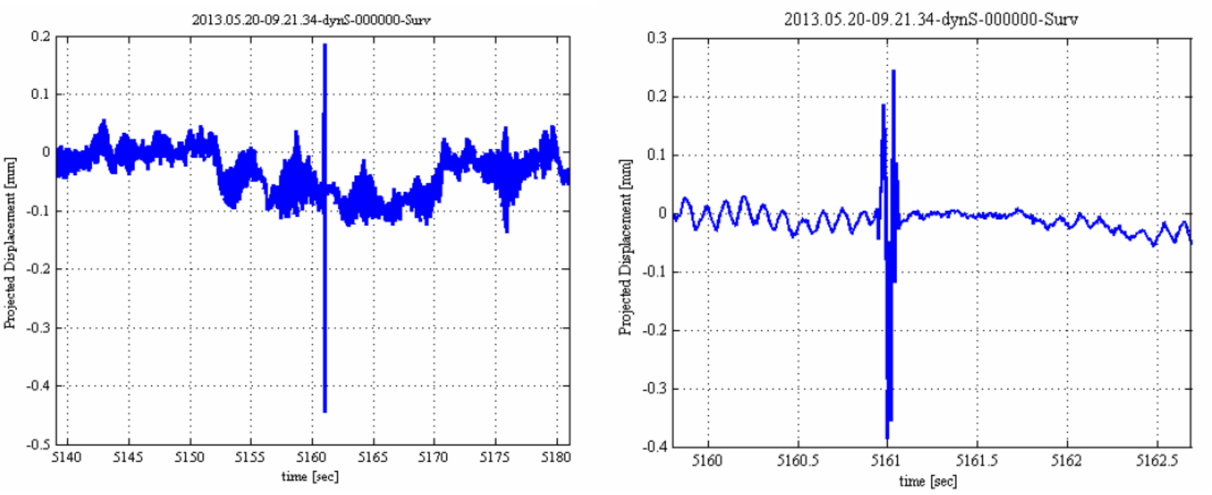

Figure 4-27: Vertical displacement of reflector #3 during suspected saw-cut tendon break.

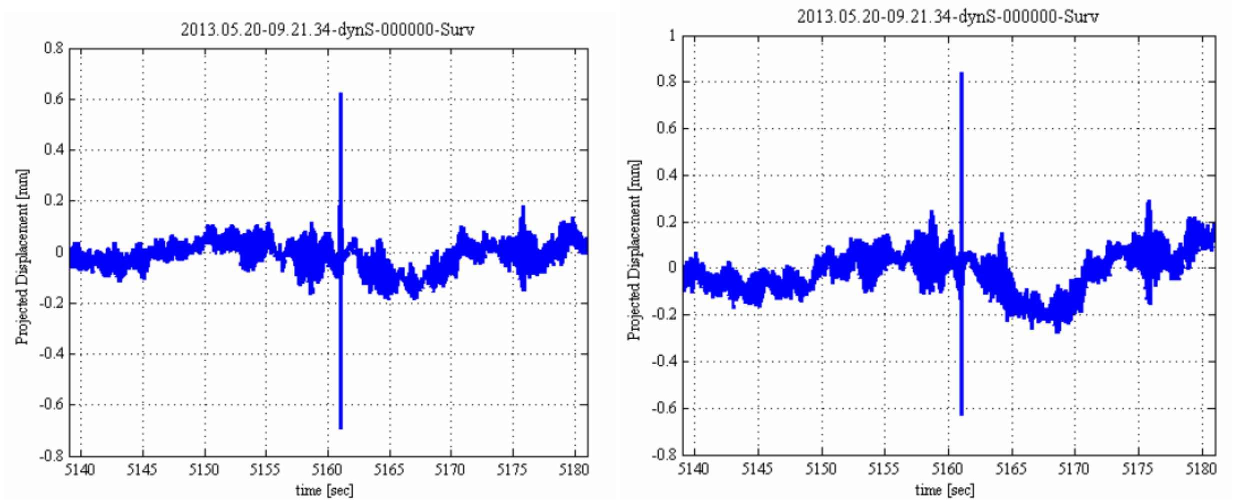

Figure 4-28: Vertical displacement of reflector #7 (left) and #10 (right) during suspected tendon break.

4.4.3 IPR Test Summary

While the IBIS-S system can detect impulse vibrations due to the tendon cutting, the system's sampling rate is not fast enough to provide the resolution in the time domain to differentiate the arrival times accurately enough to be used to determine the location of the vibration source. Consequently, it is interesting to note the signature of the tendon breaks in the IBIS-S data, but it is considered of minimal practical use. The IBIS-S data can also be analyzed to measure the overall structure movements during the saw-cutting of the web walls. The "strong back" beam reinforcement and other reinforcing measures reduces the amplitude of displacement due to the cutting of the top and bottom slabs and web walls, but measurable movement was observed.

5 LABORATORY AND SEGMENT TESTING

5.1 INFRARED THERMOGRAPHY (IRT) TEST

5.1.1 Identification of Strand

Infrared thermography (IRT) is deployed by two approaches; passive and active heating. With the passive approach, differentiation in thermal heating and cooling of material is made in ambient conditions, while in case of active approach an external thermal source is used for thermal distinctions. For the identification of tendon anomalies due to corrosion, active heating source is required as passive heating may not be adequate to create sufficient differential heating of tendon elements. Inductive heating is of interest as an active heating source for testing in PT tendons because it can create differential heating of tendon element without need to contact any tendon components directly.

In this effort, at first, feasibility of using IRT was tested with the samples prepared with steel wire surrounded by a polyvinyl chloride (PVC) duct. To create differential heating conditions, the steel wire was pre-heated (i.e. oven, torch, inductive heating) to verify feasibility of heat radiation through an encapsulating plastic material. From the testing, it was evident that the heat signature of the steel placed within a plastic container can be detected (Figure 5-1). Furthermore, materials of other composition placed in contact with the heated steel can be detected as well. As shown in Figure 5-2, the spherical shape of a foam ball can be seen. The pre-heated steel wire inserted through the foam ball was placed within the plastic container. This observation was encouraging as material of varying composition and density (such as grout voids, grout segregation, and grout contamination) may be present in bonded PT tendons.

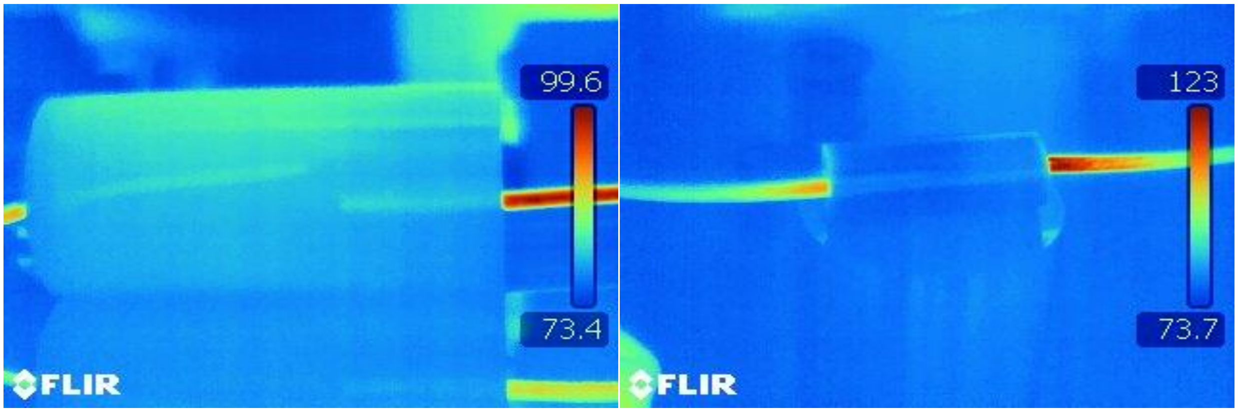

Figure 5-1: Test of samples without grout.

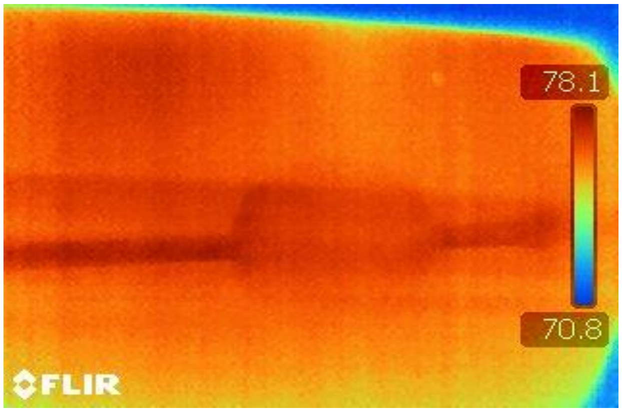

Figure 5-2: Test of samples having a foam ball.

It was evident that IRT of steel within free space would be significantly different than that encapsulated in a filler such as grout material. For further exploration of the use of IRT, steel was encapsulated in a grout material. The use of passive heating by the natural heat of hydration of the cast grout was initially considered. This heating source would be useful during early hydration time; therefore, only initial tendon defects can be considered for quality assurance purposes and use at a later testing stage may not be possible. Although obscure, Figure 5-3, indicates that the steel strand can be distinguished.

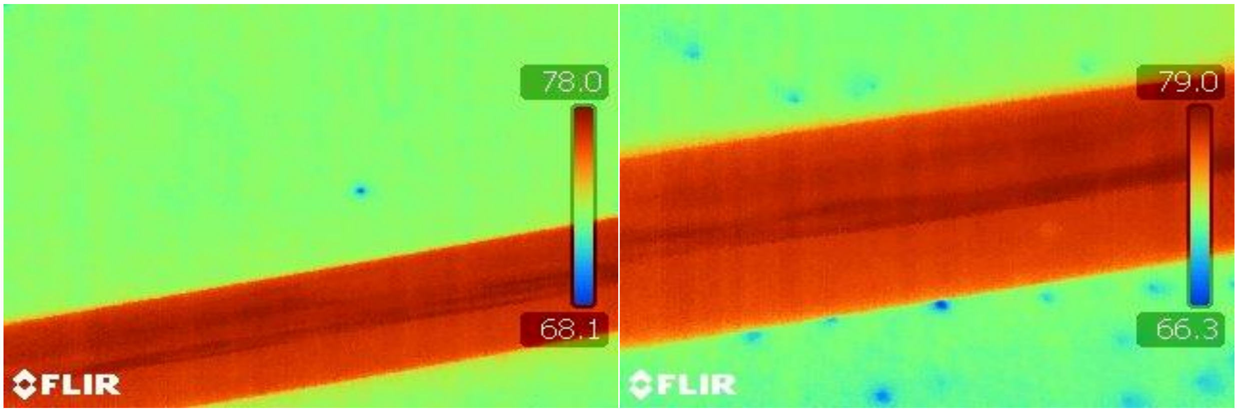

Figure 5-3: Test figures using the heat of hydration.

Testing of steel embedded in grout required other sources of heating. A steel wire was embedded in grout within a cylindrical mold. The steel wire extended out of the grout at one end and a butane torch was used to heat only the tip of the exposed steel wire. The diffusion of the heat transferred from the tip of the steel wire into the grout was readily observed (Figure 5-4) and it was shown that the infrared camera was highly sensitive to heat transfer in the grout. Interestingly, no differential heating along the length of the embedded steel wire was observed but it was evident that the heat capacity of the grout can be investigated by this method.

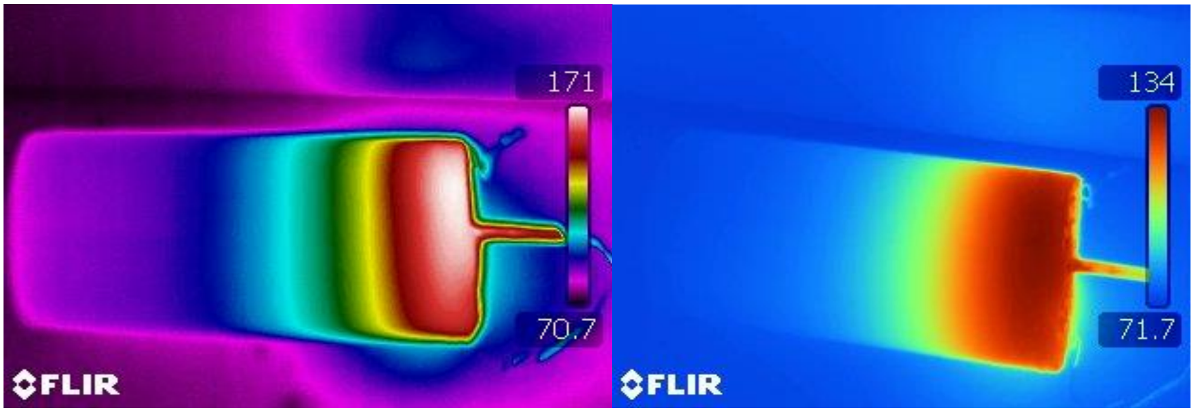

Figure 5-4: Test figures using butane torch.

For testing of external tendons, direct heating can cause premature damage to the tendons components and these effects were not considered in the tests. Both direct and resistive heating would require partial exposure of the tendons components.

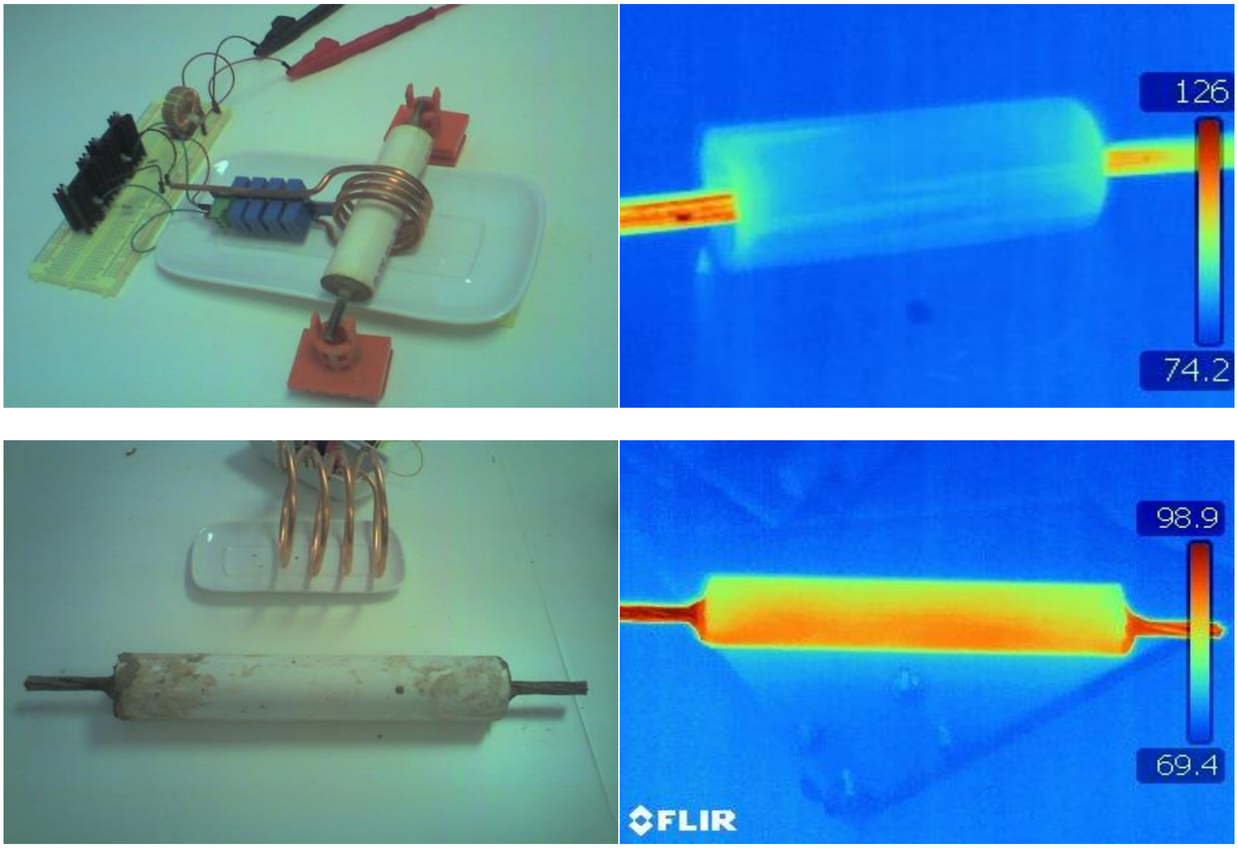

Figure 5-5: Test of samples surrounded by grout.

Inductive heating was thought to be of interest due to its ability to heat the steel without direct contact. The steel was heated by inductive heating and only the steel was to be heated initially. Testing showed that heat signature of the steel can be obscured (Figure 5-5). Also, thermal reflections on the outer surface of the plastic duct may result in further anomalous findings. However, encouraging results were obtained when a discontinuity was placed in the steel sample (i.e. wire cut in half). As shown in Figure 5-6, the location of the steel discontinuity was clearly demarcated. It was thought that the thermal signature was due to heating of the grout material surrounding the steel wire. The grout material was differentially heated at the location where steel was not present.

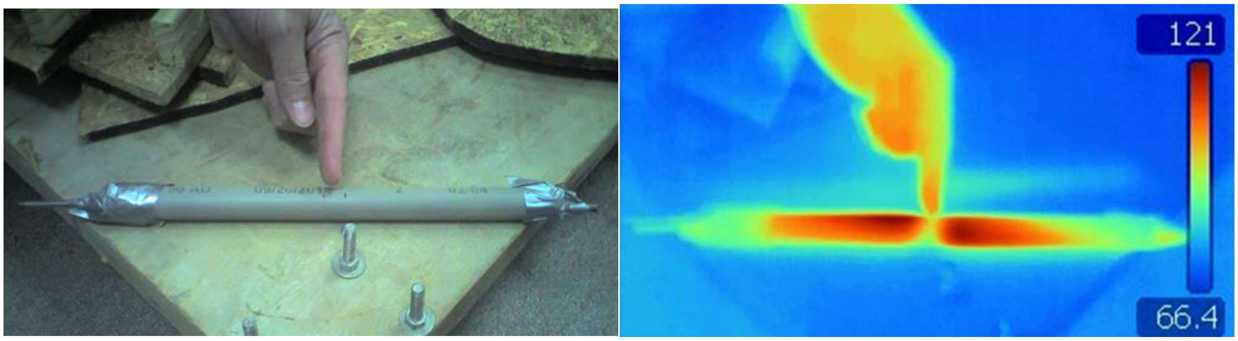

Figure 5-6: Test of samples having a discontinuity in steel.

In that same sample, two batches of grout were used to simulate differentiation in grout. As seen in Figure 5-7, the differential heating of the grout showed clear demarcation of the two grout mixes. The grout with a higher water-to-cement ratio (w/c) heated more than the material at the ends containing lower w/c ration grout. The heating of the grout was shown to be different despite approximate uniform heating of the wire. Study of end effects were not considered at this level of testing. Additional information on IRT testing is given in Appendix A.

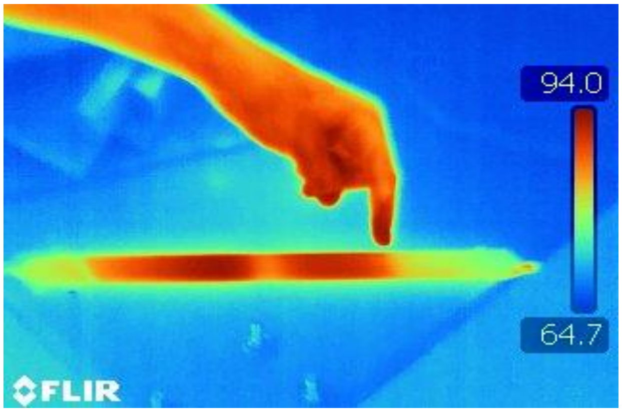

Figure 5-7: Test of samples having two types of grout condition.

5.1.2 Infrared Thermography (IRT) for Grout Deficiency

Several PT tendon failures were observed due to premature corrosion development in segmental concrete bridges during last few decades. The assessment of recently failed external PT tendons showed that the corrosion was attributed to the presence of anomalous grout. The reason behind the problem was soft grout which didn't set up, including grout segregation and associated voids. It was apparent that there was high water content in the segregated grout. So, it is important to identify soft-grout to prevent early corrosion, which may result in catastrophic failure. Non-destructive inspection of the tendons to locate grout material deficiencies and corrosion development has been a challenge without the wide availability and acceptance of appropriate techniques. Testing of IRT on preliminary test tendon samples showed promising results with indication to feasibility of identification of differential materials (Figure 5-8). In this part of the research the feasibility of using IRT was studied to identify deficient grout.

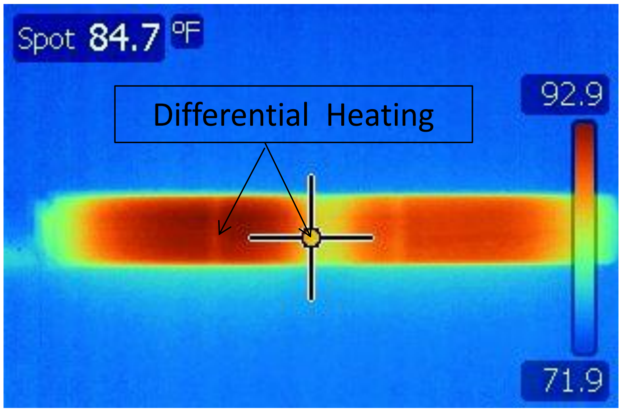

Figure 5-8: Differential heating of test tendon sample.

5.1.2.1 IRT Methodology for Grout Deficiency Tests

To incorporate different level of deficiency, samples were prepared using a commercial pre-packaged PT grout product along with variable sulfate and water content inconsistency. As-received and pre-exposed grout was used for sample preparation. For pre-exposure, grout was removed from its original package and was placed in container within a 100% relative humidity (RH) chamber for 32 days. In addition to possible absorbed moisture from pre-exposure, the grouts were mixed with additional 20% excess water (by mass of grout after exposure for treated samples) above the manufacturer recommended mix water content to enhance material deficiency. Three level of sulfate concentrations in the mix water termed as low (200 ppm), medium (20,000 ppm) and high (100,000 ppm) were mixed for the samples preparation for grout deficiency. The samples were divided in 8 different groups as represented in Table 5-1. The mixing procedures for small grout quantities followed manufacturer's recommendation. Small laboratory sample were casted in (2-in diameter x 3-in length) cylindrical mold and (2 × 2 × 1½ ø, 4¾ length) PVC tee as shown in Figure 5-9. The PVC tee was expected to facilitate volume displacement of the deficient grout material to the tee header and allow discrete testing and sampling of the deficient grout materials.

Figure 5-9: Casting of small laboratory sample.

Pre-exposed grout was made to evaluate the severity of grout degradation due to pre-exposure in high humidity and excess moisture content. Relevant grout material parameters included bulk density, void content, and moisture content were measured. The pre-exposed grouts (de-molded 4 days after casting) were placed in 100% RH for 40 days for conditioning in high humidity. After conditioning, the samples were subjected to drying to measure moisture content.

Table 5-1: Sample configuration with material differentiation

Sample group	Grout type	Water Content	Sulfate content
EAS	As-received	Required	No Sulfate
EALS	As-received	Required	Low Sulfate (200 ppm)
EAMS	As-received	Required	Medium Sulfate (2,000 ppm)
EAHS	As-received	Required	High Sulfate (10,000 ppm)
EES	32 days Exposed	20% Extra	No Sulfate
EELS	32 days Exposed	20% Extra	Low Sulfate (200 ppm)
EEMS	32 days Exposed	20% Extra	Medium Sulfate (2,000 ppm)
EEHS	32 days Exposed	20% Extra	High Sulfate (10,000 ppm)

5.1.2.2 IRT Grout Deficiency Test Results

IRT was used to detect any temperature variation within the test samples at different time after casting. Temperature differentiation was observed in samples after casting due to heat of hydration and their resulting chemistry. The following Figure 5-10 to Figure 5-12 shows the test sample and temperature variation within some of the samples after 4 and 18 hours of casting due to water cement reaction.

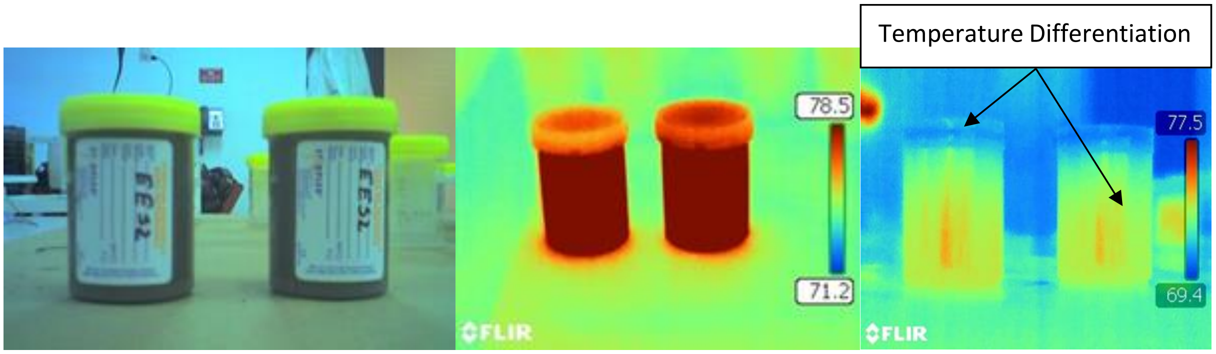

Figure 5-10: Laboratory sample (left) and temperature variation: at the time of casting (center); after 4 hours of casting (right).

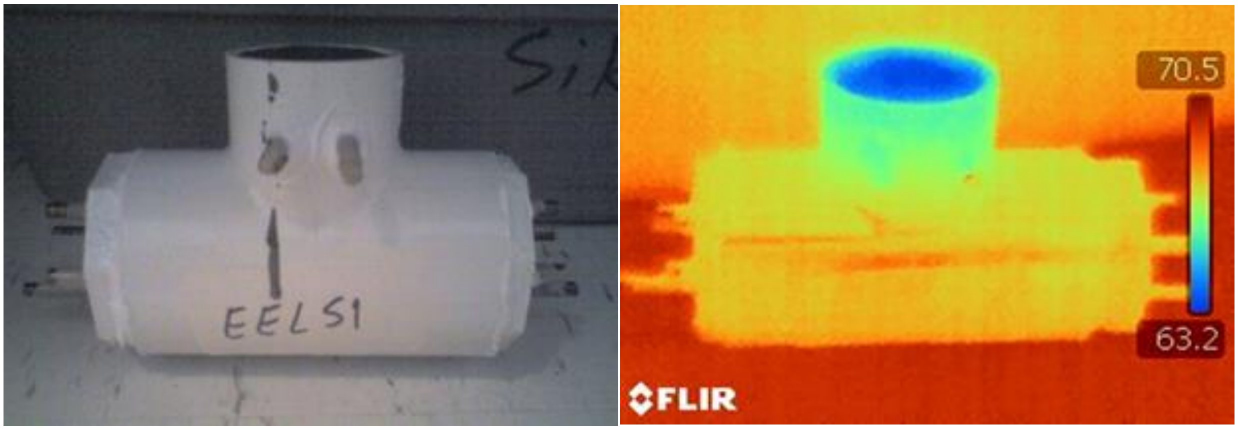

Figure 5-11: Samples for use in infrared testing at the time of casting.

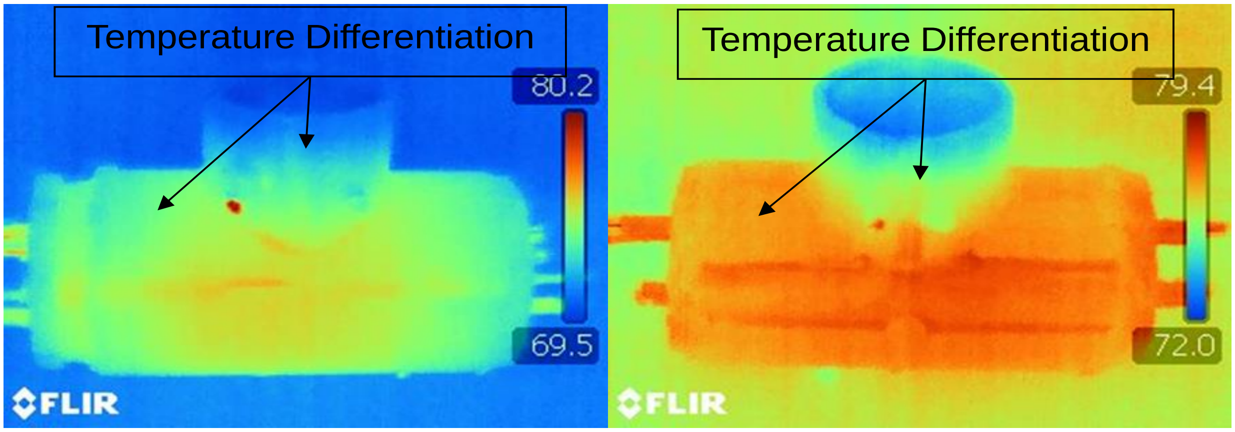

Figure 5-12: Infrared testing of samples: 4 hr after casting (left); 18 hr of casting (right).

From the figures, it is evident that infrared pictures could provide clear demarcation about the material differentiation as there was a temperature variation within the samples. From the thermographic picture, it was also visible that there was a temperature differentiation at the top of some samples. In the pre-exposed grout, exposure of the raw grout material to 100% RH for 32 days as well as application of excess mix water was thought to create grout material deficiencies. As shown in Figure

5-16, as-received grout with required water content formed uniform well-hardened strata but grout after exposure and casting with excess water formed two segments where the bottom portion was generally uniform and well hardened and the top portion consisted of a light and friable material (Figure 5-17). The top portion is referred to as being segregated. Grout material parameters such as bulk density, void content, and moisture content (that were thought to be possibly higher in deficient grout) were inspected from top and bottom portion of one set of the sample to evaluate the deficiency. Figure 5-13 to Figure 5-15 shows the moisture content, void content and bulk density of as-received (hardened) and pre-exposed (segregated) grout samples from top as well as bottom portion of the samples.

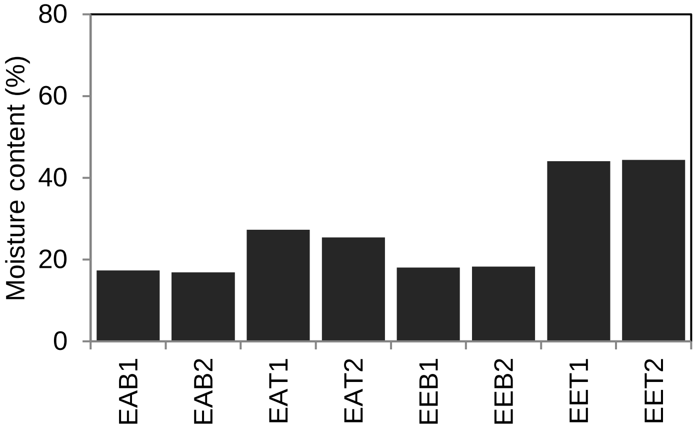

Figure 5-13: Moisture variation within the test sample.

E: Grout, A: As-received, E: Pre-exposure, T: Top, B: Bottom

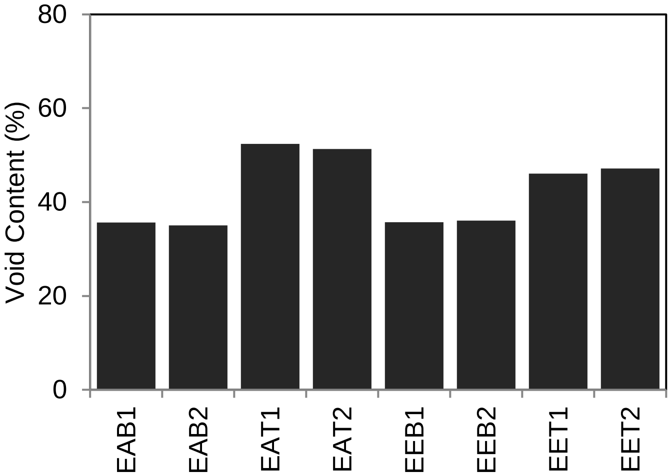

Figure 5-14: Void content within the test sample.

E: Grout, A: As-received, E: Pre-exposure, T: Top, B: Bottom

In agreement with visual observation of severe grout segregation, the pre-exposed grout samples with excess mix water had higher moisture and void content than hardened as-received samples. As expected, bulk density was higher at the bottom portion of the samples compared to the segregated top portion.

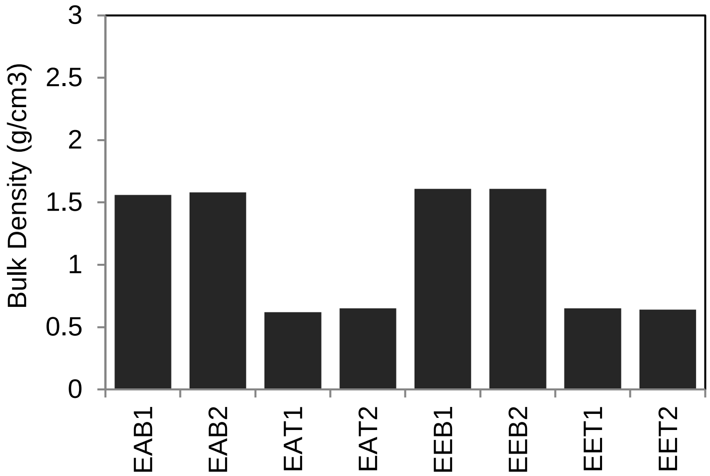

Figure 5-15: Density variation within the test sample.

E: Grout, A: As-received, E: Pre-exposure, T: Top, B: Bottom

As evident grout deficiency was identified by visual observation and with the help of infrared thermographic picture with passive heating by the heat of hydration. IRT was used to find out the feasibility of using active heating to locate grout deficiency. After 14 days of casting plastic molds from another set of sample were removed and clear visible separation was observed in the top portion of the samples fabricated from exposed grout mixed with extra water and low (200 ppm) amount of sulfate content. These samples contained deficient grout. Then all the samples were heated in the oven and thermal changes were observed in the top and bottom portion of the samples through an infrared camera. Clear thermographic demarcation and temperature variation were observed for the samples associated with deficient grout.

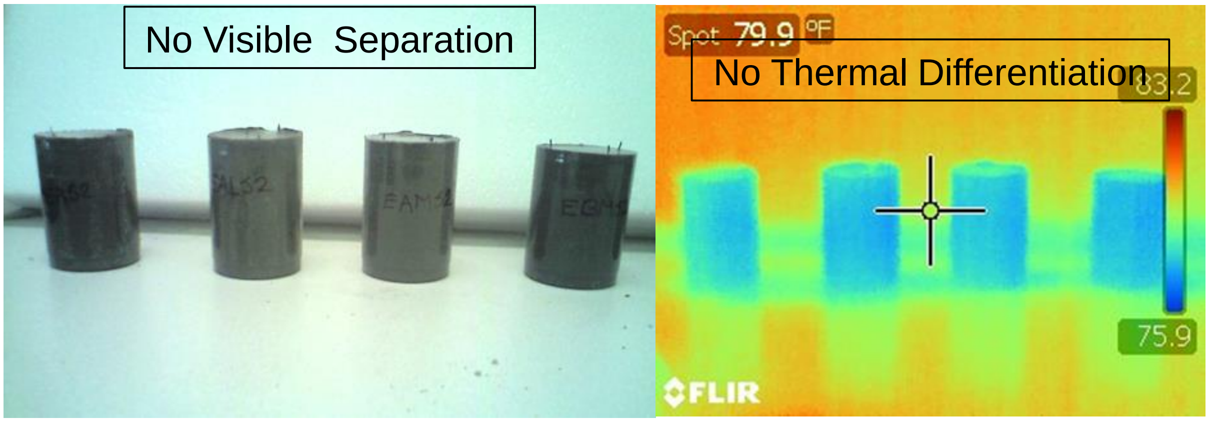

Figure 5-16: Samples prepared from as-received grout.

In consistence with visible identification, as-received samples did not show any thermal differentiation at top and bottom portion of the samples after heating in oven (Figure

5-16). Whereas clear visible and thermal differentiation was found within the samples consisting of pre-exposed grout (Figure 5-17 to Figure 5-21). Also, variable level of segregation was observed in the thermographic picture with different level of sulfate concentration (Figure 5-17).

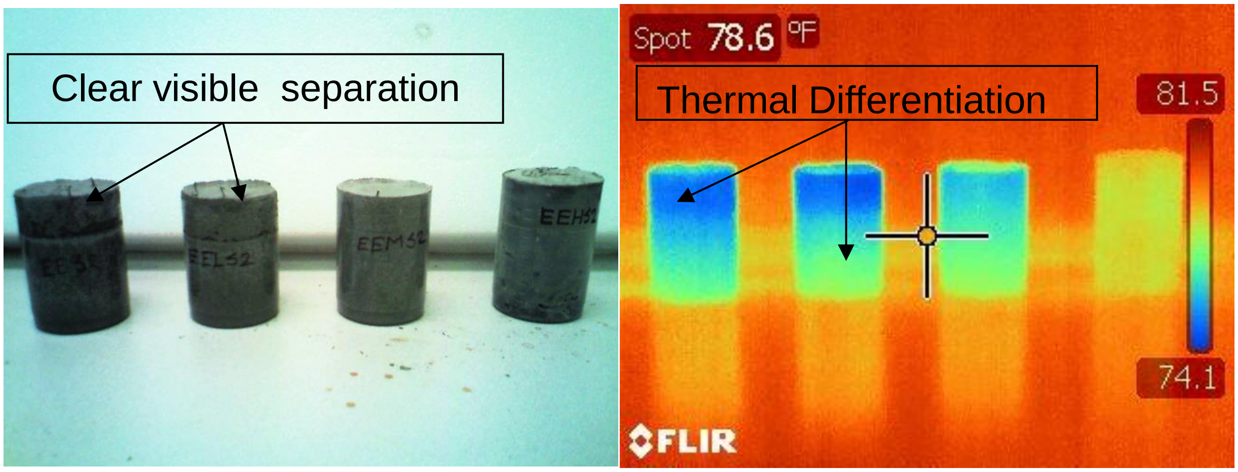

Figure 5-17: Samples prepared from pre-exposed grout.

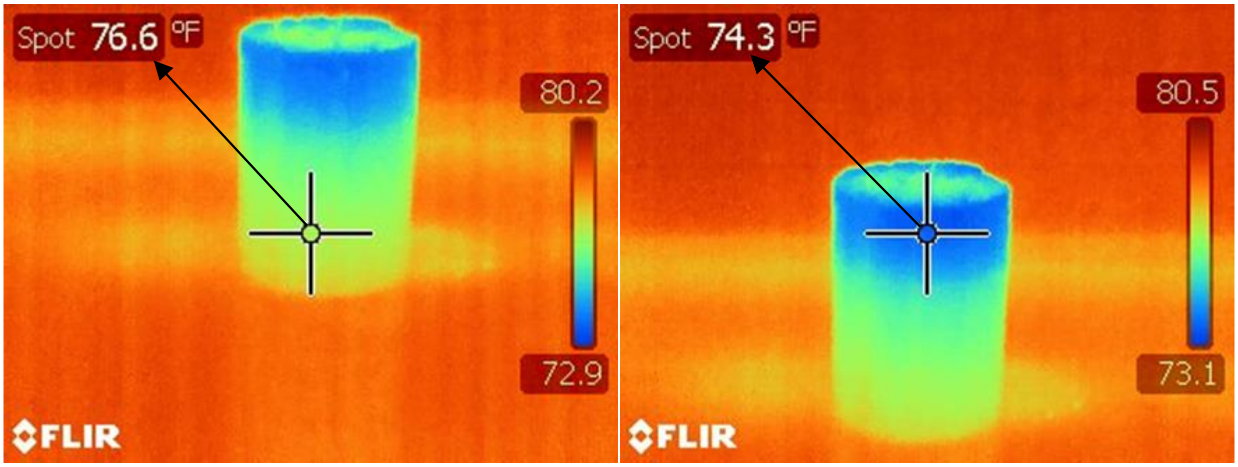

Figure 5-18: Temperature differentiation before heating (pre-exposed).

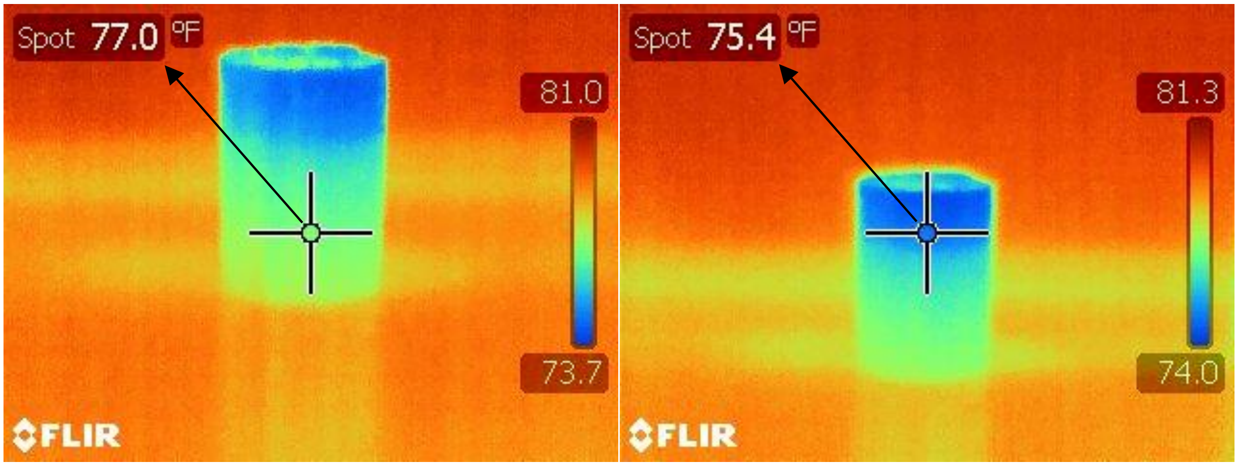

Figure 5-19: Temperature differentiation before heating (pre-exposed and low sulfate).

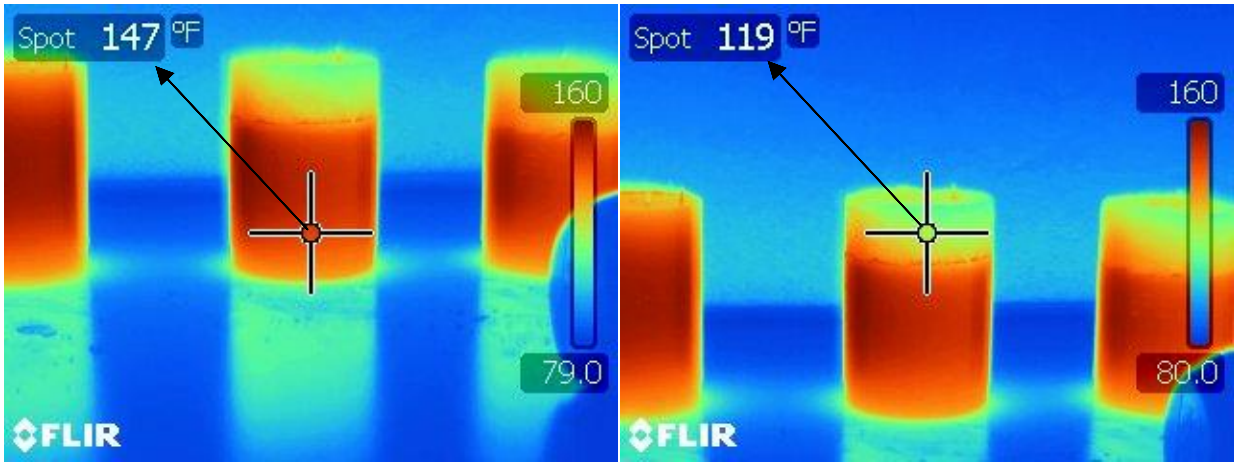

Figure 5-20: Temperature differentiation after heating (pre-exposed).

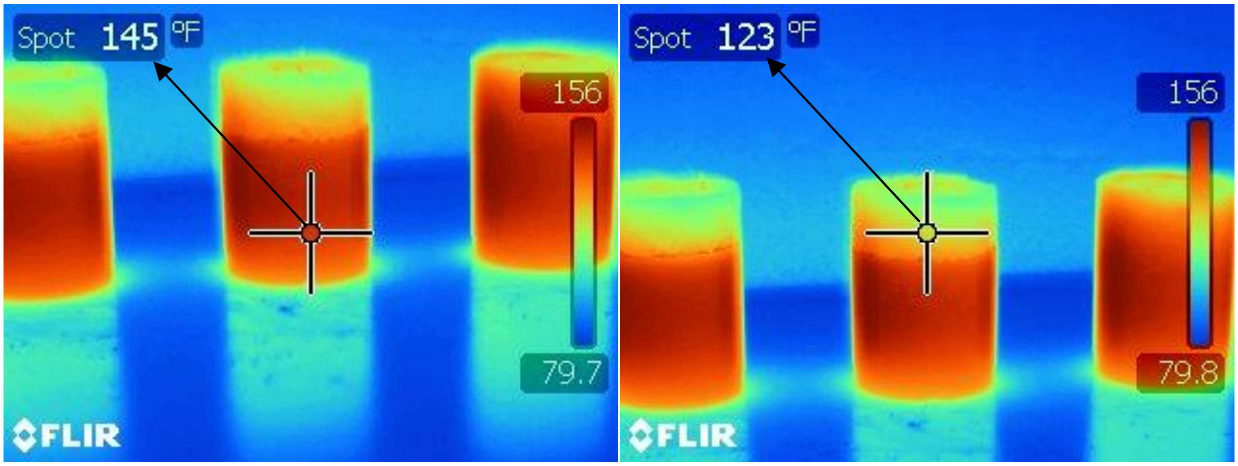

Figure 5-21: Temperature differentiation before heating (pre-exposed and low sulfate).

Heating and cooling temperature of bottom and top portion of all samples at regular interval was recorded by the infrared camera to verify the behavior of deficient grout.

Temperature differentiation was recorded after a regular time interval. From the recorded temperature it was observed that extra water content created deficient grout at the top of the sample which behaves differently through the heating and cooling process as shown in the following graphs (Figure 5-22 to Figure 5-26). Even though the cooling process depends on the convection as well as radiative heat transfer to its surrounding environment, there was a clear demarcation of temperature variation for the deficient grout.

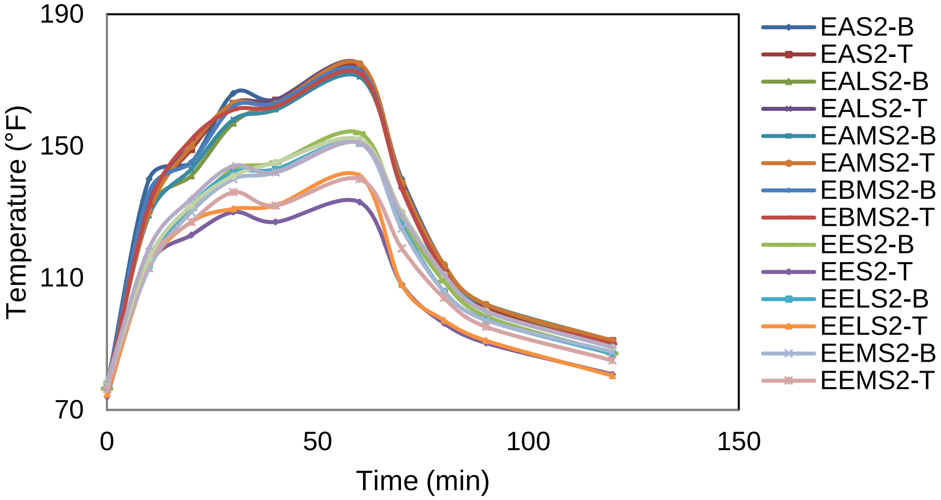

Figure 5-22: Temperature differentiation of different samples.

From the graph (Figure 5-22) the behavior of samples fabricated from as-received grout is different from pre-exposed grout mixed with extra water content. By analyzing the bottom and top portion temperature, it was observed that top portion temperature for the exposed grout sample revealed lower temperature. This was an indication of differential thermal behavior of deficient grout.

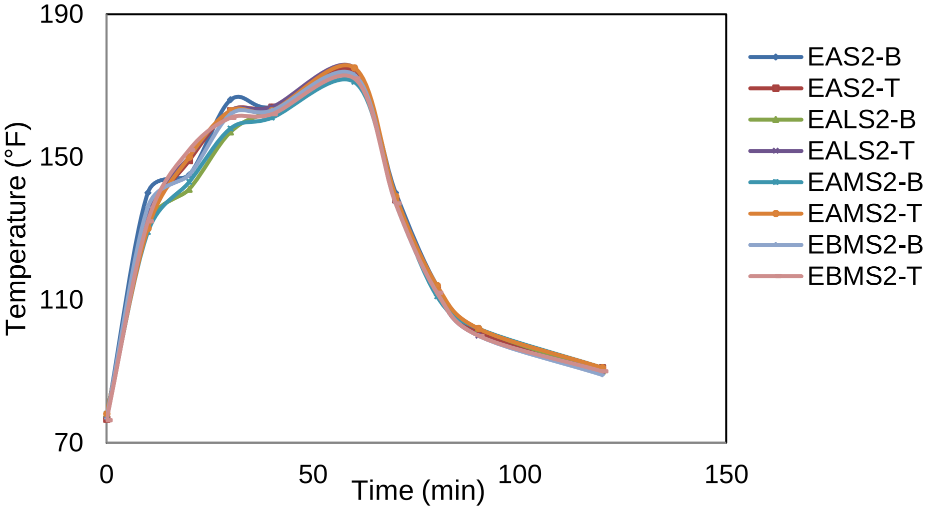

Figure 5-23: Temperature differentiation of samples (as-received grout).

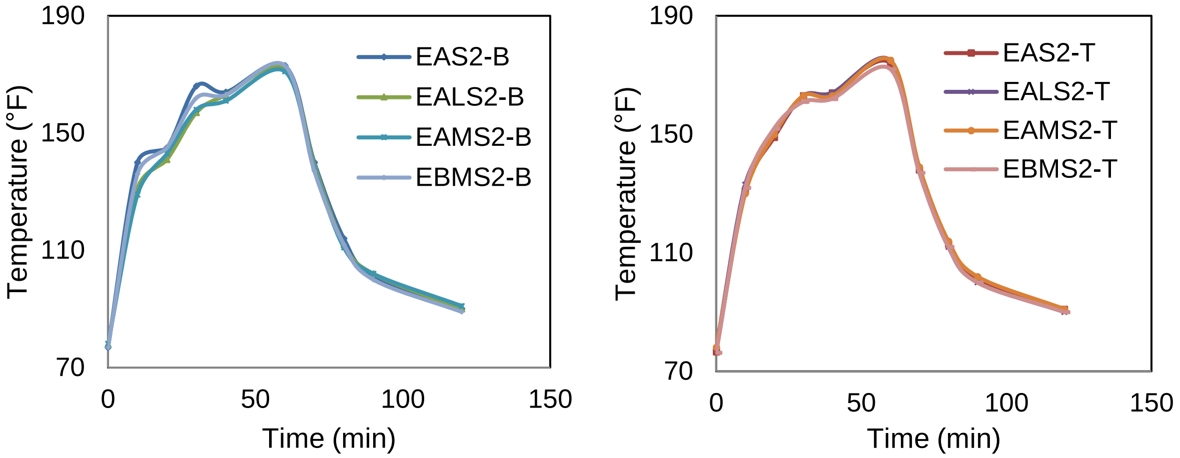

Figure 5-24: No apparent temp differentiation at bottom (left) and no apparent temp differentiation at top (right).

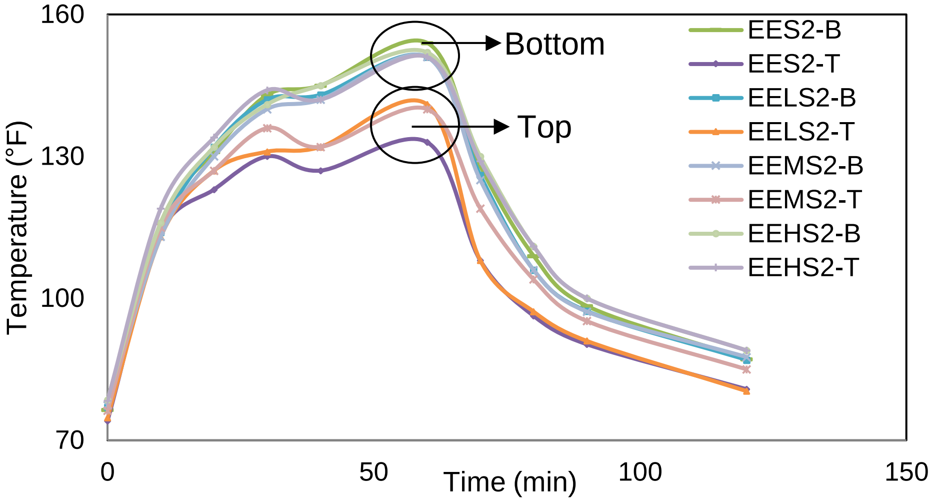

Figure 5-25: Temperature differentiation of samples (pre-exposed grout).

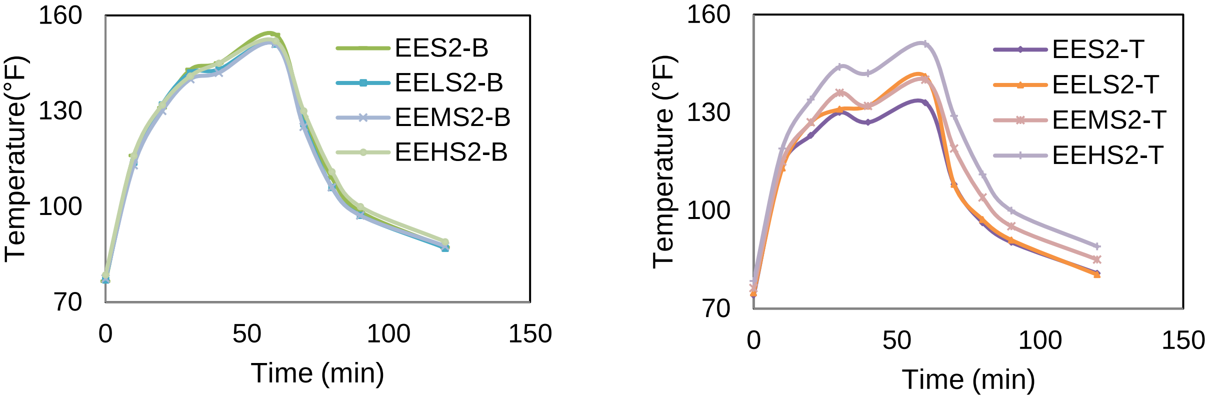

Figure 5-26: No apparent temperature differentiation at bottom (left) no apparent temp differentiation (right).

From infrared thermographs, deficient grout can be identified from good quality grout as temperature variation was observed on that region along with the heating and cooling transition. The principle problem involved in the detection of grout anomalies in PT tendons by active IRT is the system of heating. If the associated heating problem for active heating source is solved, IRT will be available as an efficient and easy NDT technology to locate deficient grout material.

5.1.3 Summary of IRT Test

Testing of IRT on grout encapsulated steel wire showed promising results. Detection of the heating of the steel and the subsequent heating of the surrounding grout in certain conditions can have differentiation with good demarcation of condition anomalies within the steel tendon. This finding further supports the benefit of inductive heating where the steel components are heated differentially from the surrounding grout. Early testing with inductive heating showed that wire breaks and differential grout materials can be detected. This is promising as deficient grout materials and steel corrosion are important parameters in the long-term durability of tendons. Further testing to resolve important testing parameters, such as the amount of heat required to provide good resolution of the thermal behavior of the material and heat capacity of relevant building materials that may or may not inhibit heat transport, is needed. Also, minimization of thermal reflections is important to reduce anomalous thermal signatures on the tendon surface. Further work, to develop an inductive heater that can be adapted to the geometries and scale of tendons and provide adequate heating, is needed. In the inductive heating experiments, the tendon was heated until observations of differential heating was made via the infrared camera. It is understood that the heating parameters will depend on the materials, amount of steel and other geometry details of the tendon components including grout quality, cover as well as the duct sheathing. Additional details of IRT tests and inductive heating are presented in Appendix A.

The presence of high moisture content can promote grout deficiency. The results of this preliminary work indicate that thermal differentiation in deficient grout by means of IRT is feasible due to the difference between the thermal diffusivities of areas containing distinct moisture content. The advantages of the technique are the ability to rapidly investigate large region with thermal variation and able to provide indication for further quantitative assessment. The limitation is that the promising thermographic imaging success depends strongly on the thermal variation of differential material content. This may require external heating source to create enough thermal differentiation to be detected by thermographic image through the HDPE duct layer. To obtain a clear detection, the thermal stimulation must be as uniform as possible. Inductive heating can be an opportunity and needs to be further developed. Nonetheless, IRT can be considered as a promising NDT approach for the monitoring and location detection of grout deficiency of external PT tendons.

5.2 MAGNETIC FLUX LEAKAGE (MFL)

5.2.1 MFL Test Principle

The principle of MFL method is to detect the distorted magnetic field created due to the low permeability of the defect and the resulting leakage field is detected by optimally positioned hall effect (HE) sensors. The instrumentation of the MFL device used in this report is designed to operate primarily on horizontal surfaces in laboratory and field testing of strands. The system consists of a permanent magnet, HE sensors and a carriage for calibrated movement as shown in Figure 5-27. The components of the device are as follows:

1. The permanent magnet configuration consists of seven magnets alternating with V-shaped iron spacers. The permanent magnet is made of a Grade 45 neodymium material.

2. A carriage was assembled to support the HE sensors and the magnet for movement across the railing. The carriage is made from aluminum due to its low magnetic permeability relative to steel. The wheeled carriage can smoothly traverse the test specimen along a longitudinal path while maintaining a constant distance between the sensors and the test strands.

3. An array of HE sensors positioned between the magnet poles detected the flux leakage in the regions of steel loss

4. A strain potentiometer is used as a distance calibrator which logs the distance traversed along the strand.

The sensors were activated and the Olson Instruments data acquisition system (DAS) recorded the voltage at a sampling rate of 100 Hz. The change in voltage is typically plotted using data acquisition and analysis software against time and distance.

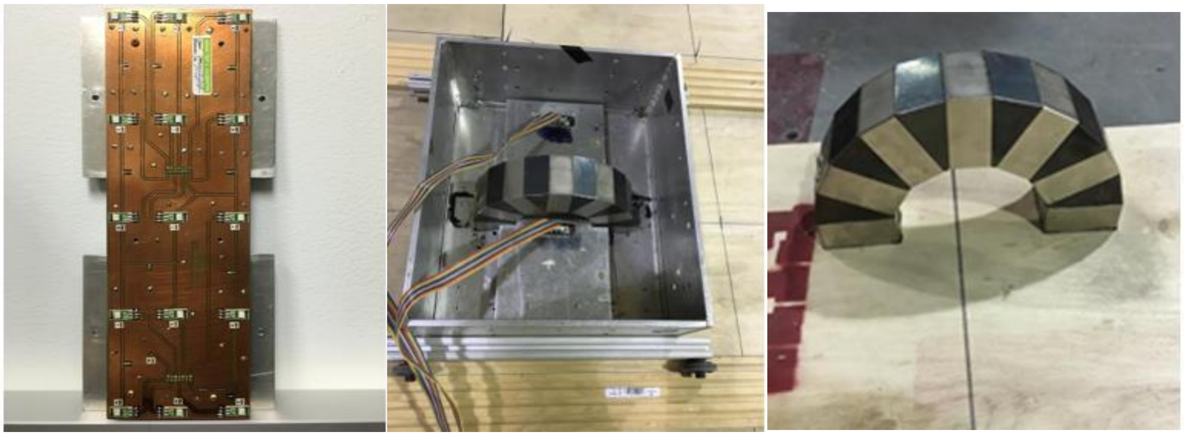

Figure 5-27: Sensor instrumentation: hall effect sensor array (left); carriage (center); and permanent magnet (right).

A bundle of 10 strand with 100% section loss was placed inside a plastic duct under an elevated platform. A study conducted by DaSilva et al. demonstrated that effect of corrosion is adequately simulated by removing steel wires within seven wire strands or cutting the strands similar to the configuration shown in Figure 5-28 (Dasilva, Javidi, Yakel, & Azizinamini, 2009). The complete loss of metal cross-section was considered an extreme test condition only for assessment of the NDT and not necessarily simulating actual structural behavior of stressed tendons. The strands were magnetized by the permanent magnet by traversing the system over the strand bundle. The HE sensors placed between the magnet poles detected the flux leakage.

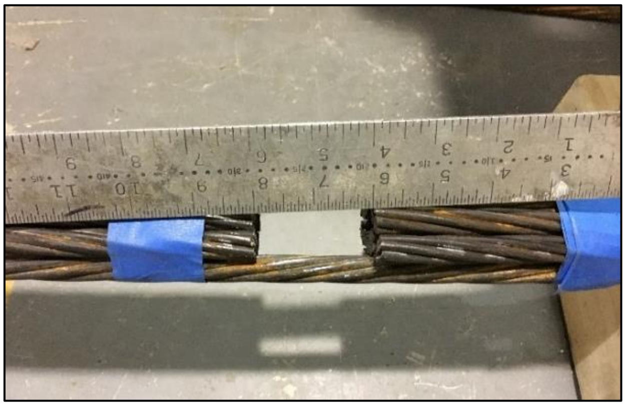

Figure 5-28: Group of strands with simulated defect.

The magnet with HE sensors positioned between the poles is traversed over a group of strands as shown schematically in Figure 5-29 (left). The defect is positioned in the middle of the plastic duct. When the magnetic assembly passes over the defect the vertical component of the flux leakage is detected which is shown in Figure 5-29 (right).

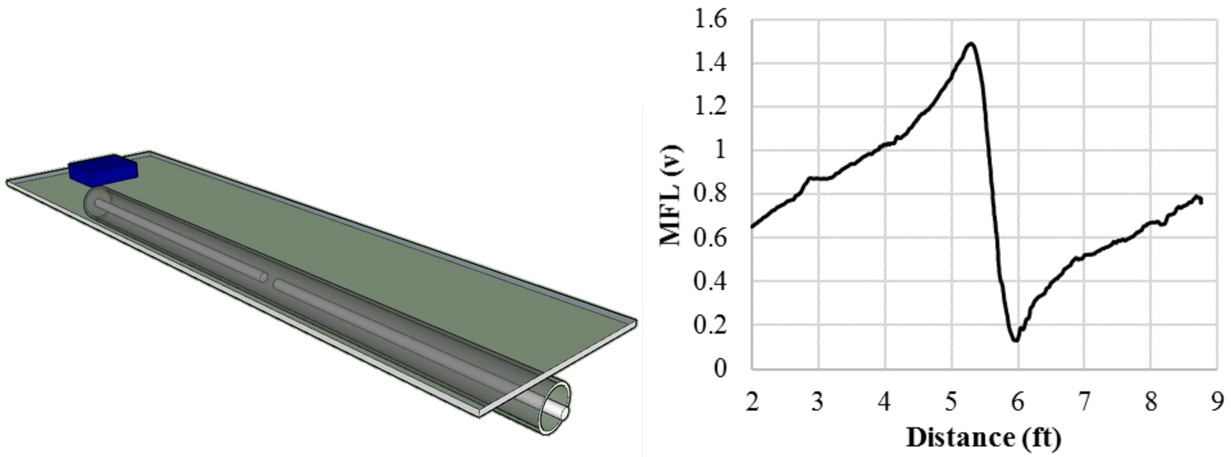

Figure 5-29: Schematic test layout (left) Leakage field for complete defect strand (right).

Mild reinforcement in actual concrete structures, located at a relatively shorter distance from concrete surface than strands, has significant effect on MFL signals. Without signal processing and other filtering techniques, these secondary signals of lesser significance, are similar to signals caused by defects as shown in Figure 5-30. This mild reinforcement can mask the defect signal making it difficult to identify the damage in strand. Researchers were able to differentiate the signals caused by strands and mild reinforcement using an electromagnet and signal processing techniques (Sawade & Krause, 2007; H Scheel & Hillemeier, 1997).

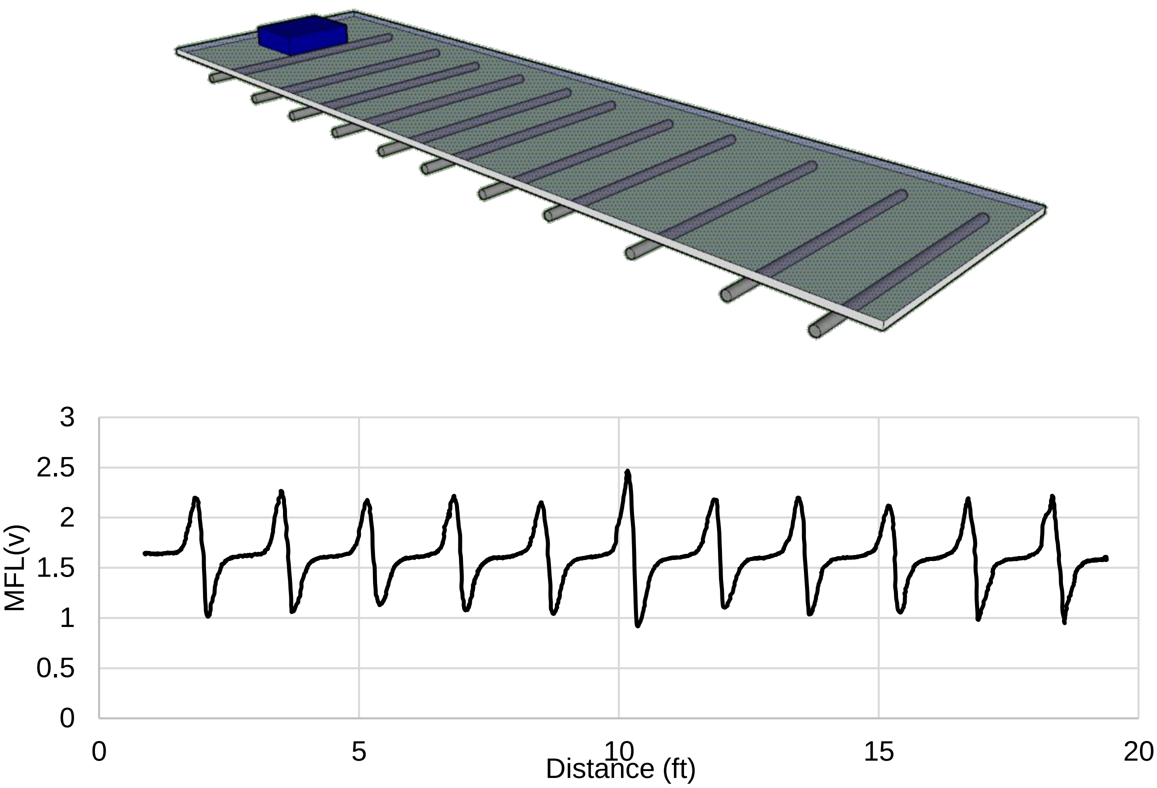

Figure 5-30: Schematic test layout (top) and mild reinforcement leakage field (bottom).

5.2.2 Challenges for Application to Internal Tendons

Ability to preemptively identify corrosion damage of steel strands is vital to ensure that appropriate mitigation of corroded tendons is made before failure of PSC components. Identification of damage of steel strands in actual PSC members may be masked by presence of interfering ferromagnetic sources such as mild reinforcing steel. One of the aim to apply MFL to PT strands was to validate an approach to assess strand cross-section loss for systems with secondary ferromagnetic sources. The general concept to reduce the effect of secondary ferromagnetic sources is to take the difference in output voltage readings between control and test cases (Rehmat et al., 2017).

5.2.3 Methodology for Laboratory Test

Large-scale laboratory tests were conducted to isolate characteristic defect output signals from complicating output signals due to secondary ferromagnetic sources. Full-scale field testing on decommissioned PT bridge segments and components were conducted to assess strand cross-section loss of systems with secondary ferromagnetic sources on actual bridge materials and geometries.

In PSC structures, the high strength strands are mostly located near accessible surfaces. For the test specimen, a 20-ft long elevated plywood platform as shown in Figure 5-31 was constructed to simulate a scenario where the strand was placed along the length. Non-ferromagnetic media (such as concrete, air, and plywood) do not influence the measurements. Rails were placed on the plywood platform to facilitate carriage travel along the length of the sample. Underneath the plywood platform, steel strands were placed inside a 4 in plastic duct. All tests were conducted using ten continuous and/or discontinuous seven-wire high strength strands. Strand placed near an accessible surface would allow magnetic saturation to be readily achieved. At the start of the laboratory experiments, the strands were magnetized by moving the permanent magnet over the strands in one direction several times (more than five times) so that the magnetic domains point in a uniform direction. The laboratory tests were run by manually traversing the carriage containing the magnetization device and HE sensors over the plywood platform along the strands at a velocity of ~1 ft / sec. The signal amplitude was monitored as a function of the carriage position in real time to identify changes in voltage.

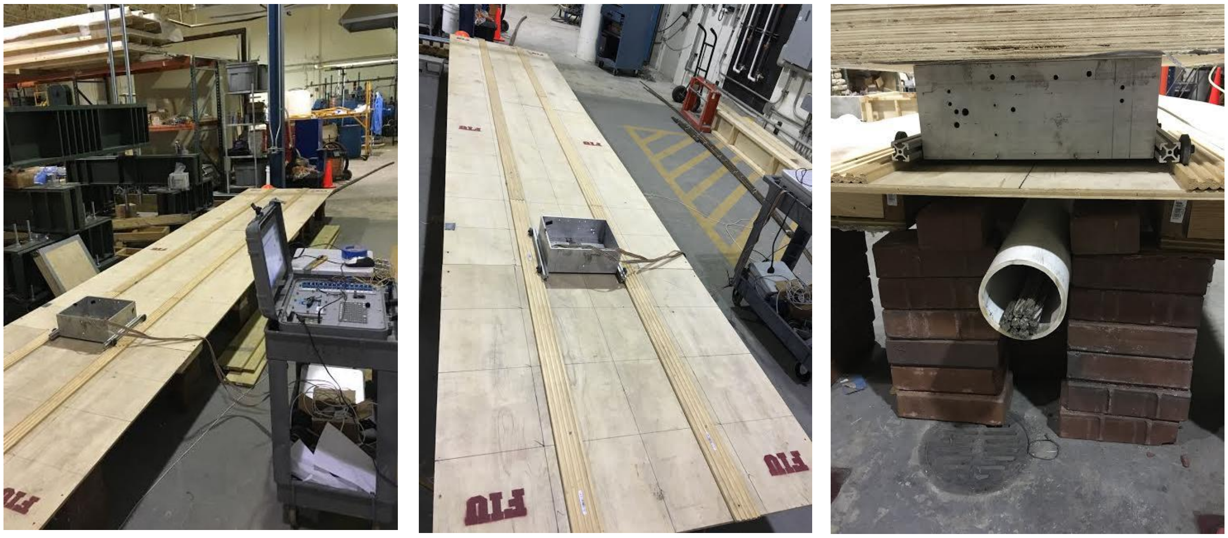

Figure 5-31: Laboratory test setup.

Figure 5-32: Complete and partial physical discontinuity.

Different scenarios of strand damage size and location as well as presence of mild reinforcing bars were simulated. For the laboratory tests 14%, 50% and 100% damage scenarios (Figure 5-32) were made on to strands as summarized in Table 5-2. Strand defects are labeled as Undamaged (ND) and Damaged (D) strands tests. Mild steel rebar (#3) were used as transverse reinforcement when tested. Table 5-3 gives the summary of all laboratory test conditions and Figure 5-33 indicates test geometry.

Table 5-2: Damage simulation in strands

Nomenclature	Location, ft from one end	No. of cut wires (Total 70 wires)	Percentage loss of area
Damage scenario 1	4.5	10	14%
Damage scenario 2	8	35	50%
Damage scenario 3	14.5	70	100%

Table 5-3: Summary of laboratory tests

Test series	Test configuration	Transverse reinforcement	Active or residual MFL
Undamaged Strands Tests	ND1	No	Active
	ND2	Yes	Active
	ND3	Yes	Residual
Damaged Strands Tests	D1	No	Active
	D2	Yes	Active
	D3	Yes	Residual

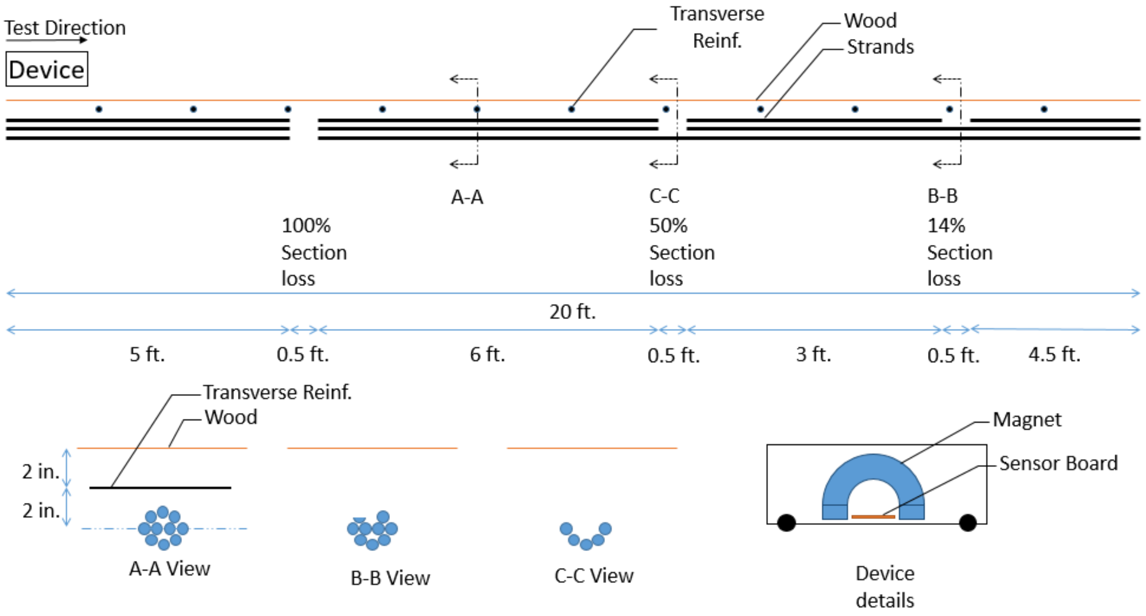

Figure 5-33: Laboratory test setup.

5.2.4 Laboratory Test Results

Disturbances of the magnetic field at the location of the damages were detected by the HE sensors. Characteristic signals of defects on the voltage-distance graph are in the shape of a peak and valley as shown in Figure 5-34. The observed inflection can be ascribed to many factors including the defect size, magnetic strength, distance between HE sensors, and strands, etc.

Initial testing assessed the effect of defect gap size. For the 100% damage scenario, the results showed similar signal characteristics for all test conditions (gap sizes between 0.1 in and 6 in). It was apparent that the peak-peak (P-P) voltage for the 0.1 to 6 in conditions did not show highly differentiating results. The P-P amplitude of different defect lengths did not tend to reduce significantly with the decrease in length of defect as shown in Figure 5-34 . The 0.1 in gap condition did show a slightly lower P-P voltage due to the short gap length in agreement with results reported (H Scheel & Hillemeier, 1997). Therefore, in further testing described here, a 6 in gap was used as an approach to minimize the influence of gap length on signal strength even though it is understood that this gap length is not representative for the onset of corrosion.

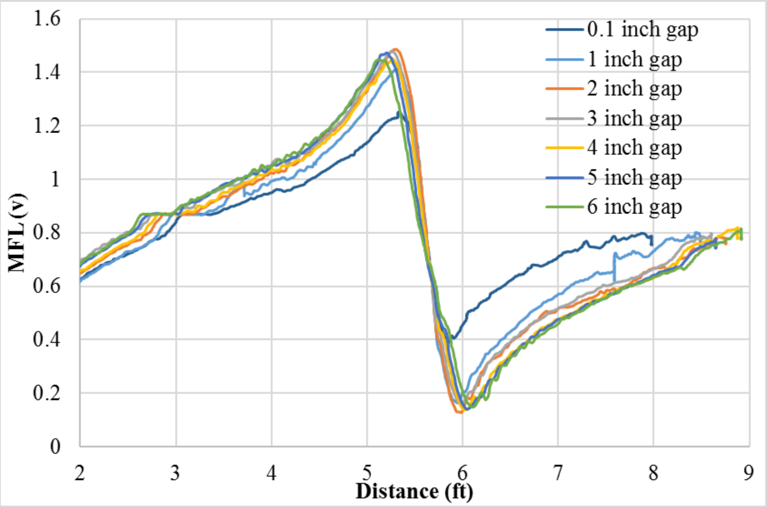

Figure 5-34: Effect of defect length on signal strength.

The tests were run in active field with no transverse reinforcement and serves as baseline results. Result from the undamaged strands test, ND1, shows a constant voltage as the sensors are placed along the strand length with the boundary effect peaks at the ends (Figure 5-35). The test result from the damaged strands test, D1, show a curve with peaks and valleys proportional to the level of damage i.e. 100%, 50% and 14% section loss. The difference of these two tests (D1-ND1) eliminates the boundary effect and displays the approximate damage location and its magnitude more explicitly.

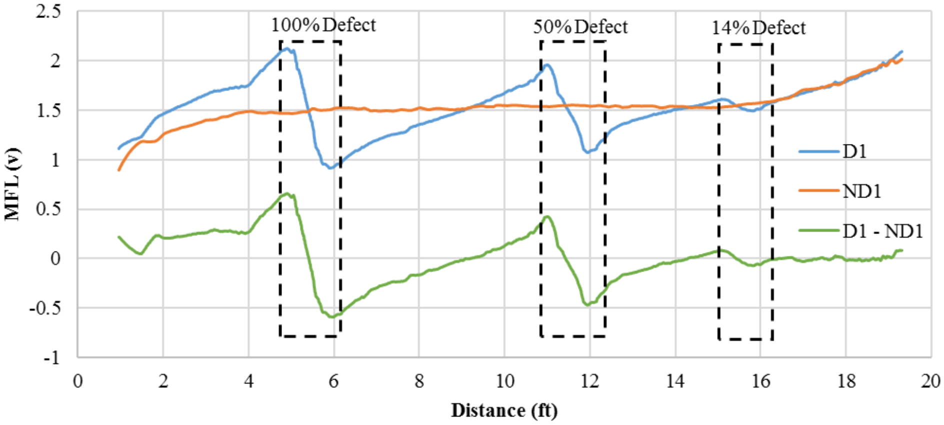

Figure 5-35: Results of MFL tests for test D1, ND1, and their difference (D1-ND1).

The transverse reinforcements were perpendicular to the magnetic field lines and their behavior alone under an active or residual field is a single peak with no valley curve. The test results of undamaged and damaged strands with transverse reinforcement in an active and residual magnetic field are shown in Figure 5-36 (top) and (bottom) respectively.

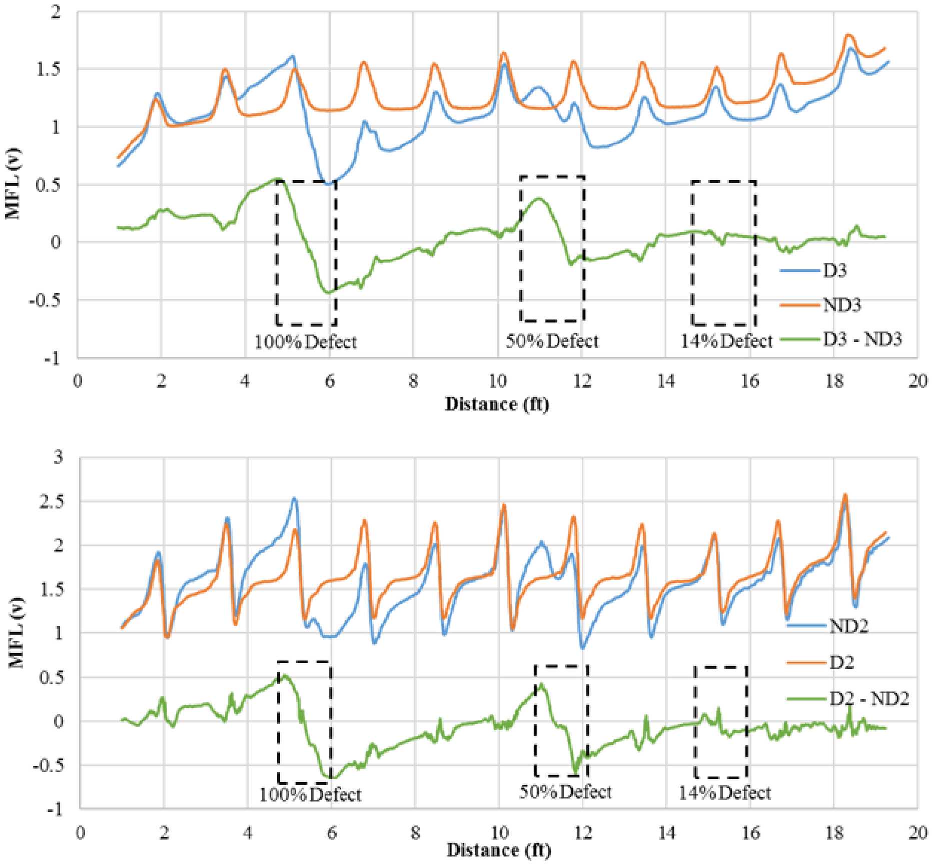

Figure 5-36: Laboratory test results with residual (top) and active (bottom) magnetic field.

In the active field measurement, the results from undamaged and damaged strands with transverse reinforcement displayed a series of peaks and valleys. Results from the damaged strand test, D2, were difficult to interpret. The subtraction of test ND2 voltage data results from D2 data shows a trend similar to Figure 5-35 where distinct peaks and valleys were obtained for each defect. Localized peaks which resulted from the subtraction at the location of transverse rebars were considered artifacts and can be ignored. For the residual field measurement, there was reduction in the signal strength but the trend is similar to the active test. The reduction in signal also diminished the magnitude of artifact local peaks due to the presence of the transverse rebars. For both tests, the section loss of 100% and 50% are clearly seen but 14% section loss is relatively obscured.

5.2.5 Methodology for Segment Testing

Testing was carried out on the bridge segment to validate the capability of the MFL and demonstrate the practical application to identify strand metal loss in internal tendons. Similar test protocols from laboratory testing were followed for the field test measurements. The control test setup typically consists of two cases: (1) strands without damage and (2) no strands within the metal duct.

The segments transported to FIU from the Fort Lauderdale-Hollywood International airport were used for NDT as shown in Figure 5-37. Each dissected test segment had a span length of almost 10 ft. The MFL testing was limited to the 3-in diameter ducts in the cantilever of top slab. There exists #3 distribution reinforcement in the slab with the arrangement shown in Figure 5-38.

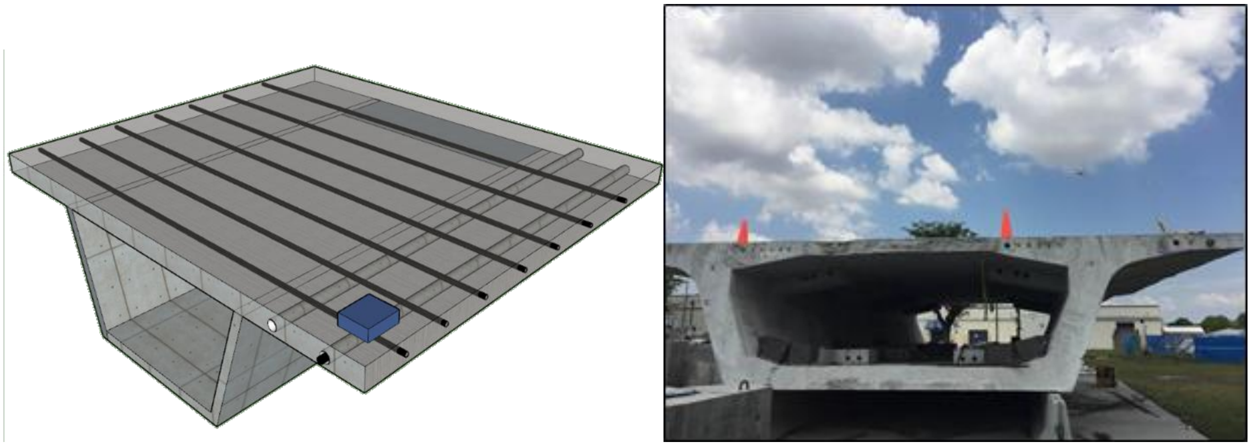

Figure 5-37: Bridge segment for testing.

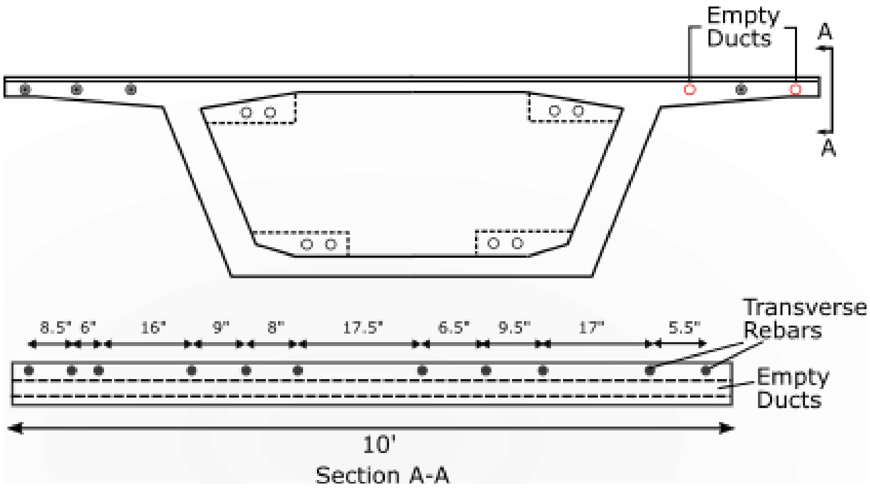

Figure 5-38: Schematic drawing of bridge segment.

5.2.6 Segment Test Results

A summary of testing on the bridge segment is given in Table 5-4. For tests on the bridge segment (1) strands with damage, (2) strands with no damage, and (3) no strands, were used. In the damaged strands test (SD) a bundle of seven strands was placed inside the empty steel duct. The test strand had a complete geometric discontinuity of 4 in to simulate complete metal loss. The defect was positioned between two transverse rebars. The undamaged-strands test (SND) was run with a set of seven strand with no geometric discontinuity. The no strands test (SN) was run without using the strands. All tests (SD, SND and SN) were run in the active magnetic field. Magnetization of the strands were masked by the presence of the steel duct and incomplete saturation of strands would limit the use of residual field method to detect MFL.

Table 5-4: Summary of tests on bridge segment

Test Series	Test Configuration	Strands	Active or Residual MFL
Damaged Strands Test	SD	Yes	Active
Undamaged Strands Test	SND	Yes	Active
No Strands Test	SN	No	Active

The test results from SD, SND and SN are shown in Figure 5-39. The defect in a strand bundle, when present (SD), was located mid span of the bridge segment (~5 ft). The response was complicated due to the numerous inflections associated with transverse reinforcement. As shown in Figure 5-36, the large inflections were well correlated to the placement of transverse steel (the dotted vertical lines). Indeed, an inflection in the signal was correlated to the defect. To eliminate the effect of transverse rebars, the approach of taking difference in signals was again adopted. The difference between damaged strands and no strands SD-SN (re-plotted in Figure 5-40) well highlights the defect location. The localized inflections in Figure 5-40 which resulted due to subtraction at the location of transverse rebars can be considered artifacts.

Alternatively, and as shown in earlier laboratory tests, taking the difference in damaged and undamaged strands SD-SND (Figure 5-41) can be viable. The results from the subtraction shows a large amount of artifact inflections as shown in Figure 5-41. The large inflection represents the geometric discontinuity while the local inflections occur due to the difference in amplitude of signals during testing and the subtraction procedures adopted in the study.

In all field testing, it was apparent that MFL measurements using active magnetic field method can be used to identify defect locations even with the complications associated with the presence of transverse reinforcing steel and construction materials in full scale bridge geometries.

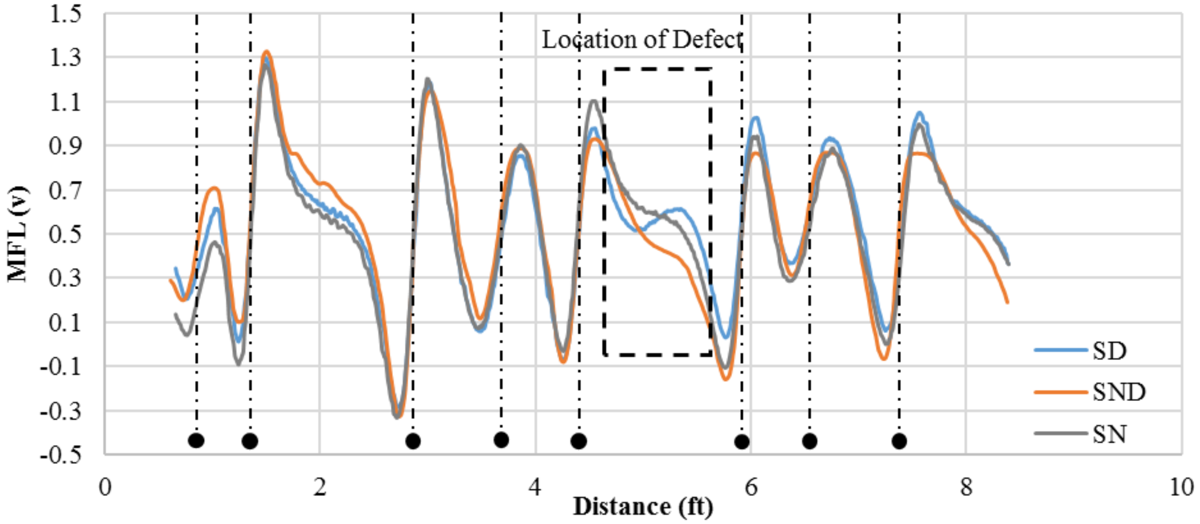

Figure 5-39: Test results of bridge segment.

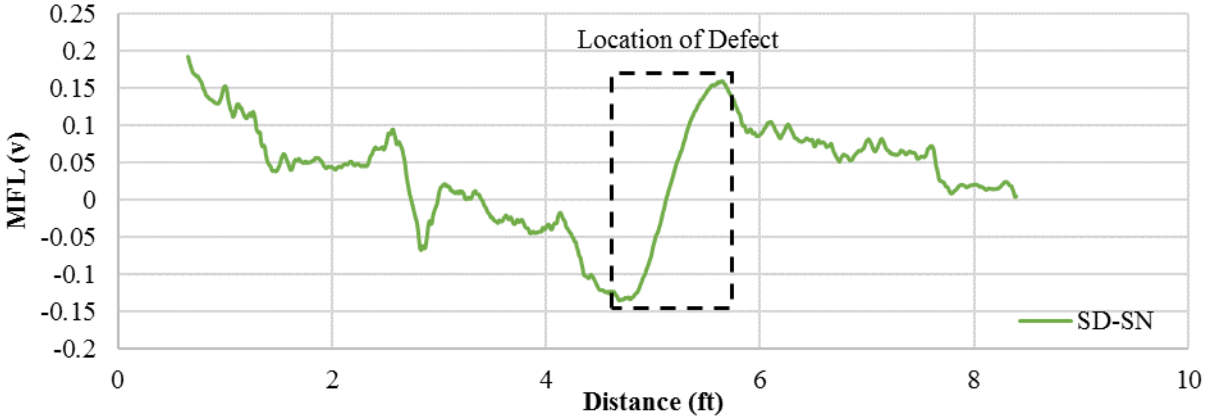

Figure 5-40: Difference of test SD and SN.

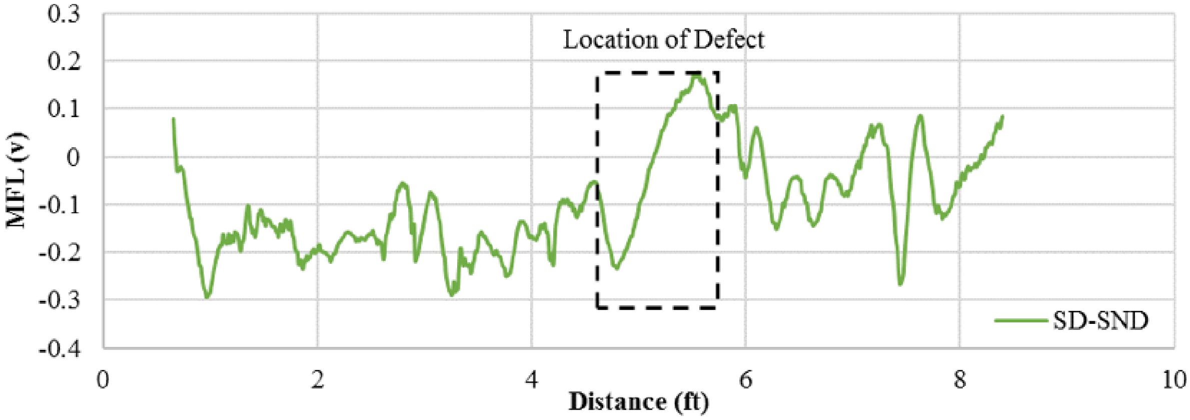

Figure 5-41: Difference of test SD and SND.

The testing showed promising results of using MFL to identify defects in internal PT strands. The MFL method is effective in identifying the location of the defect but the presence of secondary ferromagnetic sources can affect the amplitude of signals for a smaller steel area loss. The testing described here provided an approach to minimize the effect of secondary ferromagnetic sources. However, there may be limitations in identifying the location and magnitude of smaller defects. This limitation was thought to be due to incomplete magnetic saturation due to the low magnetizing capability of the permanent magnet.

5.2.7 Parameter-Based Signal Characterization

The MFL signals can be affected by many parameters such as percentage of damage in strand, defect length, embedded depth of strand, transverse reinforcement depth/spacing, and location of HE sensors etc. These factors can affect the P-P amplitude, the gradient, and shape of the waveform. To qualitative see the effect of these factors on flux leakage signals, a parametric study was conducted.

5.2.7.1 Effect of Single Transverse Rebar

A single transverse mild reinforcing bar without any prestressing strands was placed at various depths to see the effect on flux density. In addition to placing the HE sensors between the poles of the magnet, the sensors were placed at three different positions (1.75 in, 2.25 in and 2.75 in) to the rear of permanent magnet. Placement of the sensors in between the magnet resulted in typical peak-valley signals with magnitudes correlating to rebar depth. The output signal obtained when placing the sensors to the rear of the magnet resulted in valley signals of various magnitudes that also correlated to the depth of the transverse bar. The difference in signals obtained from the various sensor placements can be potentially used for reduction of interfering signals from other ferromagnetic sources.

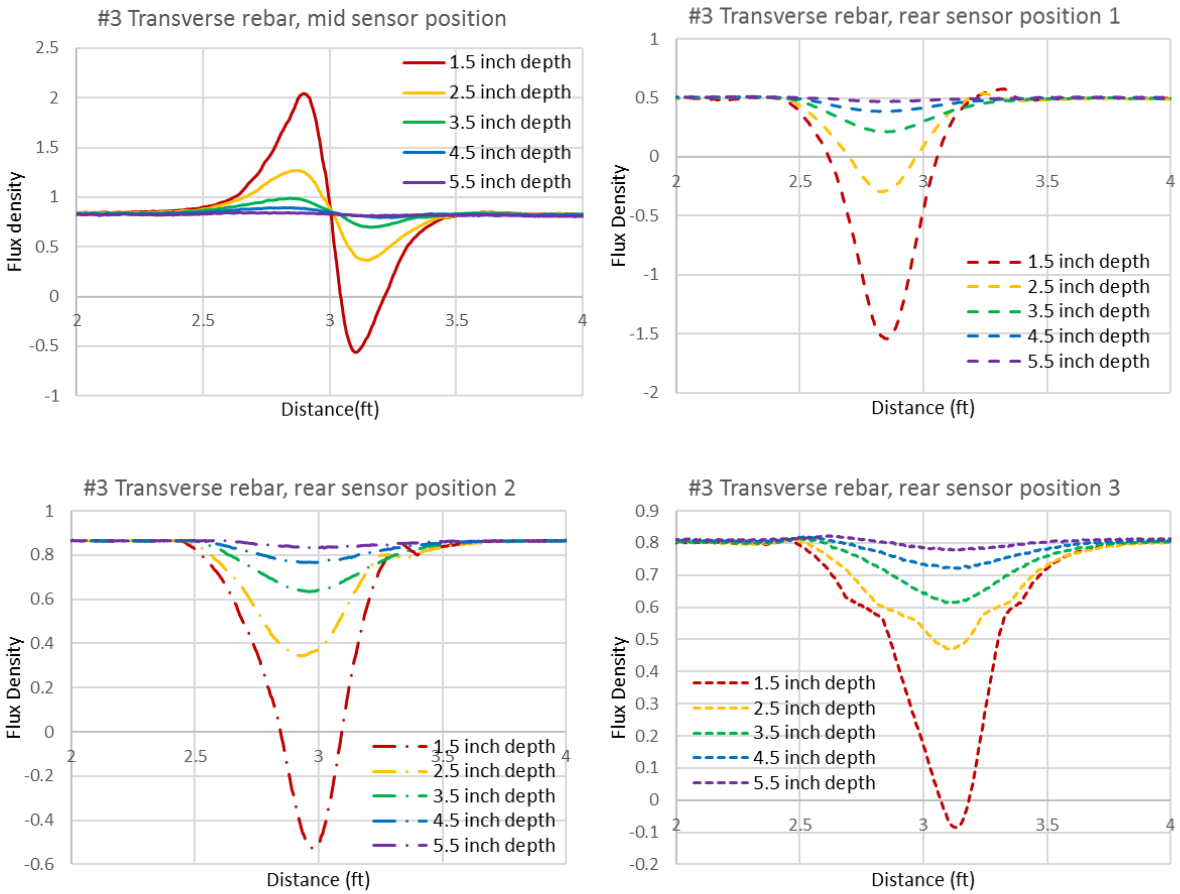

Figure 5-42: Effect of transverse rebar depth on signal strength as captured by sensors in four locations.

The various fluctuations caused by these transverse rebars are plotted in Figure 5-42. Besides the different waveform generated by different sensor positions, the peak to peak amplitude of transverse rebar shows that the there is significant reduction in the amplitude as the sensors to magnet distance increase as shown in Figure 5-43.

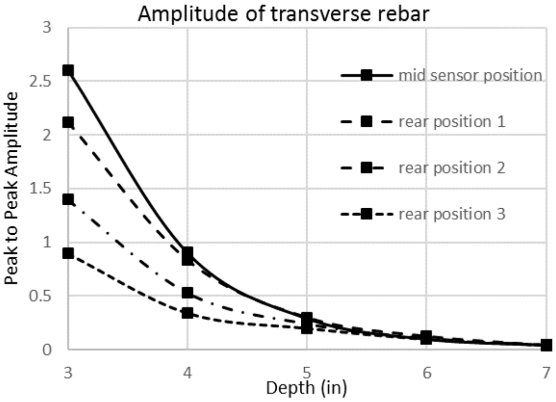

Figure 5-43: Amplitude variation against different depth of transverse rebar.

5.2.7.2 Effect of Transverse Rebar in Presence of Complete Defect Strand

Strand with a complete defect was placed under two transverse rebars with the defect centered to the assembly as shown in Figure 5-44. Measurements were taken in active and residual magnetic field. Sensors placed between the magnet poles showed a higher disturbance due to the presence of the transverse rebars compared to the generated waveforms from sensors placed to the rear of the magnet.

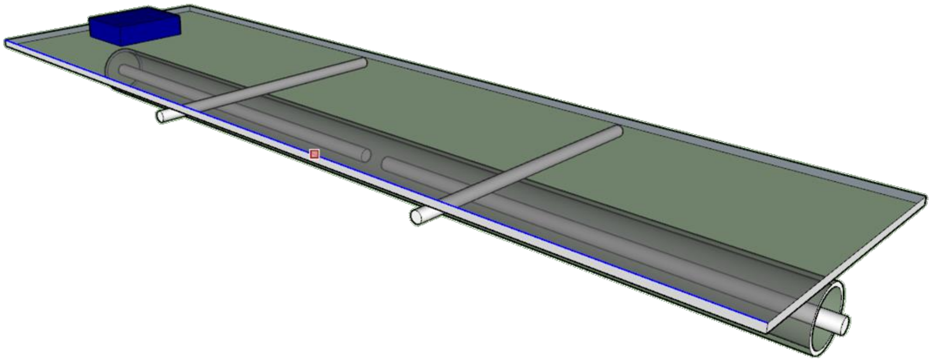

Figure 5-44: Schematic view of defect in presence of transverse rebar.

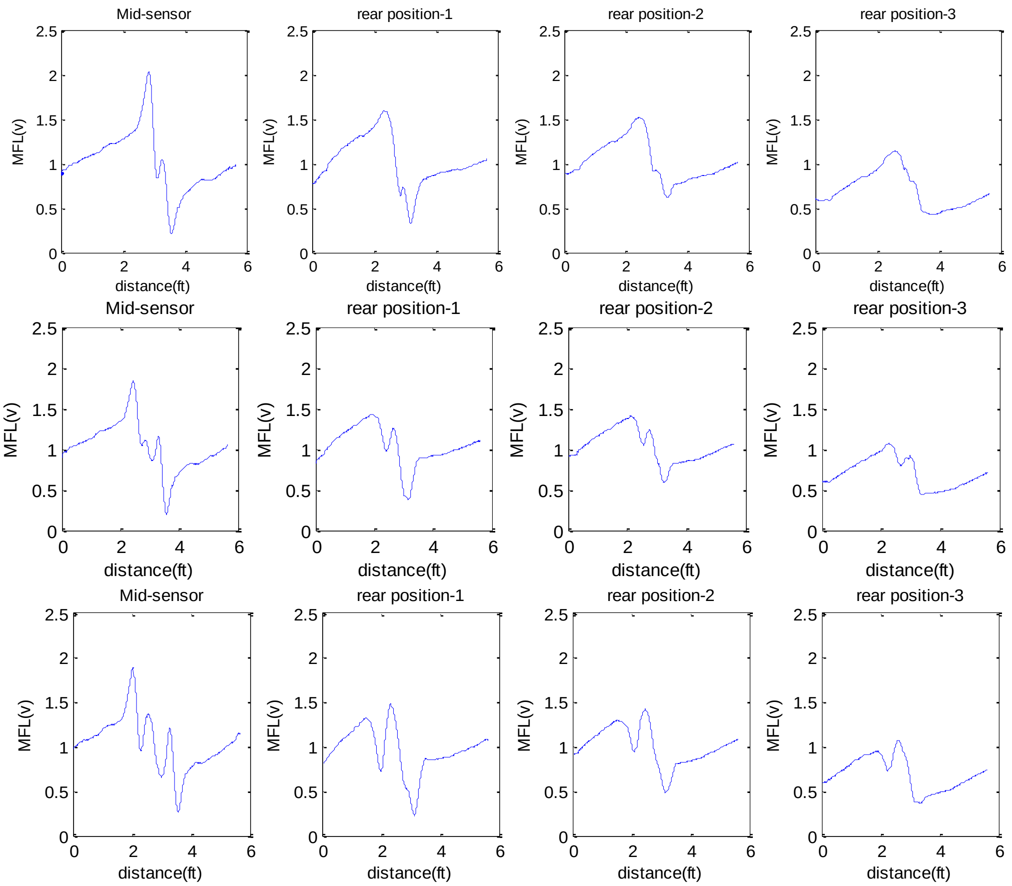

Figure 5-45: Variation of flux density for complete damage as captured by sensors placed at four locations; transverse rebar spacing at 5 inches (top), 10 inches (middle) and 15 inches (bottom).

The resultant flux signals from an array of sensor are given in Figure 5-45. The first column is results of HE sensors placed between poles. Column 2 to 4 corresponds to sensors placed 1.75 in, 2.25 in and 2.75 in rear of the magnet, respectively. The depth of strands was kept constant, and the depth of transverse rebar at 2.5 in from the top surface. The results obtained shows that the effect of transverse reinforcement reduces gradually as the distance of HE sensors from magnet increases. It was thought that residual magnetization of the transverse rebars could dissipate upon scanning by the HE sensors when placed to the rear of the magnet at greater distances. A careful analysis of the signals from a surface scanned with an array of sensors in different positions can aid in differentiation of signals obtained from transverse rebars and the defect in strands.

5.2.7.3 Effect of Defect Size in a Group of Strands

A parametric study was carried out on a bundle of strands where different percentage of defects were induced from 0% to 100% at increments of 10%. The different percentage defects are shown in Figure 5-46. The depth of strands and the gap width of defect were kept constant. It was observed that the P-P amplitude of defect increases with the defect percentage as shown in Figure 5-47. The quantification of P-P strength of different defect percentage can help in identification of extent of damage in a corroded strand.

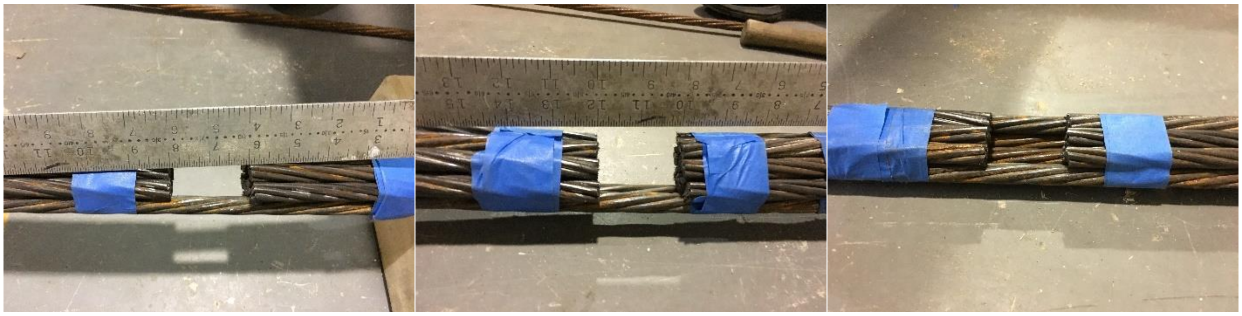

Figure 5-46: Different strand defect percentage 90% (left) 80% (center) and 50% (right).

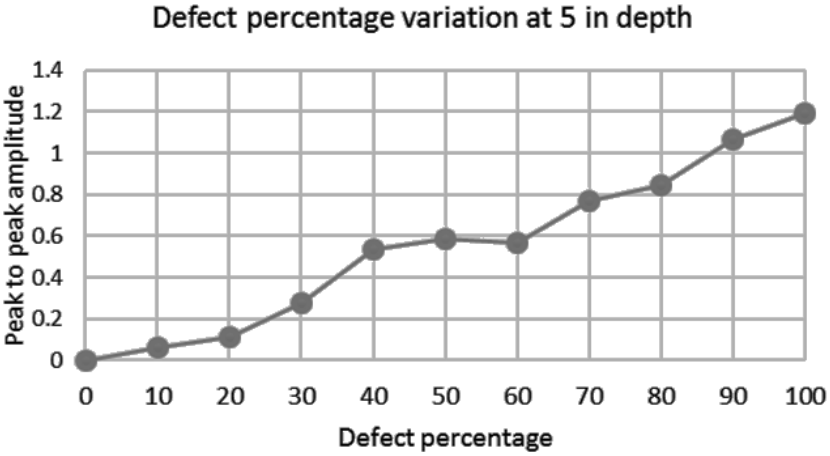

Defect percentage variation at 5 in depth

Figure 5-47: Change in amplitude for defect percentages.

5.2.8 Numerical Simulation

The purpose of a numerical simulation was to verify experimental results and identify possible improvement of the MFL system. Numerical modeling is performed as a magneto-static problem in which the fields are time-invariant. For the numerical analysis, FEMM and ANSYS, were used for 2-D and 3-D analyses, respectively. The magnetic material is defined as a neodymium iron magnetic (NdFeB 40/45) material with v-shaped spacers of iron. The strand is modeled as a cold drawn carbon steel embedded in an air medium. The magnetic elements generate flux flowing in the strand and most commonly these fluxes are perpendicular to axis of the defect. The flux lines generated in intact strand are shown in Figure 5-48 (top). A defect is introduced in the ferromagnetic material and the flux flow and leakage is observed Figure 5-48 (bottom). The defect causes a local change in relative permeability which is usually lower than the intact ferromagnetic material causing the flux to change its path. The magnitude of disturbance depends on the geometric properties of the defect.

A 2D (FE) analysis presented two challenges. First, the modeling a transverse rebar along the depth is not possible which gives conservative values of flux perturbations at the location of the reinforcement. Second, modeling of HE sensors is done as a line element which gives inaccurate values of flux leakage at the location of defects or transverse rebars.

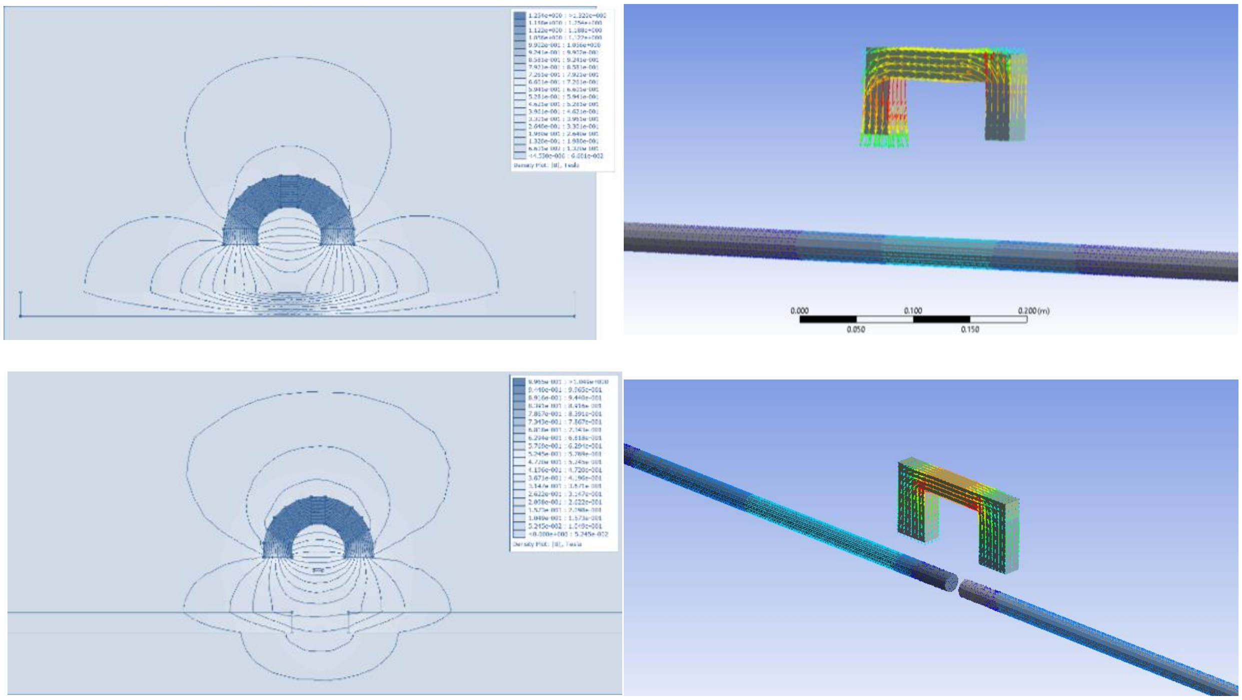

Figure 5-48: Magnetic flux through intact (top) and defect strand (bottom).

A 3D model of MFL was simulated with a strand having a 1-in defect gap located at 1.5 in from the face of the magnet. The numerical simulation of MFL requires an excitation field from a permanent magnet and positioning of the sensors which can detect the changes in flux density. Initially, the sensors were positioned in the middle of the permanent magnet since flux changes were more uniform in this region. Thereafter, sensor positions were changed to eliminate the effect of other ferromagnet and to model a remnant magnetic field. Figure 5-49 (top) shows the contour plot of the model with a complete defect. The signals are calculated by creating a series of models with the defect moving with respect to the excitation field generated by the permanent magnet. The resultant flux density is plotted in Figure 5-49 (bottom). The parameters used in the numerical study are the strength of permanent magnet, defect type and depth. For 3-D analysis in ANSYS, Solid98 is used which is a 10-node tetrahedral element. A flux parallel boundary is applied and reduced scalar potential (RSP) is used since no current sources are defined in the model. The relative permeability of materials and magnetic coercive forces are inputs for ANSYS. The relative permeability is the ratio of flux density of material to flux density in vacuum. The numerical analysis assists in the better understanding of the mechanism of magnetic field flow in an intact ferromagnetic material.

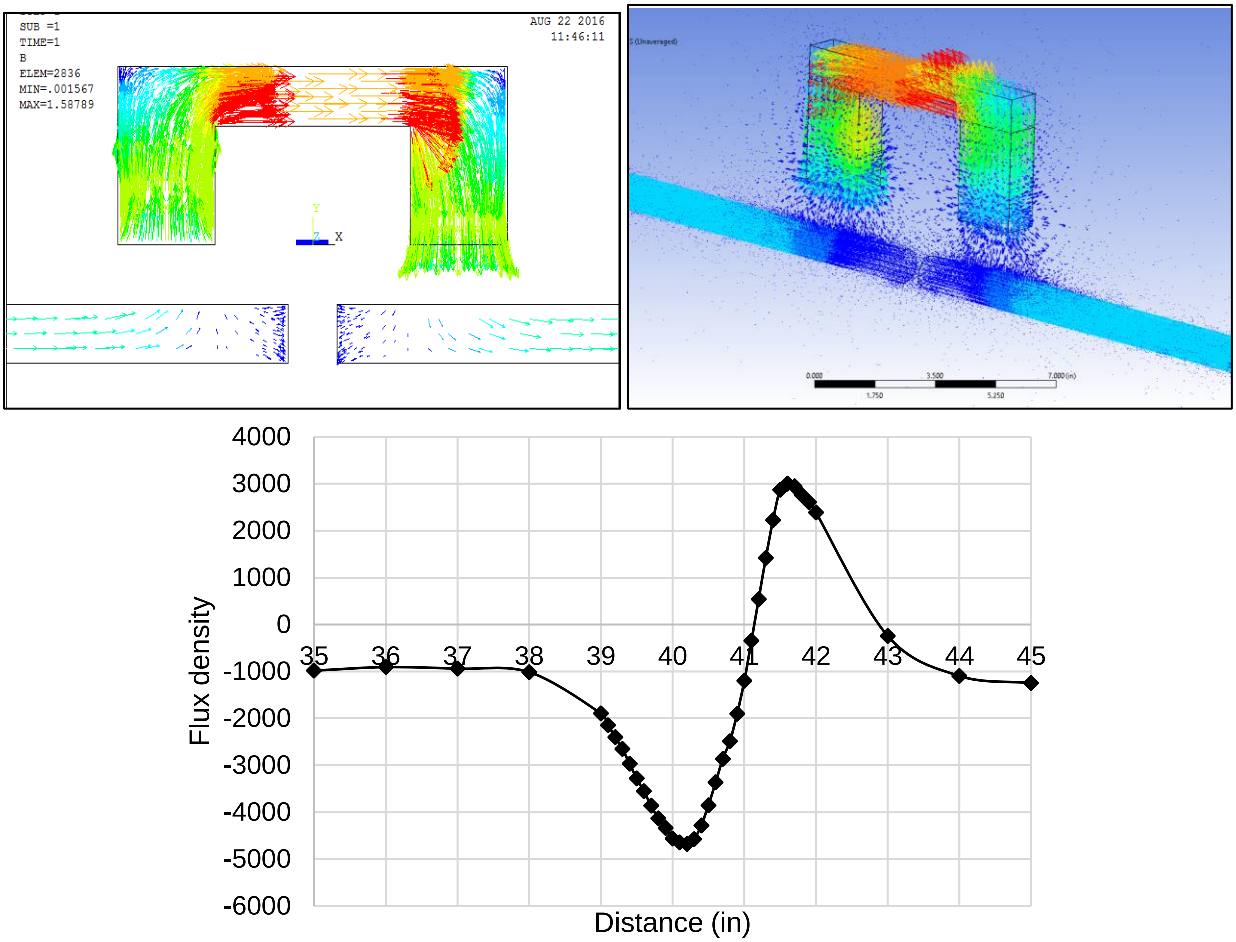

Figure 5-49: MFL through damaged strand (top) and resultant flux density plot (bottom).

5.2.9 Electromagnet

The permanent magnet used in the experimental program generates a constant magnetic flux density which has limited capability of strand saturation and flux penetration into a surface with embedded strands. The more practical approach of using MFL method is the use of an appropriate magnetic strength to saturate the steel strand, and the optimal placement of HE sensors. A varying magnetic strength can be provided using an electromagnet, whose configuration depends on the intended application. For example, a surface scanner may be more useful for strands located near probe surface. In case of strands in beam members, scanning of strand profile using a vertical assembly shown in Figure 5-50 (left) may be more practical.

Figure 5-50: Electromagnet application to MFL systems: application of electromagnet for vertical members (left) and surface scanners (right) (photo courtesy Dr. Hillemeier).

The possible options of an electromagnet are a coiled U-core, E-core or an alternate U-core cross-section depending on the application. Among the many factors which affect the strength of an electromagnet include number of turns of wire within the coil, amount of current flowing in coil, and the type of core material. The detailed design and fabrication of an electromagnetic surface scanner is proposed as future work.

5.2.10 MFL Test Summary

The study uses MFL method for damage detection of strands in laboratory setup and its application on a decommissioned bridge segment. The laboratory test results show that the active magnetic field can detect different physical discontinuity in strands alone. However, in presence of secondary ferromagnetic sources, disturbances and masking effects caused by mild reinforcements or steel ducts, can lead to complicated signals from which damage detection could become challenging. The laboratory setup shows that the effect of mild reinforcement can be reduced by data analysis techniques. A similar test setup and post data processing for bridge segment was carried out but only in presence of active field to detect a complete fracture of the strands. Segment results showed that the post processing implemented in the study can identify damage in strands.

The shape of the signal is affected by many factors including magnetization type, dimensional characteristics of defect, signal-to-noise ratio, and parameters which affect damage resolution. A study of some of the parameters was studied for characterization of defect signal which can be used in future study such as pattern classification and statistical identification of defect. A numerical study was used to validate the results of the laboratory tests. A detailed FE simulation results can be used to improve the MFL system by assisting in sensor positions and choosing appropriate magnetic field for strand saturation. Based on experimental study, the use of an electromagnet is a more practical approach which can improve defect detection capabilities. The application of the proposed methodology may not be generic for all PT system in bridges and there is a need to develop test protocols for MFL for PSC bridges.

5.3 INDUCTANCE MEASUREMENT METHOD

5.3.1 Laboratory Test Methodology

A laboratory tendon sample test bed was constructed to identify the effectiveness of the inductance method to detect strand metal loss. The laboratory setup was similar to MFL test setup described in section 5.2.3 and consisted of a 20-ft long sample with multiple strands encased in a 4-in PVC pipe. The 20-ft length sample had section loss of various degrees along the length including a 100% cut at 2.5 ft, a 50% cut at 10 ft and a 14% cut at 16 ft as described in Table 5-2. A plywood platform was placed 3-in above the PVC pipe for the full length of the sample to simulate the top of a segmental concrete slab. The plywood platform provided a support surface for the testing equipment as inductance measurements were taken at uniform intervals along the sample length as shown in Figure 5-51. Multiple inductor coil configurations were tested to find the best combination of depth of penetration and resolution. Depth of penetration of the field around the inductor coil increases with the diameter of the coil. However, it was found from experimentation that the resolution of the readings for section loss decrease as the coil increases in diameter. This is because a larger coil overlaps and includes influences of the non-damaged section of the strands (high inductance) as readings in vicinity of the defect (low inductance) are taken. Multiple iterations of testing showed that the coil diameter shown in Figure 5-51 provided a good balance of depth of penetration and resolution for the laboratory testing.

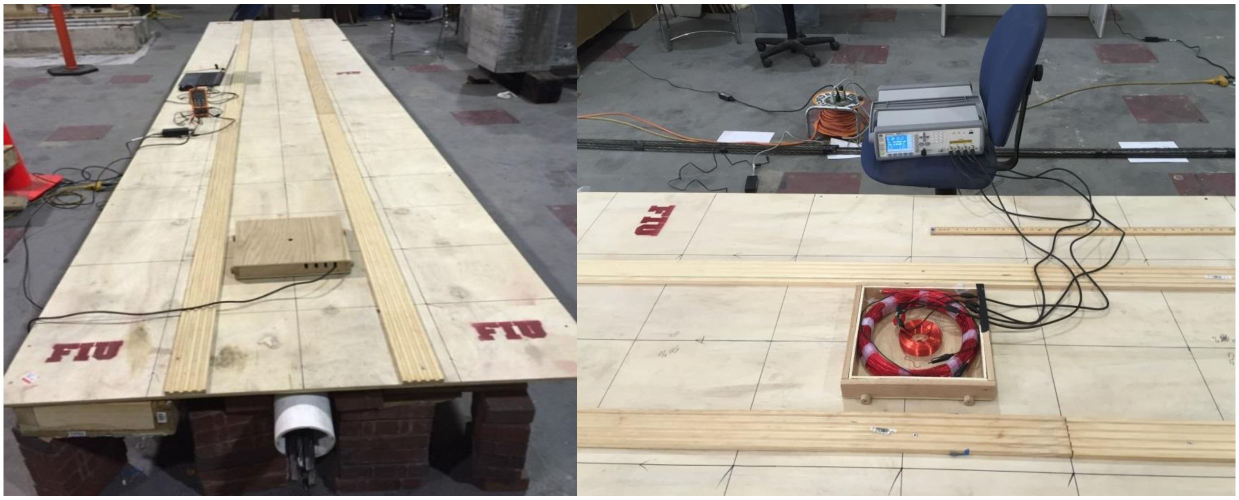

Figure 5-51: Laboratory setup (left) Inductance coil and inductance meter (right).

It is noted that the electrical characteristics of the materials used for tendons do not exhibit ideal electrical behavior. All components exhibit some form of resistance, capacitance and inductance. Most equations relating to the inductor describe an ideal case in which there are no parasitic resistance and capacitance involved in the inductor’s behavior. Real world inductors usually have some form of intrinsic parasitic behavior such as resistance and capacitance which should be considered. The precision of the measured value of inductance by an induction meter reflects the way the parasitics are taken into account. A high precision inductance meter produced the necessary test signal to generate the fluctuating magnetic field through the coil. The precision inductance meter applied a 2-volt alternating current (AC) test signal through the coil and the alternating expanding and collapsing magnetic field flux lines cut across the steel in close proximity to the coil.

5.3.2 Laboratory Test Results

Inductance measurements were taken at equally spaced points along the sample. The inductance measurement results of the test are shown in Figure 5-52. The large dip in inductance clearly indicates the 100% section loss on the steel strand (2.5 ft from the end of the strand). The dip in inductance mid-length corresponds with the 50% cut section and the smaller dip in inductance at 16 ft indicates the 14% loss location.

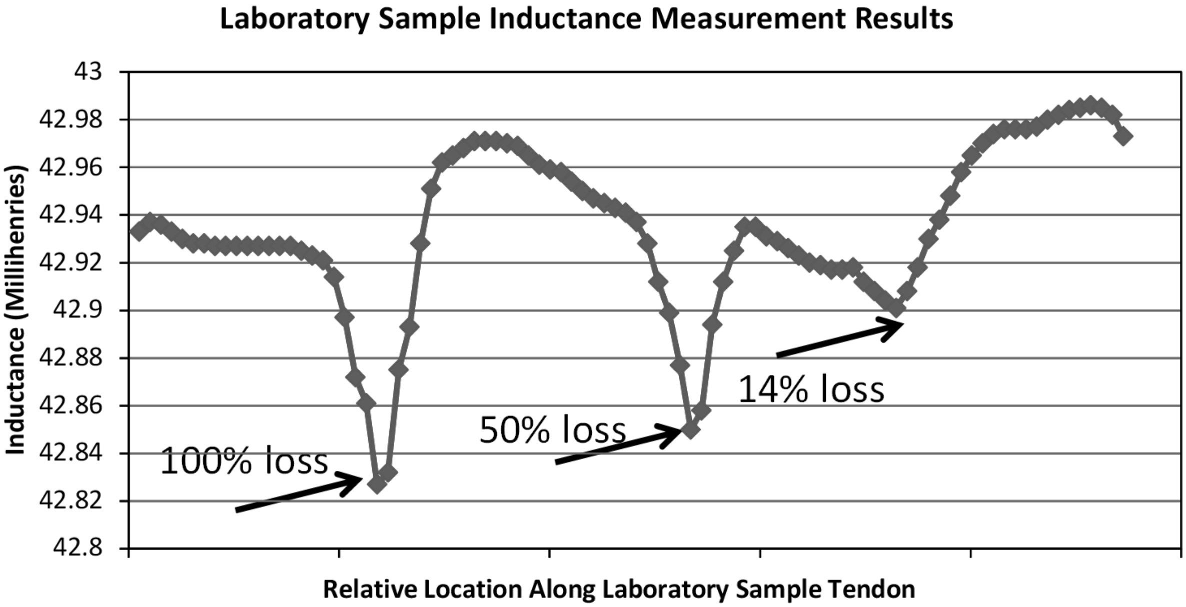

Figure 5-52: Plot of inductance measurement values along the length of the laboratory sample.

5.3.3 Segment Testing Methodology

In addition to the laboratory sample testing discussed previously, the inductance method was also implemented on decommissioned segments. The segment tendon conduit was made up of a galvanized steel duct with approximately 3.5 to 4 inches of concrete cover. The existing original strands in the segment conduit were removed and a set of strand was installed for the test.

Segment testing involved a challenging testing environment. The segment tendon cover depth varied by as much as ~0.5 in from one end of the 10-ft long segment to the other. In addition, the segment had transverse mild reinforcement as well as bundled prestressing strands on the top and bottom of the slab spaced. Challenges in the inductance measurement for segmental bridges include interference from steel components other than the tendon strands. Preliminary testing of the segment showed that inductance readings increased when in close proximity to the transverse mild reinforcement which is both above and below the internal post-tensioning strands.

Multiple tests of the segment showed that the inductance of the secondary transverse reinforcement was additive to the inductance of the longitudinal tendon strands. In addition, a myriad of other complicating factors including steel conduit material non-uniformity as well as conduit depth non-uniformity offered challenges not encountered in the relatively simple laboratory sample previously discussed.

A different approach was needed for the segment sample as compared to the approach taken for the laboratory sample. Therefore, a baseline calibrated approach to testing was adopted in order to reliably take into account the myriad of unpredictable secondary factors present. A baseline set of inductance reading were established for a single strand in the conduit and then subsequent readings were taken for additional strand configurations. Inductance measurements were taken at 107 equally spaced points along the 10 ft segment.

Figure 5-53: Modified second prototype elliptical coil used for inductance testing on the top slab of segment.

The effect of the top transverse rebars in the segment was significant because they were closer to the coil than the longitudinal strands. Since the point of the investigation was not to measure the transverse bars but the longitudinal strands, a modification of the coil dimensions was required to reduce as much as possible the interference effects of the transverse reinforcement on the inductance readings. The redesign of the coil was influenced by the need to keep the depth of penetration of the magnetic field and reduce the size of the coil. A compromise in the design resulted in an elliptical coil which was positioned so the narrow dimension was parallel to the longitudinal axis of the strands. The longer dimension of the coil in the perpendicular direction to the strands did not have a significant detrimental effect because the reinforcement was in the transverse direction as shown in Figure 5-53.

5.3.4 Segment Test Results

The inductance measurement results of the test are shown in Figure 5-54. The spikes in inductance in Figure 5-54 are due to transverse mild reinforcement and transverse prestressing strands. The decreasing trend of the inductance from left to right is caused by the increasing distance between the inductor probe and the strands as the conduit slopes down relative to the top of the concrete. More importantly, however, is the fact that the inductance shows an increase of inductance for the larger (more strand) samples at the locations of transverse reinforcement. See Figure 5-55 for a clearer depiction of the difference in readings between the “1-strand” sample and the “6-strand” sample. This implies that, as long as there is a calibration test data set made for future numerical comparison, the location of strand loss can even be detected under transverse reinforcement.

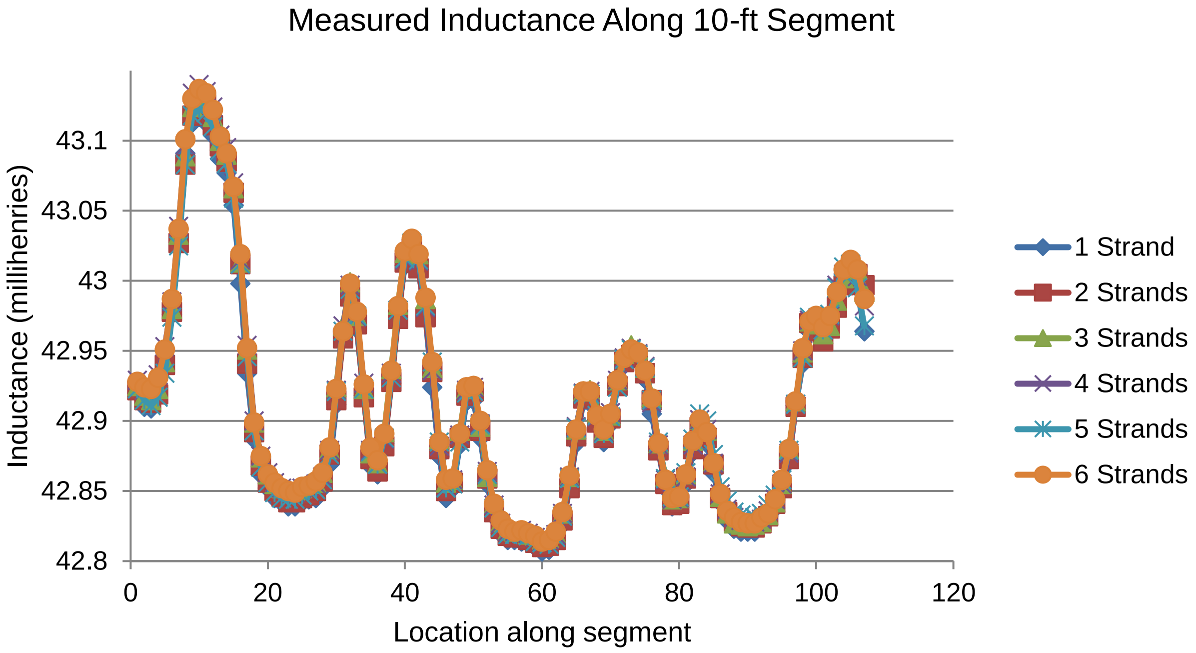

Figure 5-54: Plot of inductance values along the length of the segment for cases of 1, 2, 3, 4, 5, and 6 strands.

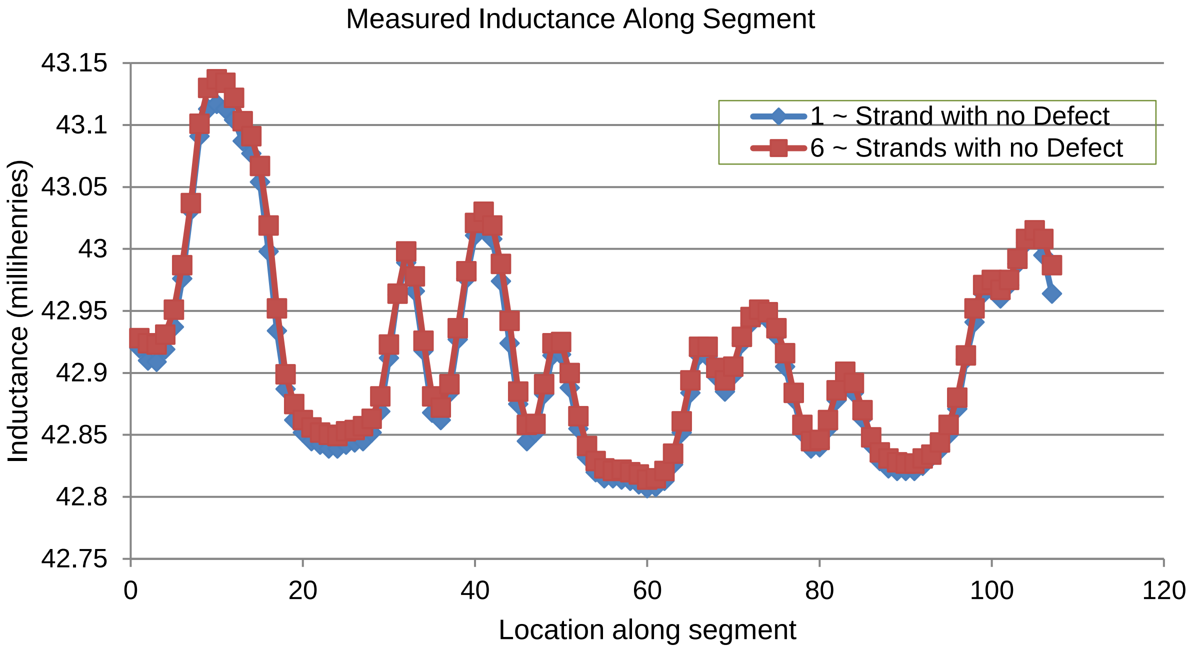

Figure 5-55: Plot of inductance meter measured values along the length of the segment comparing 1-strand and 6-strand tests only.

5.3.5 Inductance Method Summary

Iterative trials of different testing equipment configurations over the course of the project found that the major factors affecting the inductance method test data include the quality of the inductance meter, coil geometry (probe), number of turns of the coil (probe), frequency of the test signal, concrete cover over the tendon, the thickness of the wall of the steel conduit and magnetic interference (shielding) from transverse reinforcing steel. Overall it was found that the inductance method, being an electromagnetic method, is very sensitive to any secondary steel elements in a segmental bridge.

In realistic situations for segmental bridge internal tendons, where complications such as transverse reinforcement or nonlinear conduit profiles are present, a baseline calibrated approach is necessary for the inductance method to consider these secondary factors and to provide reliable results. It is anticipated that a baseline set of inductance reading could be established at the beginning of the service life of the bridge and subsequent readings could be taken at prescribed time intervals to compare to the baseline data. It is recommended that, for reliable comparison purposes, subsequent readings should be taken at the same exact locations as the baseline readings using the same testing equipment (probes) and test settings (current and frequency). Interestingly, as indicated by the laboratory testing of a tendon sample, when no transverse reinforcement is present and the conduit is a uniform distance from the surface of the concrete, the inductance method can locate defects as small as without a previous baseline calibration run for comparison. The section loss for the laboratory sample was indicated by a localized drop in inductance at a location along the length corresponding to the defect.

Future potential improvements to the inductance method may include modification to inductor coil (probe) geometry to sharpen (localize) the inductance reading and modification of the coil turns and wrapping method to increase depth of penetration of the test field. Other future potential improvements also include the use of a more precise inductance meter with a larger voltage test signal. Data set collection and processing is also an important issue to be investigated since several data sets averaged together may provide a better quality data set due to cancellation of data set outliers caused by electromagnetic noise.

6 SUMMARY OF IMPORTANT FINDINGS AND RECOMMENDATIONS

The objective of the project was to identify practical and effective NDT technologies and approaches to utilize those technologies that can be used for the condition assessment of internal PT tendons. In the project, several commercially available technologies were tested before and during deconstruction of a PT bridge. The same segments were made available as a testbed at FIU for other NDTs. To this effect, sequential demolition of the bridge was carried out by Finley Engineering Group, Inc., based on safety considerations, and an analytical study was made which replicated the stages of construction of a segmental bridge to calculate stresses at intermediate and final structure. The analytical model of the structure provided checks for various deconstruction stages such as stability of superstructure, mid-span cut and segment removal. The analytical study provided a theoretical response of the structure which was, in general, not inconsistent with on-site NDTs. A visual survey was carried out on the portion of the bridge that was demolished. This post-deconstruction survey revealed some partially grouted ducts, honeycombing in concrete, and strands showing signs of corrosion. However, most of the components of post-tensioning systems showed no deficiencies and were in good condition.

6.1 SUMMARY OF RESULTS

Several on-site field tests were conducted on the bridge to observe the overall response of the structure and to investigate the condition of bridge components. The IR provided mobility spectrum which is indicative of flexibility of the structural element. Within a span, the mobility of the bridge decreased at the junction of deck and web and showed higher values in the middle of the span due to lower stiffness. A higher mobility of the bridge, along the width and length of bridge, was observed after partial demolition of the bridge which is indicative of the reduction in global stiffness of the structure. Although the results of the IR test could not identify any specific damage in the bridge, the results of IR tests at different times during the service life of a bridge can be used to evaluate the health of the structure.

IRT with active heating could not be conducted in the field due to constraints during bridge deconstruction. The field work instead aimed to identify practicality of heating and differential cooling by passive heating. In Florida summer conditions, passive heating from the sun did allow differential heating especially when surfaces are partially sheltered. The bridge concrete surface conditions did not contain significant anomalous features that could be detected by IRT. After demolition, access to the strands in the bridge segments for IRT by active heating using a torch did not give good resolution of embedded steel due to the good thermal properties by the bulk concrete itself. IRT on available segments from failed tendons from another bridge was able to differentiate deficient grout from hardened grout. The on-site field tests on tendons using IRT tests required further investigation into deficient grout. Therefore, a set of laboratory IRT test were conducted and preliminary tests showed that inductive heating can detect wire damages and differential grout materials. The findings support the use of inductive heating where the steel components are heated differentially from the surrounding grout. Further investigation is required to develop an adaptable inductive heater, determining heat required to provide good resolution and minimization of thermal reflections.

Acoustic emission tests carried out under no-traffic conditions was effective in pinpointing the location of calibration hammer strikes. The results showed that the tendon breakages produce substantial vibration amplitude which is above typical traffic noise and thus can be measured at a distance of 20 ft or more. However, a numerical source location routine using 2-D and 3-D models showed poor to fair results due to high level of noise generated by the saw cutting operation and 3-D nature of the structures. The optimization of sensor layout and using improved signal processing techniques could be advantageous for better results. The IBIS system was used in overall structure movements during saw-cutting operation but due to high stiffness of reinforced structure prevented moveable measurement.

The MFL method was used to assess the damages in PT strands. Initial tests on the laboratory tests showed the capability of the system to detect geometric discontinuity in strands alone using the active magnetic field. However, the secondary ferromagnetic such as mild reinforcement lead to complicated signals. A methodology was adopted to reduce the effect of transverse steel reinforcing bars which was applied on laboratory and extended to decommissioned segments. Results showed that the methodology implemented can reduce test artifacts from the transverse reinforcing bars and identify damage in strands. A numerical study was carried out to validate the MFL results and improve the system by optimizing sensor positions and choosing appropriate magnetic field for strand saturation. The permanent magnet has limitations in full-scale structure testing, therefore use of an electromagnet can provide magnetization under different boundary conditions. Depending on the use, an electromagnet can be designed for small scale tests to large scale surface scanners. This surface scanner can provide robust damage detection in strands located near flat surfaces. The design of a surface scanning electromagnet using a magnetic yoke has been studied but the development of this technology is proposed as future work.

The inductance method was tested under laboratory and field conditions. In controlled laboratory settings, the method was found to be effective to identify metal loss in steel strand in ideal cases without presence of secondary reinforcing steel. For segment testing, the inductance method identified strand section loss but interfering signals due to transverse mild reinforcement causes spikes in the inductance reading. Improvements to the method can be made possibly including the quality of the inductance meter, coil geometry, number of turns of the coil, frequency of the test signal, concrete cover over the tendon, the thickness of the wall of the steel conduit and magnetic interference (shielding) from transverse reinforcing steel.

6.2 RECOMMENDATIONS

The laboratory and field testing of a bridge at Fort Lauderdale provided an overview of meritorious applications and disadvantages of different NDE technologies. Although phenomenon of most of the non-destructive methods is fully understood and implemented through advanced commercially available technologies, the wide range of applications required for monitoring of civil engineering structures, is a challenging task.

The application of many available NDE requires trained manpower and therefore may not necessarily be easily accessible for non-specialized end user. Advanced Infrared cameras have made IRT a popular NDE method. Preliminary results from IRT results have shown promising results for grout deficiency and wire breakage, however technology to apply inductive heating still needs development. Acoustic emission is an established technology which was used for detecting wire breakages but the method requires expert end user to establish effective sensor placement as well as to differentiate wire breakage signals from ambient conditions. Owing to the simple testing procedure and commercial availability, IR method can detect mobility response by user with limited training but determination of impacts on structural integrity would require the assessment of an engineer.

The MFL method, has been widely used for damage detect in pipeline walls, but its application in detecting strand damage in complex configuration including internal tendons has been limited due to lack of test protocols to minimize complicated signal interpretation. The analysis results of MFL requires expert systems and the evaluation relies on experience of the user. Improvements in the inductance method is anticipated through use of modifications to the testing technology, high precision inductance meter and improvements in data processing techniques

REFERENCES

AASHTO. (2010). *LRFD Bridge Design Specifications*. *American Association of State Highway and Transportation Officials*. Washington, D.C.

Al-Naemi, F. I., Hall, J. P., & Moses, A. J. (2006). FEM modelling techniques of magnetic flux leakage-type NDT for ferromagnetic plate inspections. *Journal of Magnetism and Magnetic Materials*, *304*(2). https://doi.org/10.1016/j.jmmm.2006.02.225

ASTM. (2010). ASTM C1740-10 Standard Practice for Evaluating the Condition of Concrete Plates Using the Impulse-Response Method. West Conshohocken, PA: ASTM International. https://doi.org/10.1520/C1740-10

Azizinamini, A., & Gull, J. (2012a). *FDOT Protocol for Condition Assessment of Steel Strands in Post-tensioned Segmental Concrete Bridges: Volume II (FDOT Research Project BDK80-977-13)*. Miami: Florida International University.

Azizinamini, A., & Gull, J. (2012b). *Improved Inspection Techniques for Steel Prestressing/Post-Tensioning Strand (FDOT Research Project BDK80-977-13)*. Miami, FL: Florida International University.

Beitelman, T. E. (2000). Tensile Test Results of Post Tensioning Cables From the Midbay Bridge Background. Structures Research Center, Florida Department of Transportation.

Corven, J., & Moreton, A. (2013). *Post-Tensioning Tendon Installation and Grouting Manual (FHWA-NHI-13-026)*. Washington, D.C.: Federal Highway Administration.

Corven Engineering, I. (2002). *New Directions for Florida Post-Tensioned Bridges, Volume 1 of 10: Post-Tensioning In Florida Bridges*. Tallahassee, FL: Florida Department of Transportation.

Dasilva, M., Javidi, S., Yakel, A., & Azizinamini, A. (2009). *Nondestructive Method to Detect Corrosion of Steel Elements in Concrete (NDOR Research Project Number P597)*. Lincoln, NE: University of Nebraska, Lincoln.

Ghorbanpoor, A., Borchelt, R., Edwards, M., & Abdel Salam, E. (2000). *Magnetic-Based NDE of Prestressed and Post-Tensioned Concrete Members - The MFL System (FHWA-RD-00-026)*. McLean, VA: Federal Highway Administration.

Harris, D. (2003). *Test and Assessment of NDT Methods for Post-Tensioning Systems in Segmental Balanced Cantilever Concrete Bridges*. Tallahassee, FL: Florida Department of Transportation.

Lau, K., & Lasa, I. (2016). Corrosion of prestress and post-tension reinforced-concrete bridges. In *Corrosion of Steel in Concrete Structures* (pp. 37–57). Elsevier. https://doi.org/10.1016/B978-1-78242-381-2.00003-1

Li, Y., Tian, G. Y., & Ward, S. (2006). Numerical simulation on magnetic flux leakage evaluation at high speed. *NDT & E International*, *39*(5), 367–373. https://doi.org/10.1016/j.ndteint.2005.10.006

Olson, L. (2010). Innovations in bridge superstructure condition assessment with sonic and radar methods. *Structural Materials Technology*, (2), 1–12.

Olson Instruments Inc. (2008). *System Reference Manual 2008 Slab Impulse Response*. Wheat Ridge, CO.

Pollock, D. G. D., Dupuis, K. K. J., Lacour, B., & Olsen, K. K. R. (2008). *Detection of Voids in Prestressed Concrete Bridges using Thermal Imaging and Ground-Penetrating Radar (WA-RD 717.1)*. Olympia, WA: Washington State Department of Transportation.

Powers, R. G., Sagues, A. A., Virmani, Y. P., & Sagüés, A. A. (n.d.). *Corrosion of Post-Tensioned Tendons in Florida Bridges (Research Report No. FL/DOT/SMO/04-475)*.

Rehmat, S. e, Sadeghnejad, A., Valikhani, A., Chunn, B., Lau, K., & Azizinamini, A. (2017). Magnetic Flux Leakage Method for Detecting Corrosion in Post Tensioned Segmental Concrete Bridges in Presence of Secondary Reinforcement. In *Transportation Research Board 96th Annual Meeting* (Vol. 221, pp. 1–15).

Sawade, G., & Krause, H.-J. (2007). Inspection of Prestressed Concrete Members using the Magnetic Leakage Flux Measurement Method - Estimation of Detection Limit. In *Advances in Construction Materials* (Vol. 2007, pp. 639–649). https://doi.org/10.1007/BF02716787

Scheel, H., & Hillemeier, B. (1997). Capacity of the remanent magnetism method to detect fractures of steel in tendons embedded in prestressed concrete. *NDT & E International*, *30*(4), 211–216. https://doi.org/10.1016/S0963-8695(96)00058-8

Scheel, H., & Hillemeier, B. (2003). Location of Prestressing Steel Fractures in Concrete. *Journal of Materials in Civil Engineering*, *15*(3), 228–234. https://doi.org/10.1061/(ASCE)0899-1561(2003)15:3(228)

Szielasko, K., Kloster, A., Dobmann, G., Scheel, H., & Hillemeier, B. (2006). High-Speed, High-Resolution Magnetic Flux Leakage Inspection of Large Flat Surfaces. In *European Conference on Nondestructive Testing* (pp. 1–8).

Taghinezhad, R., Gull, J., Pham, H., & Olson, L. (2017). Vibration Monitoring During the Deconstruction of a Post-tensioned Segmental Bridge: Case Study. In *Transportation Research Board 96th Annual Meeting*. Retrieved from https://trid.trb.org/view.aspx?id=1438448

Xu, F., Wang, X., & Wu, H. (2012). Inspection method of cable-stayed bridge using magnetic flux leakage detection: principle, sensor design, and signal processing.

Journal of Mechanical Science and Technology, *26*(3), 661–669. https://doi.org/10.1007/s12206-011-1234-x

Zuoying, H., Peiwen, Q., & Liang, C. (2006). 3D FEM analysis in magnetic flux leakage method. *NDT and E International*, *39*(1), 61–66. https://doi.org/10.1016/j.ndteint.2005.06.006

APPENDIX A INFRARED THERMOGRAPHY AND INDUCTIVE HEATING

A.1 INFRARED THERMOGRAPHY BACKGROUND

Infrared thermography (IRT) is a type of photography which uses a camera that detects infrared radiation across a focal range and converts that radiation into a recorded digital image within the visible light spectrum which indicates the variation in temperature by different colors. The recorded digital image created by the infrared camera can take a variety of spectrum formats depending on the user’s needs. The images presented followed the “rainbow color scale” which depicts higher temperatures toward the yellow end of the spectrum and lower temperatures toward the opposite blue end of the spectrum. Intermediate temperatures are indicated by the intermediate colors of the visible spectrum. The IR camera used for this project also produced a temperature scale which showed the maximum and minimum temperatures corresponding with the recorded image. The varying intermediate temperatures within the image could be interpolated from its corresponding intermediate color.

IRT may be performed on a subject that has only been heated, directly or indirectly, by the sun in which case the IRT method is described as passive thermography (Passive IRT). Passive IRT has the advantage of providing the ability to easily obtain images over a large field of view as the results require only solar energy to heat the test subject.

Active Infrared thermography (Active IRT) involves heating the subject by means that are outside the limits of what the subject would normally experience. Active IRT by induction heating was used on the tendon test samples to create detectable temperature transients on the outside of the test samples which would not be present under Passive IRT conditions.

There are several Active IRT methods available to provide additional heating of the prestressing strand within the post-tensioning tendon. The strands may be heated by direct electric current (DC) in which case the electrical resistance of the strand itself causes the heating. Access to the ends of the strands inside the tendon are required to implement the DC heating method. Heating by conduction from the outside of the tendon is another method of active heating in which heat could be applied to the duct which would then heat the grout and strand indirectly. A disadvantage of conductive heating is that the duct could be damaged by large temperatures. Heating by induction is another option for Active IRT. Unlike heating by conduction or DC, induction heating allows the ferrous material to be heated without direct contact with the prestressing strands or damage to the existing protective duct and grout. In addition, any non-ferrous material within the vicinity of the induction coil is not directly heated but is indirectly heated by contact with the ferrous material. This is an advantage in this situation as the grout and the duct of the tendon are not excessively heated, with the duct experiencing the least amount of heating during the process. Induction heating of the prestressing strand within a post-tensioned (PT) duct is well suited to this application because the tendon can be left intact and uniformly heated along its length, providing an environment in which Active IRT may be effectively utilized.

A.2 INDUCTION HEATING BACKGROUND

Induction heating is an established technology in the realm of industrial heating and forming of manufactured steel components. One of the major advantages of induction heating is its adaptability to the shapes required for various component configurations. Induction heating coils of cylindrical or flat "pancake" configurations can be modified to fit many different geometries and applications.

The basic mechanism of induction heating is the creation of eddy currents in the ferrous core of an inductor under a changing magnetic field. A changing magnetic field is induced in the inductor core because some of the changing magnetic field lines of the inductor pass through the inductor core. This mechanism is analogous to the behavior of a transformer under an alternating current (AC). In this analogy, the primary coil is the inductor and the secondary coil is the core of the inductor. Since the secondary coil in this analogy is a coil of only one turn, small currents within the core itself are formed which give rise to significant resistive heating.

In practice, induction heaters are usually comprised of the following general electrical processes:

1. An alternating line current is rectified to a smooth direct current. The DC is electronically processed using MOSFET switches to provide a high frequency inverted signal.
2. The high frequency inverted signal is routed through a “tank” circuit made up of a resonant parallel capacitor and inductor (coil).
3. The alternating signal in the resonant tank circuit causes the current through the inductor (coil) to alternate and thus the magnetic field of the inductor expands and collapses at the frequency of the circuit.
4. The rapidly expanding and collapsing electromagnetic field around the coil is transferred to the secondary coil which in this case is the core of the inductor.

Figure A-1: Induction heater with the copper coil (inductor).

A.3 EXPERIMENTAL INVESTIGATION OF LABORATORY SAMPLE

A test was run in the laboratory on experimental small scale tendon samples using IRT and induction heating to heat the prestressing steel. Three-foot-long tendon samples were tested with varying degrees of discontinuities in each strand at approximately mid-length of each sample as shown in Figure A-2.

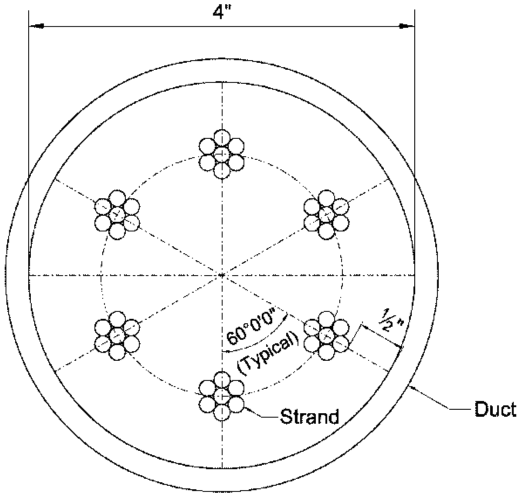

Figure A-2: Typical arrangement of strands in the 3-ft long sample.

The typical induction heater is powered by a DC power source rectified from an AC line voltage. For the testing involved in this project a high voltage high current DC power source was required to provide the current necessary to effectively heat the large mass of prestressing strand inside the sample tendons. The 30-volts 20-amp DC power supply used for this project was powered by a 120-V 60-Hz line voltage.

The DC power supply powers an inverter circuit made up of two high power MOSFET “N” type transistors (MOSFET) which produce a high frequency AC. The DC power supply connects to the gates of the MOSFETS through 240-ohm resistors from the power source. The two MOSFET switches are connected in a way so that they are alternatively switched on and off by the alternating high and low gate voltages. When the gate voltage is high the MOSFET switches on and allows the current to drain to ground. The voltage required to keep the circuit oscillating was approximately 12 volts.

The parallel tank circuit is made up of a coil (inductor) and a capacitor in parallel. The coil is made up of a wound copper tube which is center tapped to the power source through a toroid choke inductor. The toroid inductor serves as a choke to keep the high frequency signals from the tank circuit from feeding back into the power supply. Every tank circuit has a certain frequency at which it oscillates. An advantage of the parallel Royer oscillator is that it adjusts the frequency of the circuit, within limits, to the frequency that will produce resonance for the existing properties of capacitance and inductance in the tank circuit. Therefore, the capacitance and inductance may be adjusted to provide the desired frequency. The main copper coil acts as a transformer in relationship to the ferrous work piece (strand) being heated. The copper coil acts as the primary coil of the transformer, and the strand acts as a single turn secondary coil. Due to the high frequency of the current through the primary copper coil, localized eddy currents are produced in the strand which cause heating of the work piece. In case of this project, the secondary (strands in the tendon sample) varied in number (mass) and defect configuration. The current drawn through the circuit varies based on the mass of the secondary coil. A small secondary mass would pull a relatively smaller current than a larger secondary mass. The current demand for heating a 3-strand tendon, for example, is less than that required for a 5-strand tendon.

The smaller samples required only a current of a few amps from the DC power source, so there was little concern for circuit overheating. The larger samples required more current and therefore more voltage to effectively heat the sample. Circuit overheating became a problem with the MOSFET gates as the higher voltage exceeded their capacity and the MOSFET were damaged. This problem was solved with a 12-volt regulator to the gates which limited the gate voltage but allowed the voltage and the current to the coils to be increased significantly. Heat sinks were also added to the MOSFET transistors to dissipate heat more effectively. A fan was also utilized to cool the induction heater system as the circuit wiring also began to melt when the current exceeded approximately 5 amp. The fan allowed the circuit to run continuously up to a current of 12 amp.

The experimental process was comprised of the following steps:

1. The circuit voltage and current limits were adjusted on the DC power supply.
2. The power to the induction heater circuit was turned on to begin oscillation.
3. The tendon sample was placed within the copper core of the induction heater.
4. The coil was moved at a uniform rate along the length of the tendon sample.
5. IRT images were taken during and after the heating process.

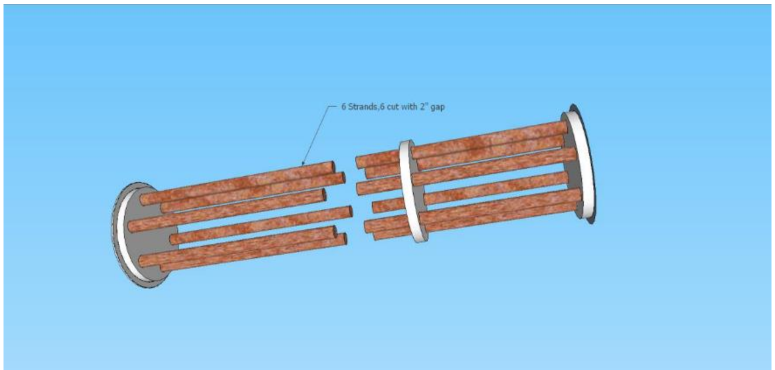

Figure A-3: Typical arrangement of strands for sample-1. (All 6-strand cut with 2-in gap at mid-length.).

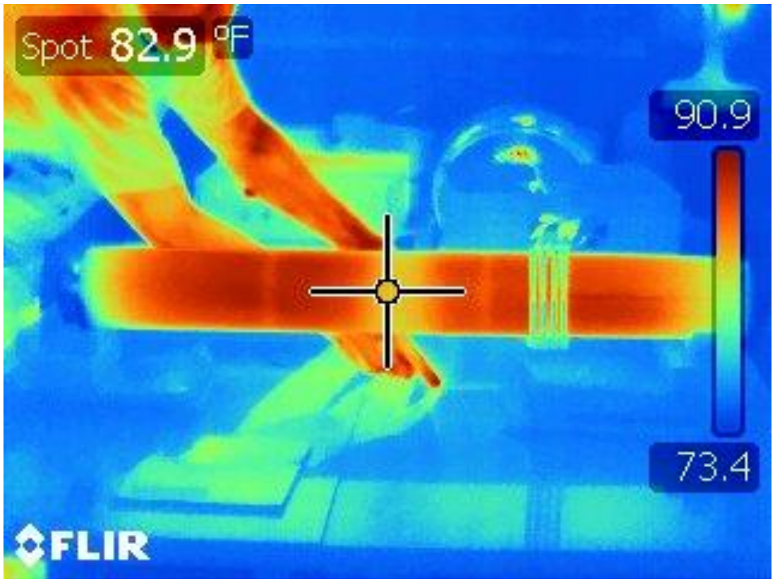

Figure A-4: Infrared thermography image of sample-1 during induction heating.

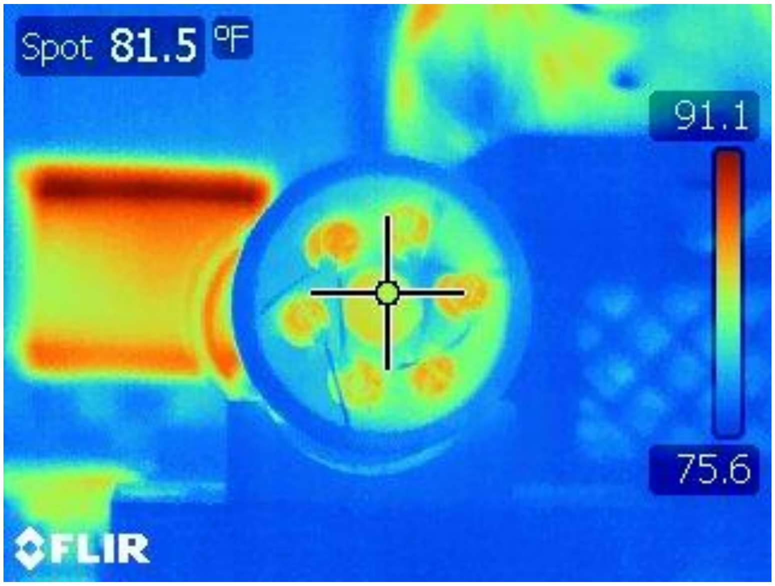

Figure A-5: Infrared thermography image of the end of the sample during heating shows the strands as hotter than the surrounding duct.

IRT images were taken of the outside of the duct of the actively heated tendon sample. The induction heater was successful in heating the strands enough to create thermal transients on the outside of the polyvinyl chloride (PVC) duct that were detectable by the IRT camera (Figure A-4 and Figure A-6). The ends of the PVC sample were not heated (also indicated as yellow) as the induction coil could not be moved past the supports of the sample during the test.

The 2-in gap in the strands is easily visible at mid-span of the sample, indicated by a yellow gap between the red (hotter) areas on each side. The vertical lighter lines on either side of the gap indicates the location of the plastic spacers inside the duct that were used to hold the strands in place.

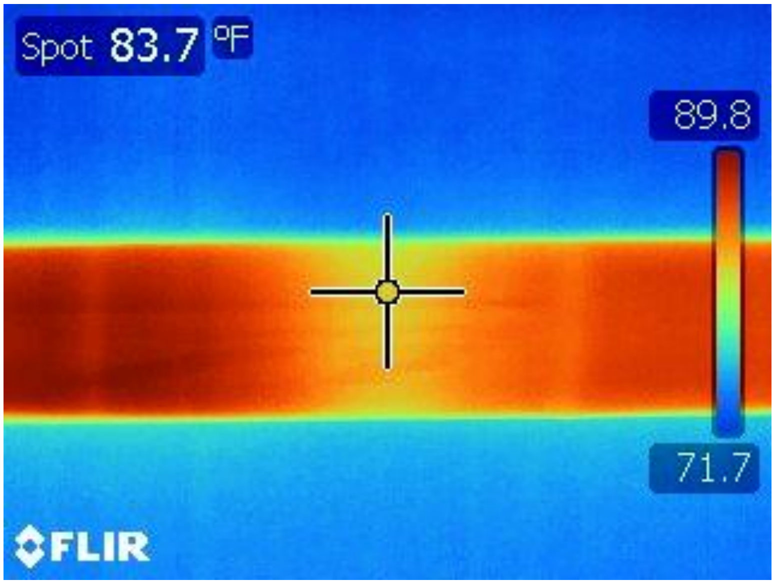

Figure A-6: Close-up infrared thermography image of the sample after heating (at the location of the 2-in gap (break) in the 6 strands indicated by a yellow band).

The IRT images of the outside of the experimental sample tendon duct were successful in indicating differential heating in the areas of a major discontinuity in the strands, indicating a loss in strand section.

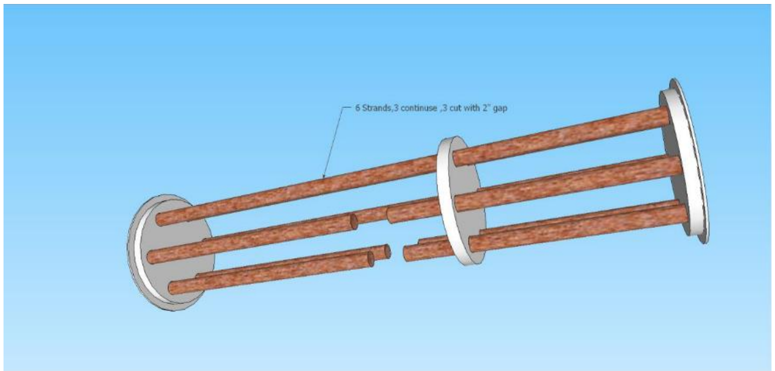

Figure A-7: Typical arrangement of strands for sample-2 (3-strands cut with 2-in gap at mid-length).

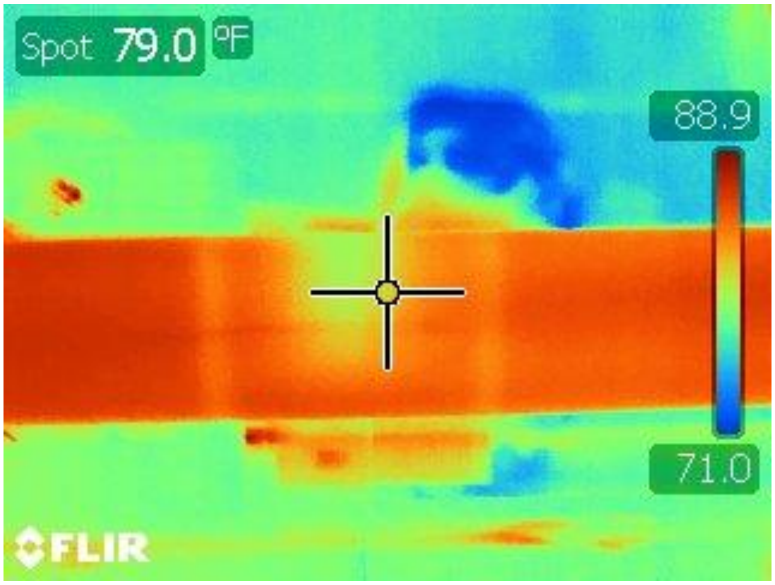

Figure A-8: IRT image of sample 2 (3-strands cut with 2-inch gap).

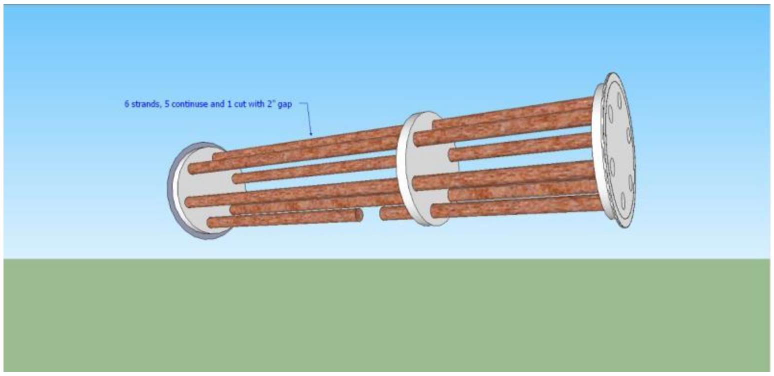

Figure A-9: Typical arrangement of strands for sample-3 (1-strand cut with 2-in gap at mid-length).

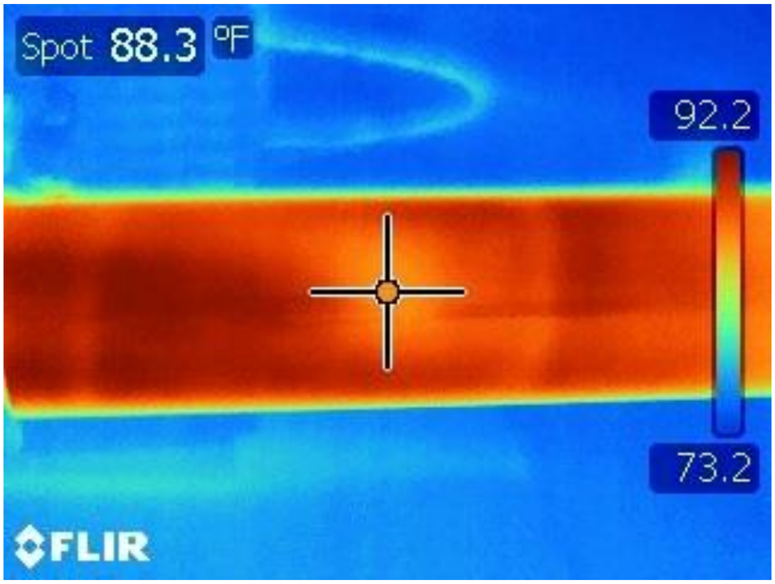

Figure A-10: IRT image of sample-3 (1-strand cut with 2-in gap).

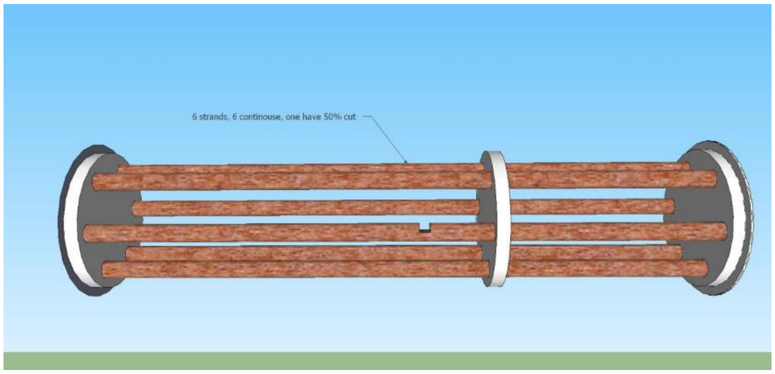

Figure A-11: Typical arrangement of strands for sample-4 (50% of 1-strand cut with 1-in gap).

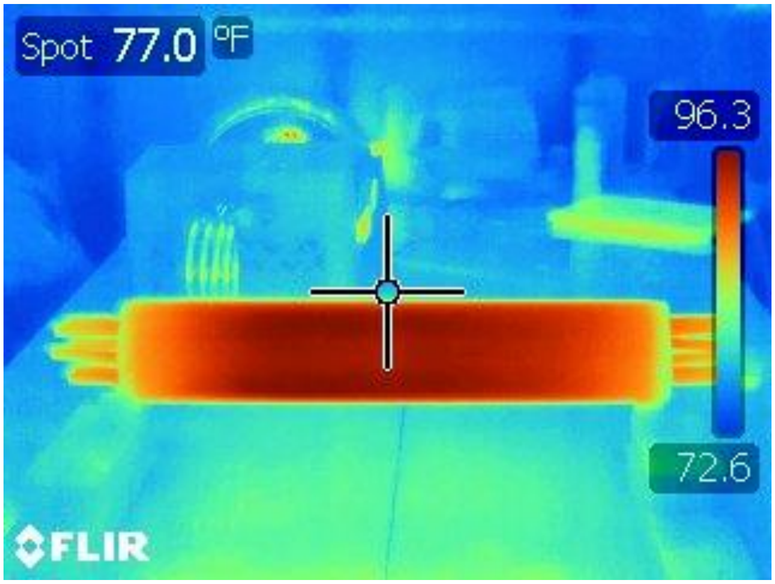

Figure A-12: IRT image of sample-4 (50% of 1-strand cut with 1-in gap at mid-length)

A.4 NUMERICAL MODELLING OF ACTIVE INFRARED THERMOGRAPHY

A finite element model was used to numerically model the effect of induction heating on the thermal state of a composite steel and grout bridge post-tensioning tendon using the finite difference method. The structural model of the tendon for this finite difference model is based on the sample used in the laboratory which was a 4-in wide round PVC pipe which enclosed the steel strands and concrete grout. The finite difference model simulates the heating of the tendon sample from the inside to the outside due to induction heating of the steel strands. The proposed finite difference model will model temperature changes over time due to the heating of the steel strands by induction heating to compare the temperatures to the temperatures found under laboratory conditions.

The approach to the analysis is based on a simplifying assumption that the induction heating will heat all strands equally in the manner observed in the laboratory. It is also assumed that the sample is surrounded by ambient air of a constant 22°C. For the simplifying assumptions of uniform longitudinal heating, a two-dimensional model of the tendon based on a vertical cross-section is utilized for the analysis. The flow of the heat through the tendon sample during the induction heating is mathematically modeled based on the two-dimensional differential heat equation:

$$\rho Cp \frac{\partial T}{\partial t} = k\left(\frac{\partial^2 T}{\partial x^2} + \frac{\partial^2 T}{\partial y^2}\right)$$

This equation mathematically expresses the temperature as a function of time and as a function of position within the tendon sample cross-section. The additional parameters in the above equation are the thermal material parameters:

ρ = Density of the material

C_p = Heat capacity

k = thermal conductivity

The thermal material parameters vary based on the type of material. In the case of the composite tendon the three materials used are PVC, concrete, and steel. There was no need to model the steel because the steel strand temperature was modelled as a point temperature which changed with time due to the induction heating. In addition, the ambient air temperature was assumed to be constant as the air was free to flow around the sample. Therefore, the only thermal parameters required were those for concrete and PVC. For convenience of calculations the material density, heat capacity and thermal conductivity were lumped together into one parameter, α, the thermal diffusivity:

$$\alpha = \frac{k}{\rho Cp}$$

Based on the above material parameters the thermal diffusivity used for this project are:

$\alpha\ for\ PVC$ = 8.0 x 10^{-8} m^2/s

$\alpha\ for\ concrete$ = 3.23 x 10^{-7} m^2/s

Incorporating the substitution for thermal diffusivity into the two-dimensional differential heat equation, the equation can now be expressed as follows:

$$\frac{\partial T}{\partial t} = \alpha\left(\frac{\partial^2 T}{\partial x^2} + \frac{\partial^2 T}{\partial y^2}\right)$$

The effect of induction heating on the thermal state of a tendon sample was modeled in an excel spreadsheet program using the finite difference method applied to a mesh representing the cross-section of the sample. The sample cross-section was divided into 43 rows and 43 columns which was used to individually model the temperatures at different locations within the sample at different time steps.

Finite difference approximations for the first and second derivative expressions in the differential heat equation can be made using the following finite difference equation including the superscript k which denotes the time increment:

$$\frac{T_{i,j}^{k+1} - T_{i,j}^{k}}{\Delta t} = \alpha\left[\left(\frac{T_{i-1,j}^{k} - 2T_{i,j}^{k} + T_{i+1,j}^{k}}{\Delta x^2}\right) + \left(\frac{T_{i,j-1}^{k} - 2T_{i,j}^{k} + T_{i,j+1}^{k}}{\Delta y^2}\right)\right]$$

The spatial location of each point in the mesh is represented in the x-direction by the subscript i and in the y-direction by the subscript j. Assuming equal increments in the x (i) and y (j) directions and assuming u = the x increment and the y increment, the equation can be expressed as follows:

$$\frac{T_{i,j}^{k+1} - T_{i,j}^{k}}{\Delta t} = \alpha\left[\left(\frac{T_{i,j-1}^{k} + T_{i-1,j}^{k} - 4T_{i,j}^{k} + T_{i+1,j}^{k} + T_{i,j+1}^{k}}{u^2}\right)\right]$$

The above equation can be further manipulated to yield an expression for the temperature of a node location at the next time increment:

$$T_{i,j}^{k+1} = T_{i,j}^{k} + \Delta t\alpha\left[\left(\frac{T_{i,j-1}^{k} + T_{i-1,j}^{k} - 4T_{i,j}^{k} + T_{i+1,j}^{k} + T_{i,j+1}^{k}}{u^2}\right)\right]$$

The above equation can again be further manipulated to simplify the expression:

$$T_{i,j}^{k+1} = \left(1 - \frac{4\Delta t\alpha}{u^2}\right)T_{i,j}^{k} + \Delta t\alpha\left[\left(\frac{T_{i,j-1}^{k} + T_{i-1,j}^{k} + T_{i+1,j}^{k} + T_{i,j+1}^{k}}{u^2}\right)\right]$$

The external boundary condition (temperature of the air) is assumed to be a constant 22°C. The induction heating temperature was calculated in the excel spreadsheet for each time step incrementally corresponding to the time step of the finite difference method up to the target time of approximately 14 minutes (time to reach steady state). Iterations begin with a tendon section with an assumed room temperature (22°C) for each of the tendon elements.

An excel spreadsheet was set up to individually model each time increment and the corresponding spatial distribution of temperature throughout the tendon cross-section. The thermal properties of the concrete and the PVC were modeled separately in the spreadsheet model for each individual spreadsheet cell. The steel strand temperature was modeled as a point load which varied in time according to the heating curve discussed previously. The time step increment was reduced until it was seen that the model was stable through the full 14-minute time period. The time step was limited to 4.4 seconds to assure stability (convergence) of the finite difference mathematical model.

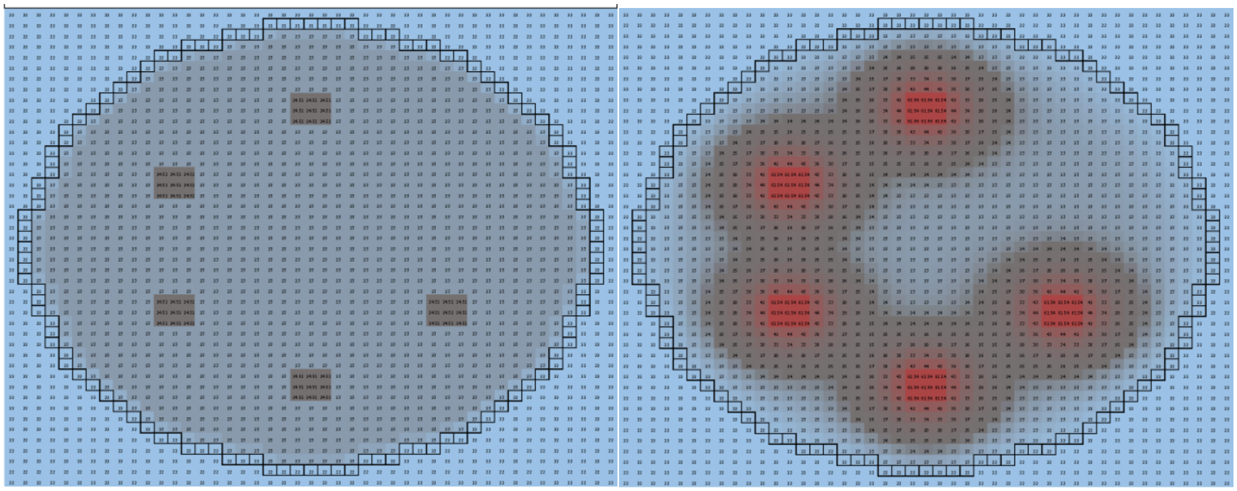

Figure A-13: Temperature of finite difference model at time T = 0 minutes and 1.8 minutes.

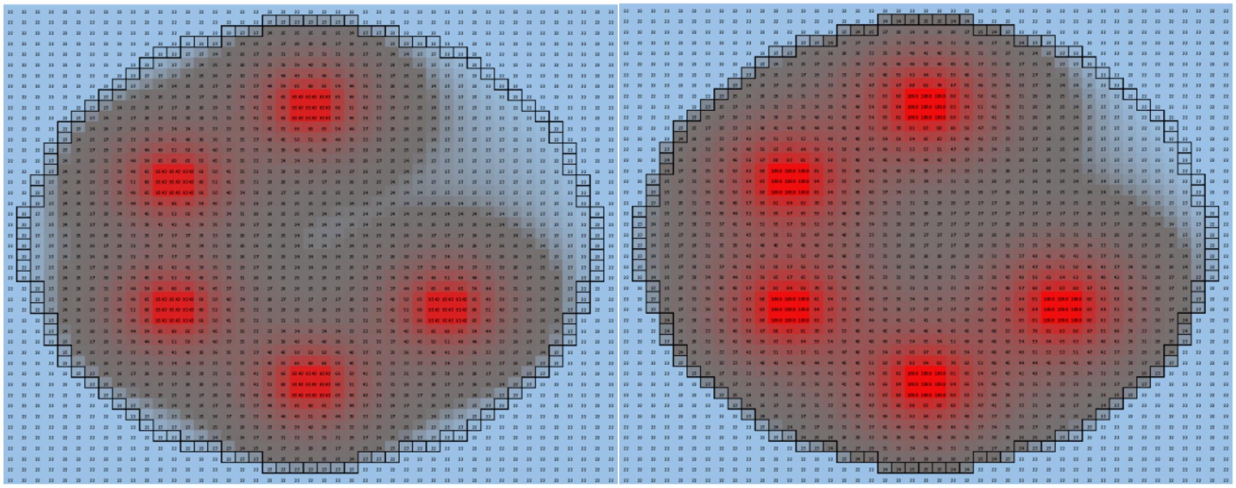

Figure A-14: Temperature of finite difference model at time T = 3.7 minutes and 5.5 minutes.

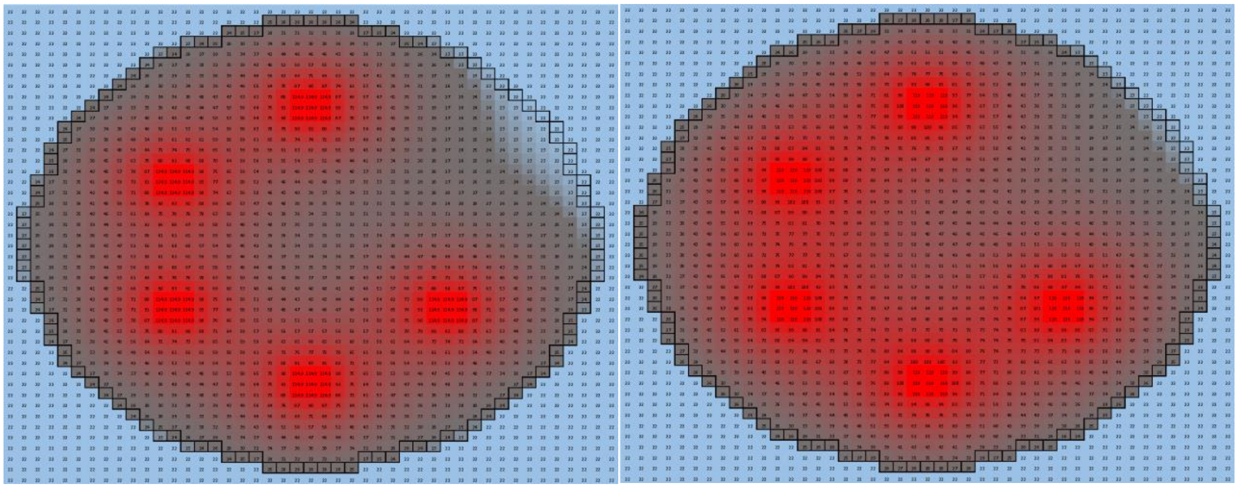

Figure A-15: Temperature of finite difference model at time T = 7.3 minutes and 11.0 minutes.

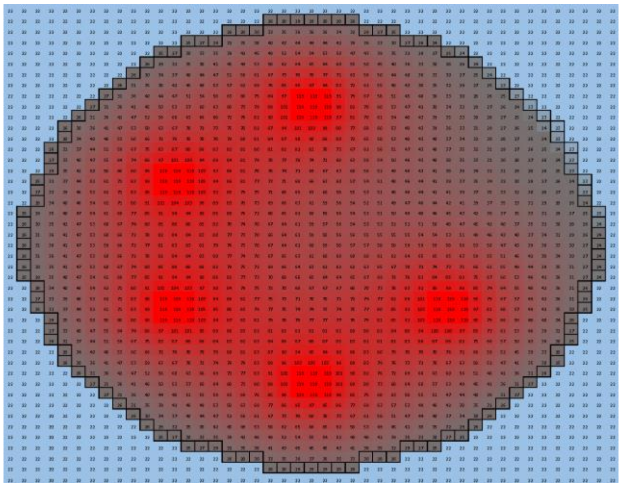

Figure A-16: Temperature of finite difference model at time T = 14.0 minutes.

A.5 SUMMARY OF IRT

The infrared thermography images of the outside of the experimental sample tendon duct were successful in indicating differential heating in the areas of major discontinuities in the strands, indicating a loss in strand section. IRT results for minor defects in the strands and minor section loss was found to be of limited effectiveness. Overall the finite model results appeared to yield realistic results and was verified by laboratory testing with similar tendon samples.

APPENDIX B INDUCTANCE MEASUREMENT METHOD

B.1 INDUCTANCE TEST PRINCIPLE

The objective of the work presented here is to verify the effectiveness of inductance measurement method as a non-destructive testing (NDT) technique and to determine the parameters that most influence the accuracy of the method. Inductance was recognized as a circuit characteristic of an alternating current (AC) circuit that could be used as a metric for the relative amount of ferromagnetic material present along the length of a post-tensioning tendon. Inductance may be described as a property of a circuit by which a change in current through the circuit induces an electromotive force in both the circuit itself and in any nearby circuits by mutual inductance. In the case of the NDT evaluation of internal tendons, an inductor coil (probe) paired with an inductance meter is placed on the concrete slab surface, energized with an AC current, and an expanding and contracting magnetic field is created which links to the steel strands inside the tendon to the probe coil by mutual inductance. Through mutual inductance, a larger amount of ferromagnetic material in the tendon produces an apparent larger inductance meter reading and smaller amount of ferromagnetic material in the tendon produces an apparent smaller inductance meter reading.

Inductance is an electromagnetic phenomenon which occurs under conditions of changing magnetic fields. The fundamental cause of inductance is the microscopic change of an electric field into a magnetic field when an electric charge is accelerated. When a constant current flow through a wire, circular radiating magnetic fields are produced. If the current remains constant the radiating magnetic field does not change. However, if the current varies as it does under AC conditions, the magnetic field constantly changes. Under AC conditions the magnetic field around a wire expands and collapses as it reverses direction under each current cycle. Magnetic fields have influence on charges that have relative motion in a perpendicular direction to the magnetic field. Therefore, a magnetic field will interact with a stationary charge when the magnetic field itself is moving. The changing magnetic field creates an induced electromotive force (EMF) which opposes the current flow. This induced EMF which opposes the current flow is commonly referred to as “back EMF”. For a single straight wire, the back EMF is usually not significant. However, for devices such as inductors, which concentrate the magnetic field in a coil of wire, the back EMF can cause large self-inductance. Inductors are devices which concentrate magnetic flux by focusing the overlapping self-inductance of multiple parallel loops of wire. See Figure B-1.

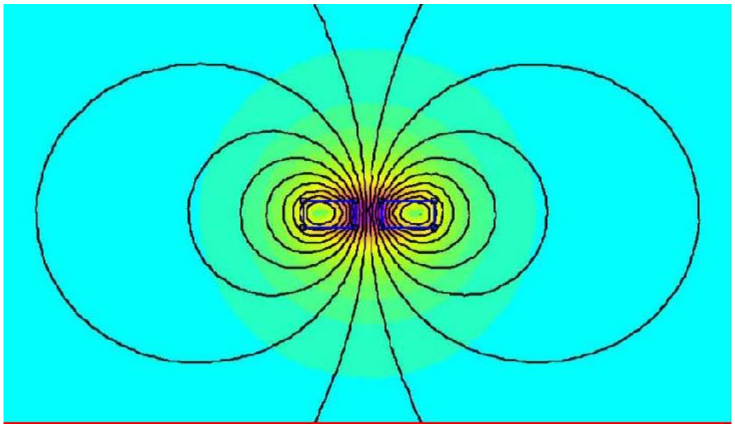

Figure B-1: Magnetic flux field of a multi-loop inductor coil excited by a sinusoidal alternating current.

The magnetic field for an inductor coil can be expressed as:

$$B = \frac{\mu N I}{l}$$

Where:

$$B = magnetic\ field$$

$$\mu = magnetic\ permeability$$

$$I = current\ flowing\ through\ coil$$

$$N = number\ of\ turns\ of\ coil$$

$$l = length\ of\ coil$$

The magnetic flux passing through a surface area A (area of circular coil) can be calculated as:

$$\phi_M = BA$$

Where:

$$\phi_M = magnetic\ flux$$

$$A = cross\ sectional\ area\ of\ coil$$

Substituting for B:

$$\phi_M = \frac{\mu N I}{l} A$$

For a changing current, such as what is present in a circuit under AC conditions the voltage across an inductor is based on the change in the magnetic flux with respect to time as:

$$V_L = -N\frac{d\phi_M}{dt}$$

Note the negative sign indicates the voltage opposes change in flux. Substituting for the magnetic flux:

$$V_L = -N\frac{d(\frac{\mu NI}{l}A)}{dt}$$

Moving the constants from the differential:

$$V_L = -\frac{N^2\mu A}{l}\frac{dI}{dt}$$

Substituting the inductance for the expression to the left of the differential the voltage across an inductor can be expressed in equation form as:

$$V_L = -L\frac{dI}{dt}$$

Where:

$$L = inductance = \frac{N^2\mu A}{l}$$

$$dI = increment\ of\ current$$

$$dt = increment\ of\ time$$

The above equation may be interpreted to mean that the amplitude of the voltage across an inductor is proportional to the rate at which the current changes. The equation may also be rearranged and expressed in terms of the current as:

$$\mathrm{I_L} = \frac{1}{\mathrm{L}}\int \mathrm{V_L\,dt}$$

The inductor coil (probe) used in this project did not act in an isolated way but interacted with the elements in the vicinity of the coil in a manner related to the magnetic permeability of the material. The materials present in the area of the coil during testing include air, concrete, transverse steel reinforcement, steel conduit, and prestressing strands. Magnetic permeability of a material is customarily measured on a comparative scale to the permeability of free space which is based on a magnetic field in a vacuum. Relative permeability is defined as the ratio of the actual permeability divided by the permeability of free space. Air and concrete both have a relative permeability close to 1.0 and thus have very little influence on a magnetic field. Carbon steel, however, exhibits a larger relative permeability of approximately 100 and has a major effect on magnetic fields. Since carbon steel was present in the prestressing strands as well as the conduit and transverse reinforcement, these elements had an effect of the testing results. The red rust (Fe_2O_3) formed from strand corrosion is assumed to have a relative permeability of 1.0 similar to the nonmagnetic material concrete.

If a secondary conductor is present in the vicinity of a primary conductor that is generating a magnetic field, the mutual inductance is the ratio of the magnetic flux in the secondary and the current in the primary as shown in the following equation:

$$\mathrm{M}_{21} = \frac{\mathrm{N}_2 \phi_{\mathrm{M}21}}{\mathrm{I}_1}$$

Where:

$$\mathrm{M}_{21} = \text{mutual inductance}$$

$$\mathrm{N}_2 = \text{number of turns of secondary coil}$$

$$\phi_{\mathrm{M}2} = \text{magnetic flux in secondary coil}$$

$$\mathrm{I}_1 = \text{current flowing through primary}$$

The opposite mutual inductance relationship is also true as expressed:

$$\mathrm{M}_{12} = \frac{\mathrm{N}_1 \phi_{\mathrm{M}12}}{\mathrm{I}_2}$$

So it follows that the mutual inductances are equivalent:

$$\mathrm{M}_{21} = \mathrm{M}_{12} = \text{mutual inductance}$$

The inductance of the primary and the secondary conductors are linked by their mutual inductance. In the case of this project the inductance of the primary inductor coil (probe) will link to the secondary steel elements in the vicinity of it. The degree to which the coil and the secondary elements link is based on the mass of the steel secondary elements present and the flux leakage due to the distance between the coil and the secondary elements.

B.2 NUMERICAL SIMULATION OF THE LABORATORY TESTING

Due to the ferromagnetic materials involved and the complexity of the inductance testing environment, a closed form numerical solution for the mutual inductance between coil and the strands is difficult to implement. For that reason, numerical modelling of the inductance testing was carried out using a finite element program. The finite element method magnetics (FEMM) program was used to model the laboratory test in finite elements. The FEMM program is a two-dimensional finite element program that analyzes complex electromagnetic models consisting of multiple material types and geometries. The program provides an inductance measurement function that was used to provide the data necessary for the inductance plots. The finite element model included the relative magnetic permeability of the surrounding air and the steel. The concrete magnetic permeability was assumed to be 1.0. The strand defects were modelled as localized sections of smaller steel area corresponding to the defect locations of the actual laboratory sample. A fine uniform triangular mesh was generated for the entire system to increase the accuracy of the results. Iterations of analysis and inductance measurements were produced at uniform intervals along the length of the strands in the finite element model and the results are plotted in Figure B-2. The plotted results show approximately the same qualitative signature as the field measured inductance plot of Figure 5-52 with a very large dip at the 100% gap and diminishing dips in inductance at the 50% and 14% section loss locations.

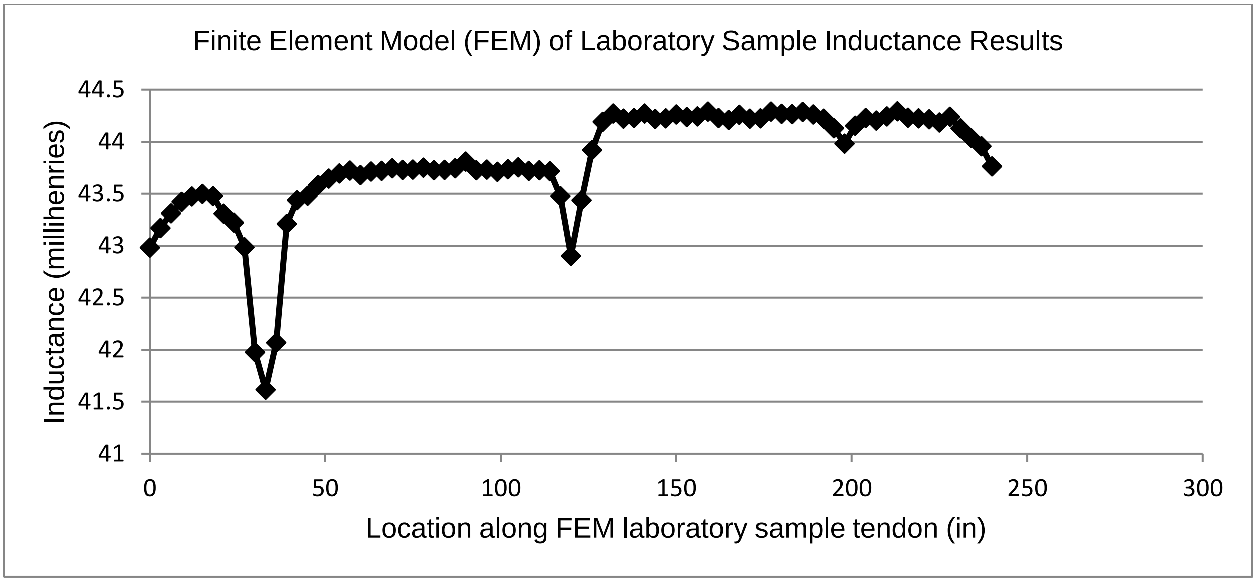

Figure B-2: Plot of finite element inductance values along the length of a model of the laboratory sample.

B.3 NUMERICAL SIMULATION OF THE SEGMENT TESTING

The FEMM finite element program was also used to model the segment test as shown in Figure B-3 through Figure B-10. The relative magnetic permeability of the air, concrete and steel were modelled as was done in the previous laboratory test model. The computations were performed in an iterative process which involved recalculating the inductance for 3-in increments along the length of the model. For each incremental inductor location, a new mesh was created and a new analysis was performed to calculate the inductance.

Figure B-3: Partial magnified cross-section elevation view of the finite element mesh of the segment model at the edge of the segment shows the conduit (hot-rolled low carbon steel) longitudinal and transverse strands (cold-drawn carbon steel, annealed) and inductor (839 turns of 18 AWG).

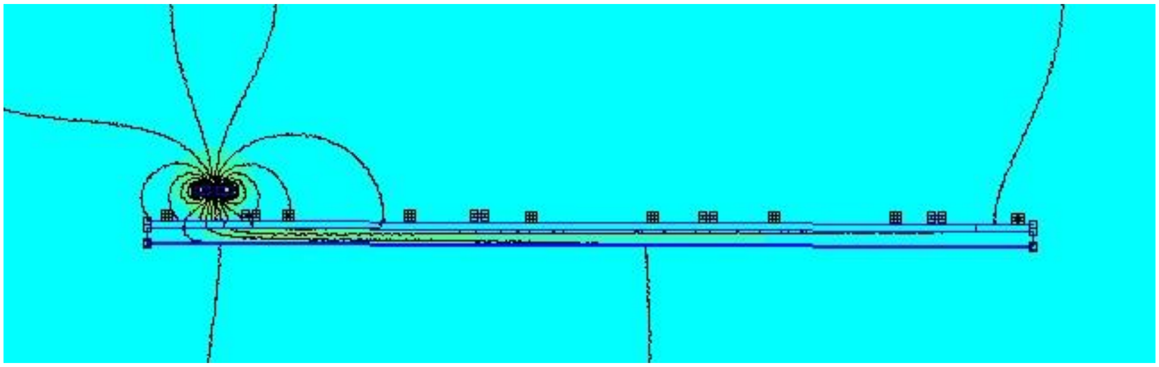

Figure B-4: Finite element flux field of the segment model at 6 inches along segment.

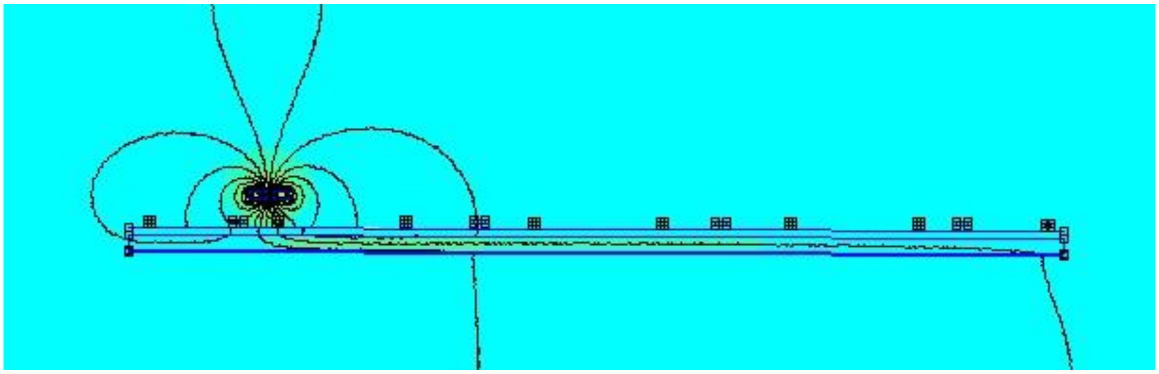

Figure B-5: Finite element flux field of the segment model at 18 inches along segment.

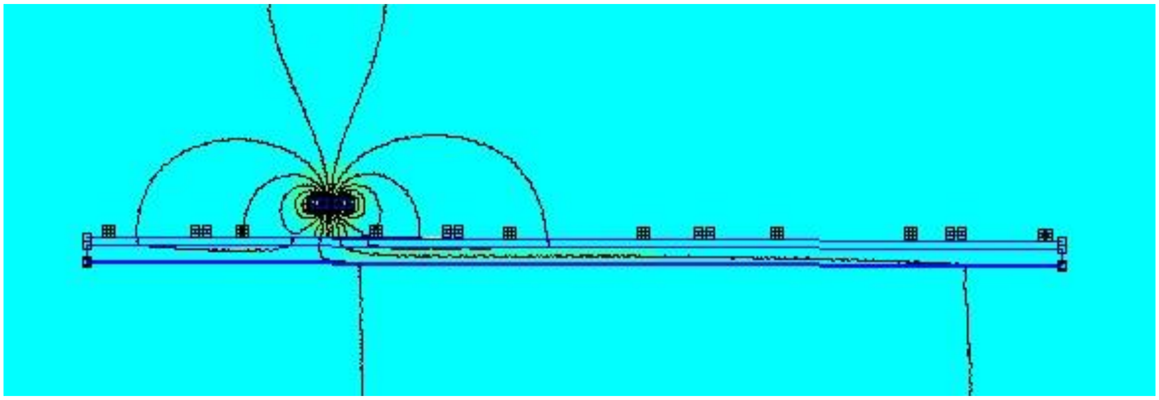

Figure B-6: Finite element flux field of the segment model at 30 inches along segment.

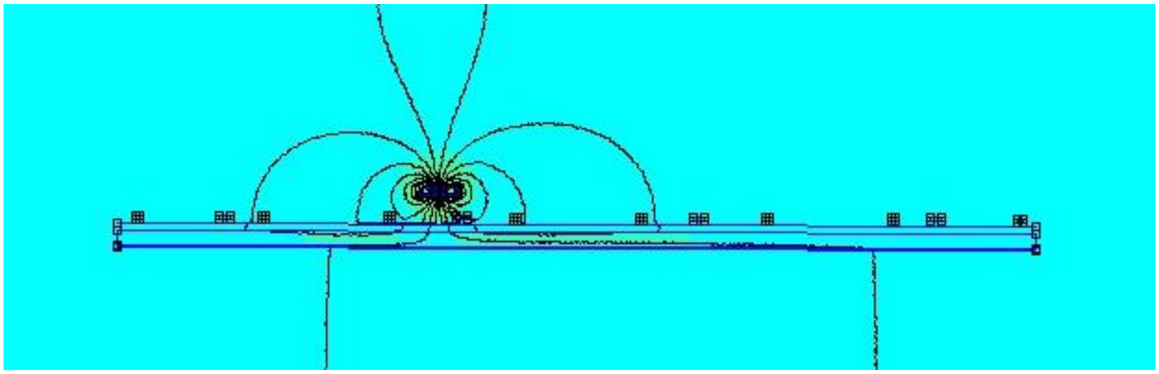

Figure B-7: Finite element flux field of the segment model at 42 inches along segment.

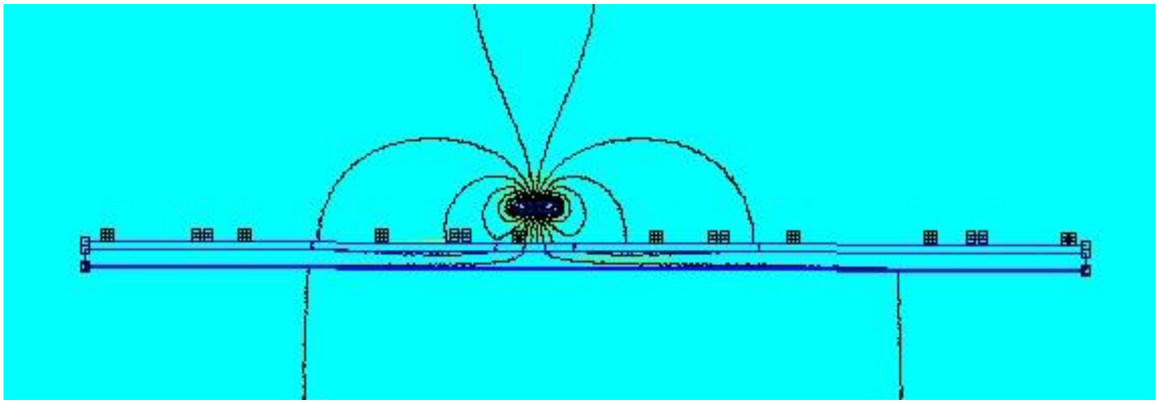

Figure B-8: Finite element flux field of the segment model at 54 inches along segment.

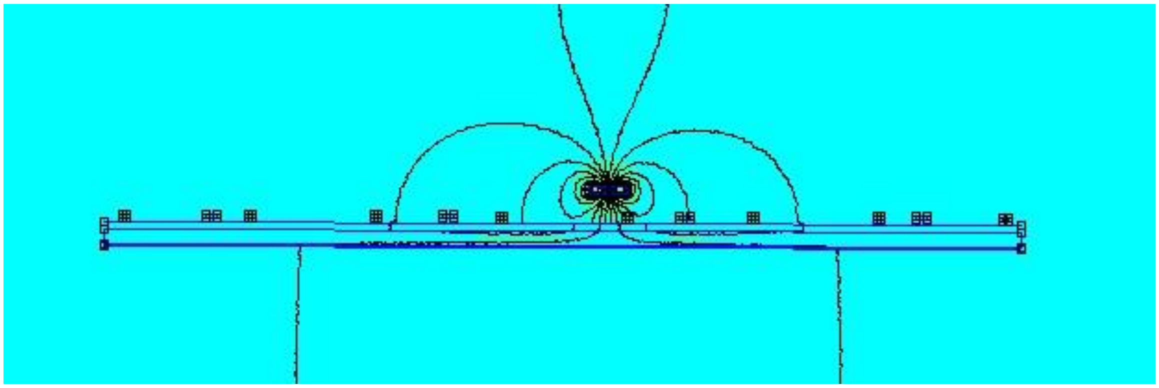

Figure B-9: Finite element flux field of the segment model at 66 inches along segment.

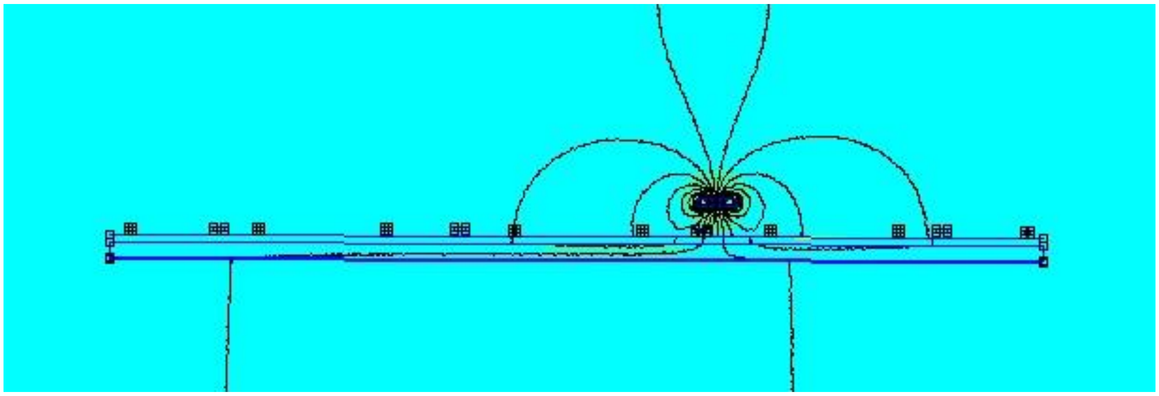

Figure B-10: Finite element flux field of the segment model at 78 inches along segment.

The plotted finite element analysis results shown in Figure B-11 indicates approximately the same qualitative signature as the field measured inductance plot with spikes in inductance due to transverse reinforcement. Like the field measurements, the factors affecting the inductance plot are the distance of the coil to the tendon and the mass of steel present within the coil's proximity.

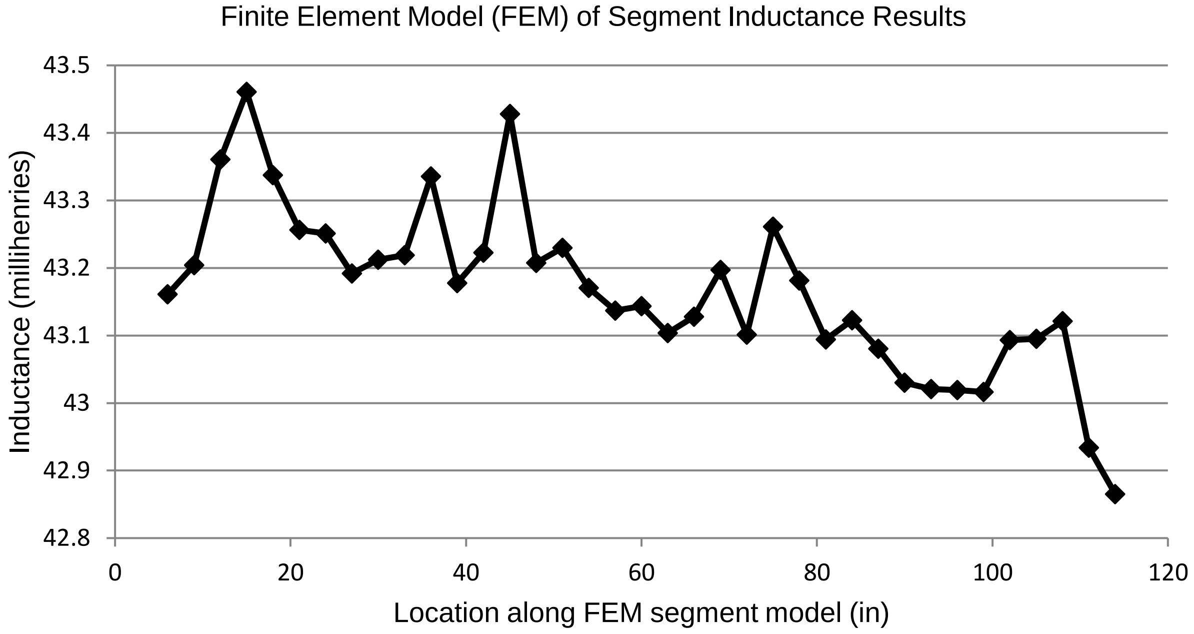

Figure B-11: Plot of results of finite element analysis inductance measurement results for the segment.

B.4 STATISTICAL EVALUATION OF SEGMENT TEST RESULTS

A statistical comparison of the test runs was done to verify the degree to which there was correlation between the data sets and consistency between test runs. The correlation coefficient was identified as a good statistic to compare each of the test runs. Overall the correlation coefficient was extremely high (greater than 0.99) for all comparisons. This was to be expected based on the close correlation shown by the data plats as shown in Figure 5-54. In addition, for each of the comparison data sets, the “1 Strand” data set vales were subtracted from each comparison set of data and the standard deviation was calculated. The results of this calculation show a standard deviation less than 0.005 which indicates very small variation in difference from the “1 Strand” data set and the comparison set. Table B-1 summarizes results of the statistical calculations.

As was to be expected, the difference of inductance between the larger and smaller samples resulted in a generally positive (greater than zero) difference as shown in Figure B-12 through Figure B-16. The variation in the difference could be due to factors such as electromagnetic noise as well as inconsistencies in placement of probe. Overall the major data outliers were found to be at the ends of the segment and these could possibly be attributed to edge discontinuity effects.

Importantly, the correlation between the data sets did not dramatically vary at locations of secondary transverse reinforcement. Since the transverse reinforcement inductance is the same in “1-strand” run and the other samples, the inductance of the transverse reinforcement cancels out when one data set is subtracted from the other. The important implication of this finding is that section loss may be detected at locations covered by transverse reinforcement.

Table B-1: Statistical evaluation of segment test runs

Statistical Evaluation of Inductance Tests of Segment Strand Configurations		
Comparison sets	**Correlation coefficient between sample sets**	**Standard deviation of difference between sample sets**
1 Strand and 2 Strand	0.9981	0.004798
1 Strand and 3 Strand	0.9985	0.004304
1 Strand and 4 Strand	0.9988	0.004354
1 Strand and 5 Strand	0.9988	0.003913
1 Strand and 6 Strand	0.9989	0.004054

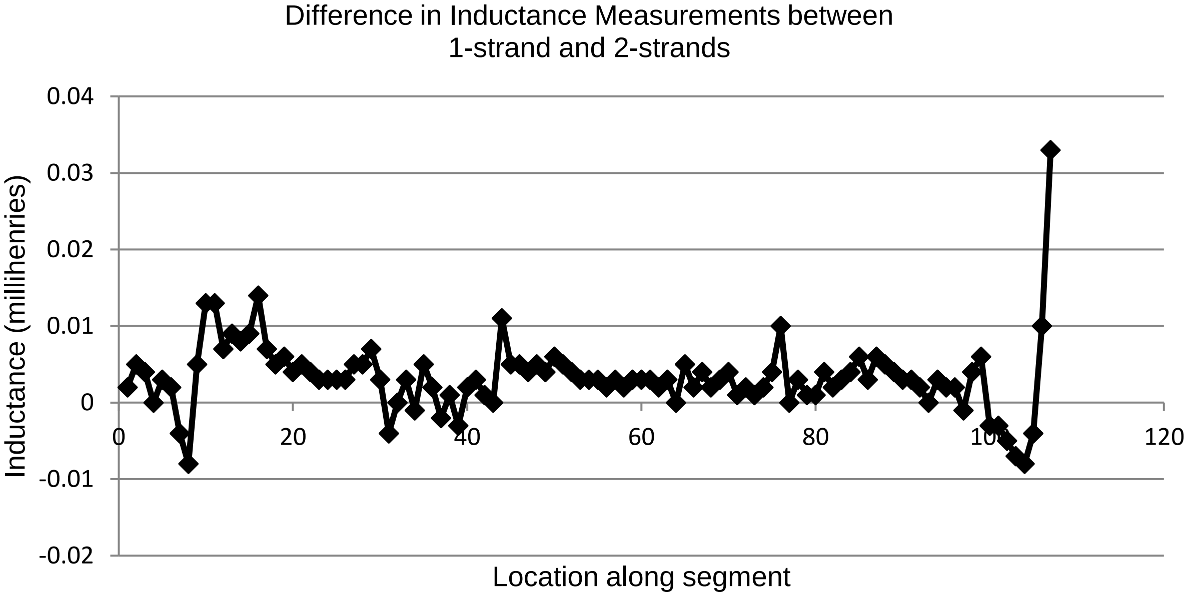

Figure B-12: Difference in inductance measurements between 1-strand configuration and 2-strand configuration shows discontinuity effects at the ends (less than zero) and minor electromagnetic noise effects creating a negative difference from approximately location 30 to 40.

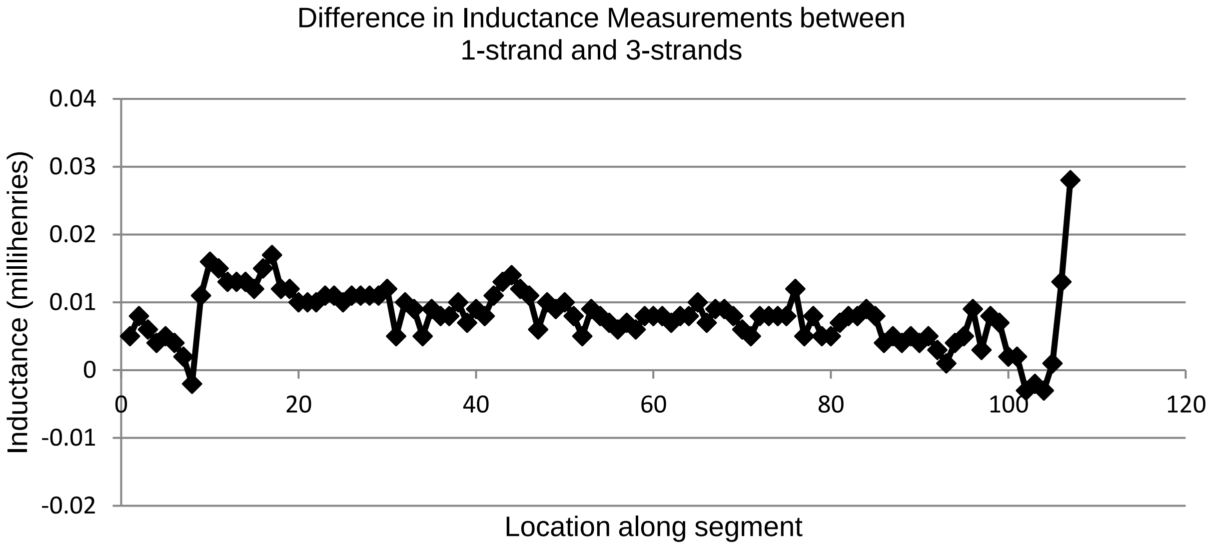

Figure B-13: Difference in inductance measurements between 1-strand configuration and 3-strand configuration shows discontinuity effects at the ends (less than zero).

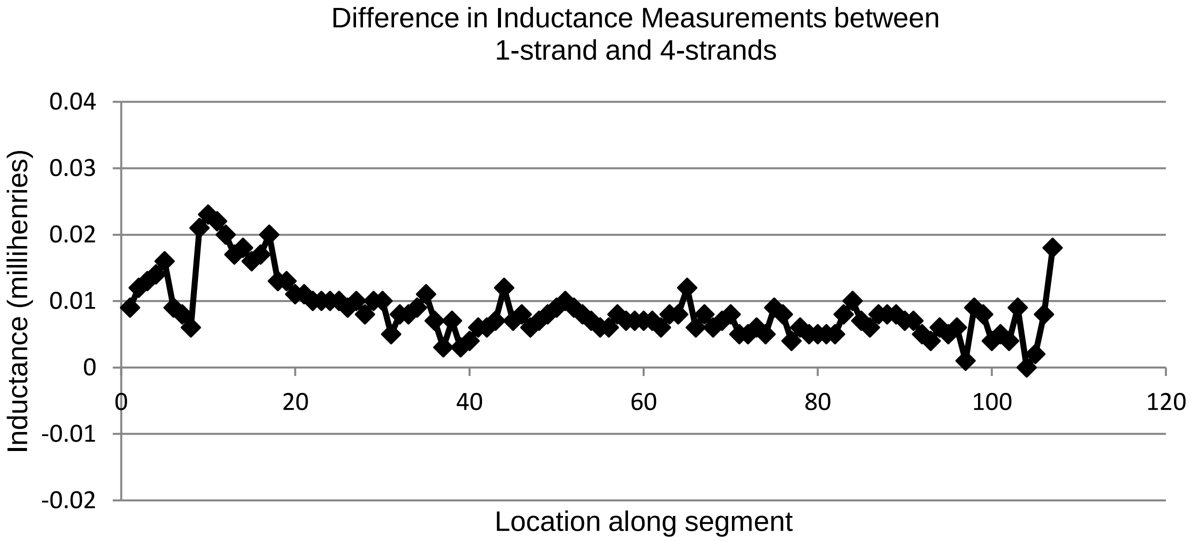

Figure B-14: Difference in inductance measurements between 1-strand configuration and 4-strand configuration shows discontinuity effects at one end (less than zero).

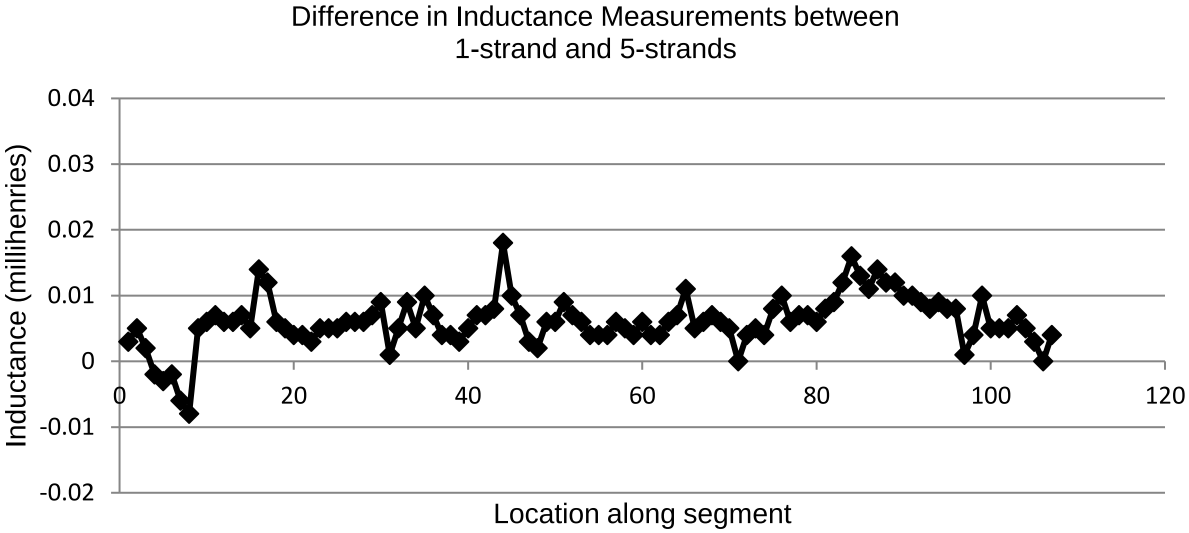

Figure B-15: Difference in inductance measurements between 1-strand configuration and 5-strand configuration shows discontinuity effects at the ends (less than zero).

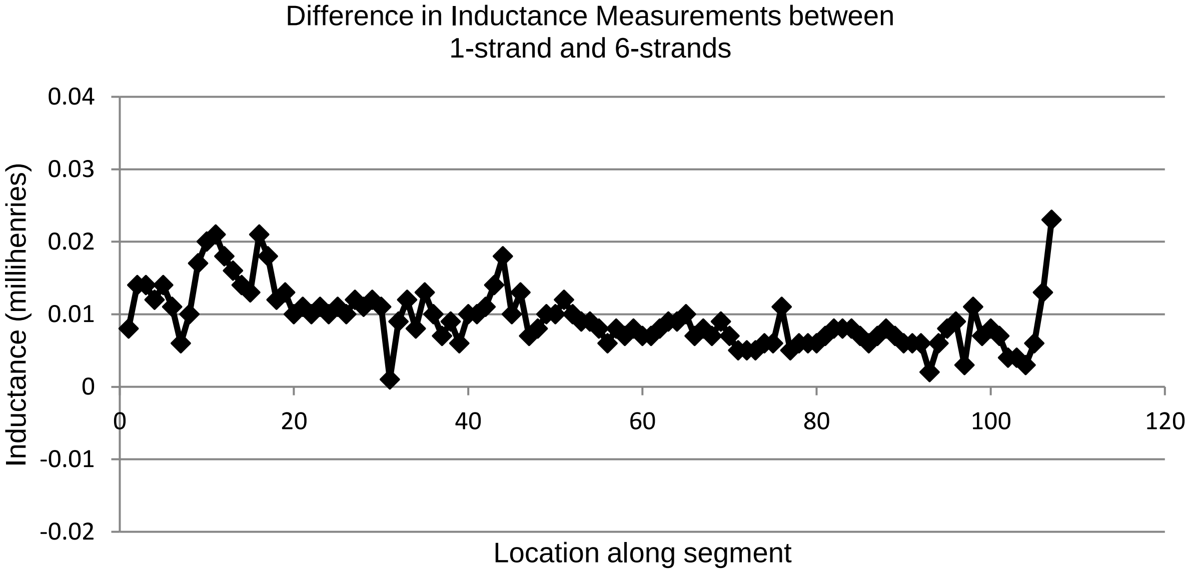

Figure B-16: Difference in inductance measurements between 1-strand configuration and 6-strand configurations (all positive) with minor outlier data points.

B.5 INDUCTANCE TEST SUMMARY

Numerical modelling of the laboratory and segment samples was carried out using the FEMM program. The two-dimensional finite element models of the inductance method were found to exhibit a qualitative correlation to the overall inductance signature of the actual laboratory and segmental box inductance measurements. The finite element models indicated the localized spikes of increased inductance resulting from the transverse reinforcement as well as the overall slope of the inductance across the segment resulting from non-uniform vertical profile of the conduit.

Interestingly, as indicated by the laboratory testing of a tendon sample, when no transverse reinforcement is present and the conduit is a uniform distance from the surface of the concrete, the inductance method can locate defects as small as without a previous baseline calibration run for comparison. The section loss for the laboratory sample was indicated by a localized drop in inductance at a location along the length corresponding to the defect.

Future potential improvements to the inductance method may include modification to inductor coil (probe) geometry to sharpen (localize) the inductance reading and modification of the coil turns and wrapping method to increase depth of penetration of the test field. Other future potential improvements also include the use of a more precise inductance meter with a larger voltage test signal. Data set collection and processing is also an important issue to be investigated since several data sets averaged together may provide a better-quality data set due to cancellation of data set outliers caused by electromagnetic noise.